Computational Modelling of Highly Mis-matched Alloys of GaNAsP and GaNAsBi as a Laser Gain Material

Ph.D. Thesis
in
Engineering Physics
University of Gaziantep

Supervisor
Prof. Dr. Beşire GÖNÜL

By
Ömer Lütfi ÜNSAL

April 2016

REPUBLIC OF TURKEY
GAZİANTEP UNIVERSITY
GRADUATE SCHOOL OF
NATURAL AND APPLIED SCIENCES
ENGINEERING PHYSICS

Name of the Thesis	:	Computational modelling of highly mis-matched alloys of GaNAsP and GaNAsBi as a laser gain material
Name of the Student	:	Ömer Lütfi ÜNSAL
Exam Date	:	18.04.2016

Approval of the Graduate School of Natural and Applied Sciences.

Prof. Dr. Metin BEDİR
Director

I certify that this thesis satisfies all the requirements as a thesis for the degree of Doctor of Philosophy.

Prof. Dr. Ramazan KOÇ
Head of Department

This is to certify that we have read this thesis and that in our opinion it is fully adequate, in scope and quality, as a thesis for the degree of Doctor of Philosophy.

Prof. Dr. Beşire GÖNÜL
Supervisor

Examining Committee Members:

Prof. Dr. Nuran DOĞRU

Prof. Dr. Beşire GÖNÜL

Assoc. Prof. Dr. Koray KÖKSAL

Assoc. Prof. Dr. Hüseyin TOKTAMIŞ

Assist. Prof. Dr. Sinan KAZAN

I hereby declare that all information in this document has been obtained and presented in accordance with academic rules and ethical conduct. I also declare that, as required by these rules and conduct, I have fully cited and referenced all material and results that are not original to this work.

Ömer Lütfi ÜNSAL

ABSTRACT

COMPUTATIONAL MODELLING OF HIGHLY MIS-MATCHED ALLOYS OF GaNAsP AND GaNAsBi AS A LASER GAIN MATERIAL

ÜNSAL, Ömer Lütfi

Ph.D. in Engineering Physics

Supervisor: Prof. Dr. Beşire GÖNÜL

April 2016, 108 pages

The aim of this thesis work is to model and investigate the electronic band structure and current density of highly mismatched alloys of GaNAsP and GaNAsBi. To reveal the importance of these highly mismatched alloys we provide a comparison of GaNAsP and GaNAsBi with their nitrogen free N-counterpart.

The GaP-based dilute nitride direct bandgap material Ga(NAsP) is gaining importance for the monolithic integration of laser diodes on Si microprocessors. The major advantage of this newly proposed novel laser material system is the small lattice mismatch between GaP and Si. However, from first gain measurements it is found that Ga(NAsP)/GaP material system has high threshold current at room temperature. Therefore, we present a comprehensive theoretical analysis of band alignment and threshold current in dilute nitride direct bandgap Ga(NAsP)/GaP/AlGaP QWs on silicon substrates using model calculations. The comparison of our calculated results with that of the experimental data indicates that the Auger effect involving CHCC process can be considered as the dominant non-radiative loss mechanism at 300K.

It has just recently reported that highly mismatched semiconductor alloys of $GaAs_{1-x}Bi_x$ has also several novel electronic properties, including a rapid reduction in energy gap with increasing x and also a strong increase in spin-orbit-splitting energy with increasing Bi composition. We, therefore to understand the origins of the rapid reduction in energy gap and its consequences, study and compare band gap and critical thickness of GaNAsBi. The results indicate that GaNAsBi material can be used in optoelectronic applications in the long wavelength region.

Key words: Highly mis-matched alloys, dilute nitrides, dilute bismides, band anti-crossing model, differential gain, carrier and optical confinement, hydrostatic pressure, transparency and threshold carrier concentration, threshold current density.

ÖZET

YÜKSEK ÖRGÜ UYUMSUZ GaNAsP VE GaNAsBi ALAŞIMLARININ LAZER KAZANÇ MALZEMESİ OLARAK BİLGİSAYARLI MODELLENMESİ

ÜNSAL, Ömer Lütfi
Doktora Tezi, Fizik Mühendisliği Bölümü
Tez Yöneticisi: Prof. Dr. Beşire GÖNÜL
Nisan 2016, 108 sayfa

Bu tez çalışmasının amacı, yüksek örgü uyumsuz alaşımlardan GaNAsP ve GaNAsBi'ın modelleme ile elektronik bant yapılarını ve akım yoğunluklarını araştırmaktır. Yüksek örgü uyumsuz alaşımların önemini ortaya çıkarmak için GaNAsP ve GaNAsBi ile N katkısız muadillerini içeren karşılaştırmalarını sunmaktayız.

Bant yapısı itibariyle doğrudan ışıma yapabilen GaP altlıklı seyreltik nitrit Ga(NAsP) lazer diyotlarının, Si mikroişlemciler üzerine monolitik entegrasyonu önem kazanmaya başlamıştır. Yeni önerilmiş bu lazer malzeme sisteminin en büyük avantajı GaP ile silisyumun örgü sabitleri arasındaki uyumsuzluğun çok az olmasıdır. Ancak yakın zamanda elde edilen ölçümler, Ga(NAsP)/GaP kuantum kuyu lazerlerinin yüksek eşik akım yoğunluğuna sahip olduğunu göstermiştir. Bu davranışın sebeplerini irdelemek amacıyla, bizde model hesaplamalar ile doğrudan ışıma yapabilen Si altlıklı seyreltik nitrit Ga(NAsP) lazer diyotların, eşik akım yoğunluklarının kapsamlı bir analizini sunduk. Hesaplamalarımız ile deneysel sonuçlarının karşılaştırılması, Auger CHCC mekanizmasının 300K de baskın kayıp mekanizması olduğunu işaret etmektedir.

Yakın zamanda yapılan ölçümler birçok özgün elektronik özellik sergileyen, yüksek örgü uyumsuz yarıiletken alaşımlarından $GaAs_{1-x}Bi_x$'ın, artan x ile yasak enerji aralığının hızla azaldığını ve spin-yörünge etkileşim enerjisininde güçlü bir şekilde arttığını göstermiştir. Bu nedenle GaNAsBi'ın yasak enerji aralığındaki hızlı azalışın kaynağını ve sonuçlarını anlamak için yasak enerji aralığı ve kritik kalınlığı üzerinde çalıştık ve karşılaştırmalar yaptık. Elde edilen sonuçlar GaNAsBi malzeme sisteminin, optoelektronik uygulamalarda uzun dalga boyu bölgesinde kullanılabilinir olduğunu göstermiştir.

Anahtar kelimeler: Yüksek örgü uyumsuz alaşımlar, seyreltik nitritler, seyreltik bismitler, anti bant geçiş modeli, diferansiyel kazanç, taşıyıcı ve optiksel hapsolma, hidrostatik basınç, geçirgenlik ve eşik akım taşıyıcı yoğunlukları, eşik akım yoğunluğu.

I dedicate this work to the glamour of science...

ACKNOWLEDGEMENTS

I would like to express my special appreciation and thank to my advisor Prof. Dr. Beşire GÖNÜL for being a tremendous mentor, superior assistance and encouraging me in the best way throughout my study.

My sincere thanks also goes to Assist. Prof. Dr. Nuran DOĞRU and Assoc. Prof. Dr. Hüseyin TOKTAMIŞ for unique constructive criticism, insightful comments and priceless opportunities on improving my qualifications.

I would like to thank my friends Sedat ÖZTÜRK, Ajda ÖZTÜRK, Ebru BAKIR KANDEMİR, Zekeriya UYSAL and Uygar ŞAŞMAZ for their intimately friendship and supports.

This work is supported by TUBITAK (Scientific and Technical Research Council of Turkey) under Grant no 113F407.

TABLE OF CONTENTS

Page

LIST OF TABLES

Page

LIST OF FIGURES

Page

LIST OF SYMBOLS

e : Electron charge

$\hbar$: Planck's constant

k_B : Boltzmann's constant

T : Temperature

E_g : Band gap(eV)

Δ_0 : Spin-orbit splitting(eV)

C_{11} : Elastic Stiffness constant(GPa)

C_{12} : Elastic Stiffness constant(GPa)

C_{44} : Elastic Stiffness constant(GPa)

b : Deformation potential(eV)

a_0 : Lattice constant Å

m_e^* : Electron effective mass

a_c : Hydrostatic deformation potential for conduction band

a_v : Hydrostatic deformation potential for valence band

γ_1 : Luttinger parameter

γ_2 : Luttinger parameter

γ_3 : Luttinger parameter

$E_{v,av}$: Average Valence Band Energy

α : First order pressure derivative (10^{-2} eV/GPa^2)

β : Second order pressure derivative (10^{-4} eV/GPa^2)

E_p^2 : Interband Matrix Element(eV)

λ_g : Refractive Index

χ : Electronegativity

h_c : Critical Thickness

Γ : Optical Confinement Factor

CHAPTER 1

INTRODUCTION

In the span of last two decades, research into so called "dilute nitride" opto-electronic semiconductor material systems has produced much attraction, due to the interesting physics and applications which includes a large bandgap bowing and an increase in electron effective mass with only a few percent of incorporated nitrogen. These in turn enable telecommunications wavelength lasers to be grown and a potential for more efficient solar cells. Also acknowledging the fact that silicon being as a low cost material for electronic circuit applications has led to a desire to combine the advantages of optical data processing with the mature silicon microelectronics technology. This merging of technologies is essential to keep up with the ever increasing need for bandwidth in optical inter- and intra-chip connections.

More recently, GaP-based dilute nitrides drew attraction where additional interesting phenomena and applications can also be explored. The GaP-based dilute nitride direct bandgap material Ga(NAsP) is gaining importance for the monolithic integration of laser diodes on Si microprocessors. The major advantage of this newly proposed laser material system is the small lattice mismatch between GaP and Si (less than 0.4% at room temperature) allowing the growth of GaP on Si without dislocations. Recently, lasing operation at room temperature in Ga(NAsP)/GaP quantum well (QW) laser has been demonstrated and the first gain measurements emphasised that material properties of these novel Ga(NAsP) material system were comparable to standard III/V material systems applied in commercial laser diodes. However, the presence of large threshold current density J_{th} in these promising laser diodes on Si substrates needs to be better understood in order to optimize and improve the device performance.

It is known that applied hydrostatic pressure changes the band structure of semiconductor alloys qualitatively without changing the crystal symmetry. Since the loss mechanisms in semiconductor lasers are strongly wavelength dependent,

hydrostatic pressure provides a convenient method to vary the band structure of semiconductor lasers continuously. In this thesis we aim to present a theoretical investigation of the threshold current density of type-I direct bandgap $GaN_xAs_{1-x-y}P_y$/GaP QW lasers on GaP and hence on Si substrates. By means of using the reported pressure coefficients of bandgap of the constituent binary materials, pressure dependence of effective mass, optical confinement factor, transparency and threshold carrier density, threshold gain, differential gain will be calculated for idealized band models. These in turn allow us to determine Radiative and Auger recombination processes which contribute to the threshold current. It is known that Radiative and Auger recombination processes limit the device performance. We believe that this detailed analysis would clarify some unanswered questions concerning with the literature and foresee the superiority or the weakness of the GaP-based dilute nitride direct bandgap material system of Ga(NAsP)/GaP on GaP substrates. We expect that these model calculations will lead to a valuable contribution to the related area in which the interest has been growing up nowadays. To the best of our knowledge the present study is the first that introduces a theoretical calculation of the pressure dependence of the threshold current density of the quaternary $GaN_xAs_{1-x-y}P_y$ well material with GaP barriers on GaP and hence on Si substrates.

This thesis begins with the basics of semiconductor physics focusing on semiconductor alloying and bandgap engineering. It is accepted that change in bandgap can be explained by a linear interpolation of constituent semiconductors for most of the semiconductor alloys. Therefore we present Vegard's law to describe the variation of bandgap by alloying binary or ternary semiconductors. We next provide a description of the highly mismatched alloys (HMAs) and its anomalous properties with a discussion of isoelectronic impurities. We then focus on the history of $GaN_xAs_{1-x-y}P_y$ alloy which is one of the most notable and new example of HMAs. Finally, we present the dramatic change of the electronic band structure of As- and N-rich $GaN_xAs_{1-x-y}P_y$ alloys which cannot be explained by Vegard's law but with band anti-crossing (BAC) model.

Chapter 3 presents the analysis of band structure and critical thickness of $GaN_xAs_{1-x-y}P_y$ QWs on Si substrates. Starting with the electronic band structure of $GaN_xAs_{1-x-y}P_y$ alloy, concentration dependence of conduction band edge energy levels and effective mass for N and P incorporation is theoretically investigated. Results indicate that the conduction band edge narrows with increasing N concentration and decreasing P concentration. Thus, to obtain light in the long wavelength region $GaN_xAs_{1-x-y}P_y$/GaP can be a suitable material system. Variation in the effective mass due to N concentration brings improvement as

the electron effective mass approaches to a value that is comparable of hole's. Then, we introduce Model Solid Theory which enable us to investigate the band alignment of the $GaN_xAs_{1-x-y}P_y$ material system on GaP and AlGaP barriers. Introducing N into host material system GaAsP, changed the band offset of the $GaN_xAs_{1-x-y}P_y$ drastically. With increased N concentration, deeper conduction band offset values obtained. This translates into better confinement of free charge carriers in the $GaN_xAs_{1-x-y}P_y$ QWs designed on GaP barriers. Low level P concentration proved to be suitable since an increase in P concentration yields decreased conduction band offset energy values. Finally, the phenomena of critical thickness is investigated for GaNAs and GaNAsP on Si substrates. Positive effects of N is also seen in the critical thickness calculations. It is also illustrated that the incorporation of N improves the strain value of $GaN_xAs_{1-x-y}P_y$ on GaP substrates.

We have investigated Ga(NAsBi) material system in chapter 4 by means of considering the effects of Bi incorporation on the electronic band structure and critical thickness on GaAs substrates. Explaining the interaction between Bi and GaNAs host material, valence band anti-crossing model is introduced. This interaction causes valence band to split into two subbands, a similar phenomena occurred in Ga(NAsP) which is between N and GaAsP conduction band. Bi concentration dependence of valence band edge energy levels are investigated for $GaN_xAs_{1-x-y}Bi_y$ on GaAs substrates. Our theoretical calculation on the concentration dependence of $GaN_xAs_{1-x-y}Bi_y$ QWs resulted in obtaining bandgap energies corresponding to $1.33\mu m$ and $1.55\mu m$. These calculated results for this material system shows that $GaN_xAs_{1-x-y}Bi_y$ is lattice-matched on GaAs substrates with a ratio of $y \cong 1.7x$, and therefore possible strained induced growth effects can be disregarded.

Chapter 5 introduces a theoretical investigation of optical confinement factor of Ga(NAsP) based quantum wells. We examine how the refractive index of Ga(NAsP) material is affected by nitrogen and phosphide concentration and the wavelength of incoming photon. A comparative study of optical confinement factor of GaAsP and Ga(NAsP) wells is undertaken by means of considering the refractive index differences between the well and that of barrier and cladding layer. Refractive index calculations are performed by using Adachi's model and optical confinement factor is calculated by five-layer symmetric slab model.

The focus of chapter 6 is to investigate material gain properties of Ga(NAsP) /GaP QWs by comparison with that of GaAsP/GaP material system. The changes in the band structure, effective mass and optical confinement factor with

concentration dependence are quantified, and their effects on carrier and current density analysed. It is found that the reduction in the threshold carrier density can be achieved by incorporating Al into cladding layer. Both transparency and threshold carrier density degrades with increased N and P concentration.

In the long wavelength region, laser material systems suffer heavily from intrinsic loss mechanism which is due to Auger recombination mechanism. An important parameter in determining the direct Auger rates is the minimum of threshold energy that carriers must have to instigate the Auger process. We present in chapter 7, a comprehensive theoretical analysis of threshold current by employing hydrostatic pressure in dilute nitride Ga(NAsP)/GaP QWs using model calculations. The pressure dependence of band structure, radiative and non-radiative recombination rates, optical confinement factor, transparency- and threshold-carrier densities are calculated in a range of 0-1 GPa at room temperature. It is found that incorporation of N into GaAsP reduces the non-radiative Auger recombination rates which brings an improvement in threshold current. The comparison of our calculated results with that of the experimental data indicates that the Auger effect involving CHCC process can be considered as the dominant non-radiative loss mechanism at 300K.

Finally, a summary of the thesis work is provided in chapter 8.

CHAPTER 2

THEORY AND FUNDAMENTAL CONCEPTS / THE PHYSICS BEHIND INCORPORATION OF NITROGEN INTO Ga(NAsP)

2.1 Introduction

The objective of this chapter is to supply necessary information on the fundamental theoretical background of this dissertation. For this purpose, we firstly overview the bandgap engineering of semiconductor compounds. Secondly, we introduce the III-N-V based highly mismatched alloys covering the basic definitions. Thirdly historical background of Ga(NAsP) alloy is covered. Finally, we present GaN_xAs_{1-x} and GaN_xP_{1-x} alloys and theoretical models which can describe the novel properties of III-N-V based Ga(NAsP) HMAs.

2.2 Semiconductor Alloys and Bandgap Engineering

Currently, III-V semiconductor alloys are employed in electronic devices due to the fact that the technology for these alloys have matured over the decades. Therefore, usage of III-V semiconductor alloys as material basis for a number of commercial applications, including high-electron-mobility and heterostructure bipolar transistors, diode lasers, light-emitting diodes, photodetectors, electro-optic modulators etc. is very common. In addition to the binary compounds, more complex material compositions such as ternary and quaternary alloys allow almost endless variety of material configurations to be designed.

The operating characteristics of optoelectronic devices are defined by the physical properties of materials composition. Thus, engineering the material composition one can achieve tailoring the materials properties like the electronic structure or optical behaviour of semiconductor alloys which carries great significance.

Figure 2.1 shows the lattice parameters, bandgaps and their corresponding wavelengths for common elemental and binary semiconductors. Hexagonal and cubic crystal structures are represented by hexagon and square symbols, respectively. Lattice constants are determined by the magnitude of interatomic forces in between the constituent atoms of material. Electrons that fill the outermost shell of these atoms characterize the strength of chemical bonds and the value of lattice parameter. Stronger the chemical bonds in between the constituent atoms, smaller the lattice parameter thus a large bandgap enrgy is observed from the material.

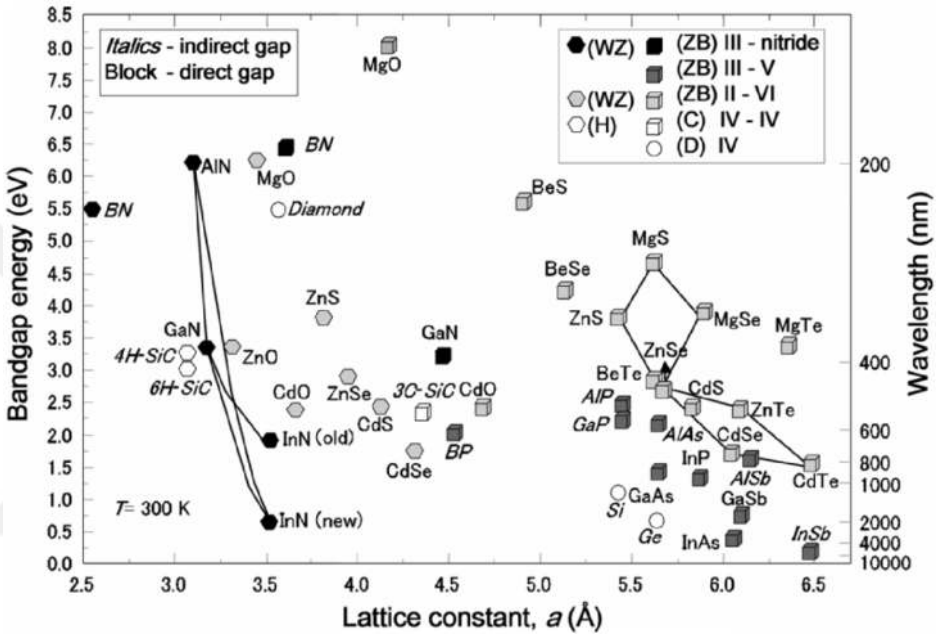

Figure 2.1: Band gap versus lattice constant for some well known semiconductors. The right-hand scale gives the light wavelength λ corresponding to the bandgap energy at 300K [1].

The lines on Figure 2.1 indicates ternary compounds which are alloys of the constituent binaries labelled at their end-points. Direct and indirect bandgap semiconductors materials are shown in plain and italic text, respectively. A direct bandgap is more efficient than an indirect bandgap at emitting and absorbing light, because direct bandgap transitions are between electrons and holes whereas a phonon is needed to achieve these transitions in an indirect semiconductor.

Application of semiconductor materials corresponding to these binary and ternary compounds and their alloys are shown in Figure 2.2. With the advancement of semiconductor alloying technology, optical discs are born. Firstly, Compact Disc(CD) which is composed of a ternary compound of AlGaAs, ranged

from infra-red to green depending on the proportion of the Al, were introduced. Later, Digital Video Disk (DVD) was introduced which is a quaternary alloy of AlGaInP. And recent years, Blu-Ray Discs (BRD) are the mainstream optical storage of choice which is born from GaN semiconductor alloys.

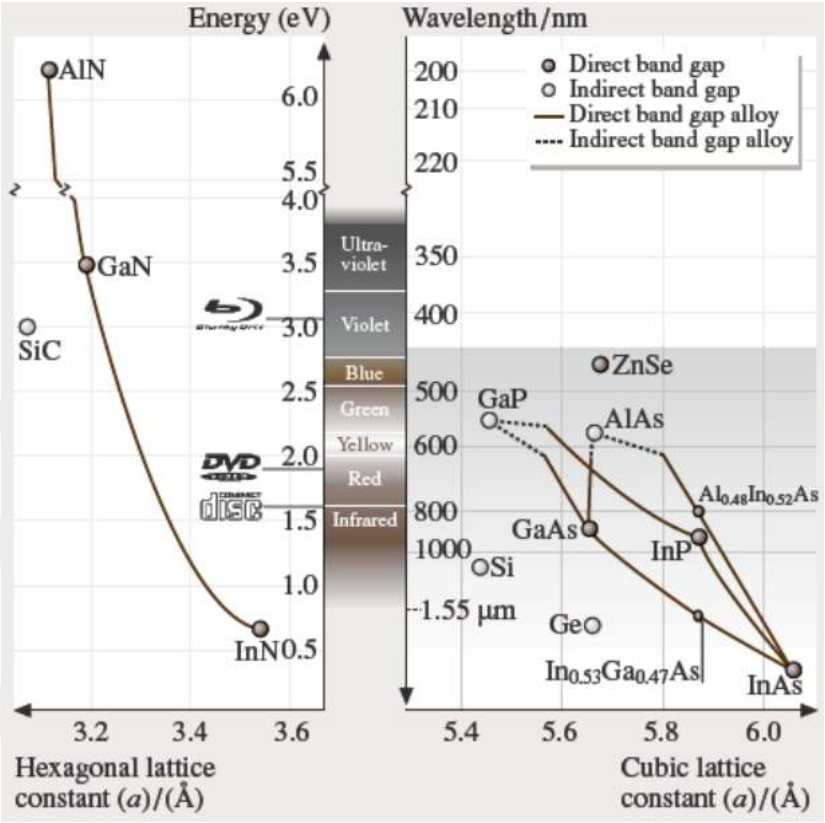

Figure 2.2: Parameter perspective: bandgaps and lattice parameters of selected some semiconductors. The significant wavelengths corresponding to optical storage (CD,DVD and Blu-Ray) and the 1.55 μm used for efficient data transmission through fibers are labelled [2].

A semiconductor alloy is a combination of two or more elements. If an alloy has two component than it is called a binary alloy, for one with three is a ternary alloy, for one with four is a quaternary alloy. An alloy is formed from a physical mixture of two or more substances, while a compound is formed from a chemical reaction. For example, GaN is a compound consisting of Ga atoms bonded to N atoms. However, $GaN_xAs_{1-x-y}P_y$ is an alloy compound consisting of GaN,GaAs and GaP with a mole fraction of x, (1-x-y) and y respectively.

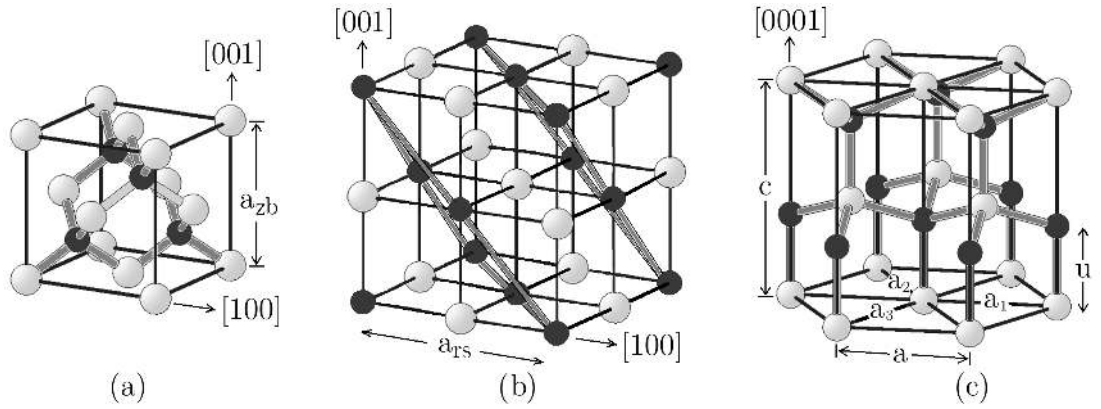

Figure 2.3: The crystal structures of a) zincblende b) rocksalt and c) wurtzite structures. Larger and smaller spheres represent anions and cations, respectively.

Figure 2.3 illustrates the cubic (diamond and zincblende), rock salt (NaCl) and hexagonal (wurtzite) structures which are represented by the hexagon and square symbols in Figure 2.1. The diamond, zinc blende and wurtzite structures are the three most common crystal structures of semiconductors. Zincblende structure consists of two interpenetrating face-centred cubic (fcc) lattices offset along the body diagonal by one quarter of the length of the diagonal. For binary compounds, atoms A and B represent different elements (zinc blende structure) and for elemental semiconductors atoms A and B represent the same element (diamond structure). Wurtzite is similar to the zinc blende structure, both are fourfold coordinated, except that the former has a hexagonal close-packed (hcp) bravais lattice rather than fcc. In Rock-salt crystal structure, Figure 2.3(c), each of the two atom types A and B forms a separate face-centered cubic lattice, with the two lattices interpenetrating so as to form a 3D checkerboard pattern.

The bandgap of a semiconductor is dependent on the lattice parameter and electron phonon interaction; therefore, the temperature dependence of the bandgap is related to the thermal expansion of the lattice and the temperature effects is related to the electron-phonon interaction. Traditionally, the change of the band-gap energy due to temperature variation E_g is expressed in terms of the Varshni formula [3] as shown in Eqn. 2.1:

$$E_g(T) = E_g(0) - \frac{\alpha T}{T + \beta} \tag{2.1}$$

where $E_g(0)$ is the bandgap energy at $T = 0$ K, α is in electron-volts per Kelvin and β is closely related to the Debye temperature of the material (in Kelvin).

The bandgap change with alloying are generally linear or have a constant curvature. This linear behaviour can be explained by Vegard's law [4] which states that the energy gap of a semiconductor alloy is calculated by a linear interpolation of the energy gap of the constituent semiconductors. Linear interpolations are suggested for the electron masses in X and L valleys, split-off hole mass, and heavy-hole and light-hole masses along [001] direction. The lattice constants and elastic moduli may be linearly interpolated. The energy gap can thus be expressed for AB_xC_{1-x} alloy as a function of $E_{g(AB)}$ and $E_{g(AC)}$ energy gaps respectively:

$$E_{g(AB_xC_{1-x})}(x) = xE_{g(AB)} + (1-x)E_{g(AC)} \tag{2.2}$$

where $E_{g(AB)}$ and $E_{g(AC)}$ the bandgaps of the binary constituents AB and AC. For some material parameters, however, energy gap calculations deviate largely from the linear relation of Eqn. 2.2. In this case, semiconductor alloys can usually be described by a quadratic polynomial in concentration x with the quadratic coefficient being called the bowing coefficient. Such as;

$$E_{g(AB_xC_{1-x})}(x) = xE_{g(AB)} + (1-x)E_{g(AC)} - x(1-x)C_{(AB_xC_{1-x})}. \tag{2.3}$$

The bandgap bowing coefficient C describes the deviation from linearity and is close to a constant for most alloys. For most III-V alloys bandgap is typically smaller than the linear interpolation result and so C is positive. Typically the magnitude of C is not dependent on the composition of the material.

Electronegativity

Ability of an atom to attract electrons towards itself in a covalent bond [5] is called electronegativity and represented by the symbol χ. Atomic weight and the valance electrons are the deciding factors of an atom's electronegativity. Greater the related electronegativity value, the more an element or compound attracts electrons towards itself. Metals are electropositive since they give out their valance electrons when they bond. Non-metals are electronegative since they take in valance electrons from other atoms when they bond.

Measuring electronegativity cannot be done directly and must be calculated from properties of atoms or molecules. Electronegativity, as it is usually calculated, is not strictly an atomic property, but rather a property of an atom in a molecule [6]. Several methods of calculation have been proposed using physical parameters including enthalpy data, ionisation energy and electron affinity, effective nuclear charge and covalent radius etc., although there may be small differences in the numerical values of the electronegativity, all methods show the

same periodic trends between elements. Due to the importance of Paulings scale [6] where electronegativity ranges from Cs, $\chi = 0.7$ to F, $\chi = 4.0$, all the other electronegativity scales are routinely normalised with respect to Paulings range. Strong correlations between numerous atomic parameters, physical and chemical, the term electronegativity integrates them into a single dimensionless number between 0.78 and 4.00 that can be used to predict much of an elements physical character and chemical behaviour.

Element	**Electronegativty**
C	2.55
B	2.04
Si	1.90
Ga	1.81
P	2.19
N	3.05
As	2.18

Table 2.1: Electronegativity values for dopant semiconductors [7].

2.3 Highly Mismatched Alloy

Typical semiconductor alloys are formed from elemental semiconductors with similar atomic radii and electronegativity (e.g., AlGaAs, GaAsP). However, over the last decade, it has been well established that the isoelectronic substitution of anions with very different ion size and/or electronegativity can result in dramatic restructuring of the electronic bands of semiconductor alloys. Semiconductor alloys which exhibit this phenomena have been known as highly mismatched alloys (HMAs) [8]. HMAs include a class of III-V and II-VI compound semiconductors such as GaN_xAs_{1-x}, GaN_xP_{1-x}, $GaBi_xAs_{1-x}$, $GaSb_xAs_{1-x}$, ZnS_xTe_{1-x}, $ZnTe_xSe_{1-x}$ and ZnO_xTe_{1-x}. Because of large miscibility gaps, typically HMAs consist of a host semiconductor matrix with the substitution of only a small amount of distinctly different isovalent atoms. For example, dilute III-V nitrides (up to $\sim 10\%$) shows unusual effects such as

- localization of states near the conduction band minimum (CBM)
- giant bandgap bowing, and
- composition dependent bowing.

This is in contrast to conventional semiconductor alloys such as GaAsP and AlGaAs whose physical, electronic, and optical properties can be deduced from a linear interpolation between their corresponding end point compounds with only a slight deviation, as predicted by Vegard's Law. The properties of highly mismatched alloys (HMAs) deviate drastically from the predictions of Vegard's Law. The unusually strong dependence of the fundamental gap on the N content in the group III-N-V alloys has been well described by the anti-crossing interaction between localized N states and extended conduction band states of the III-V matrix [8, 9, 10]. This model which can accurately describe the composition and pressure dependencies of the fundamental bandgaps of HMAs is called Band Anti-crossing (BAC) that will be provided in section 2.4.1.

Isoelectronic Impurities

Isovalent or isoelectronic impurities are known as the substitutional impurity which has the same valence as the substituted atoms in the host lattice. Although they have the same valency, the impurity atom may differ from the host atom in many other aspects, such as a different atom size and electronegativity which results a dramatic restructuring of the electronic bands of semiconductor alloys.

Element	**Covalent radius(Å)**	**Ionic radius(Å)**
Si	1.17	-
Ga	1.25	-
In	1.5	-
N	0.7	-
P	1.1	-
As	1.21	-
Al	1.25	-
O	-	1.4
Ti	-	0.745
Zn	-	0.74

Table 2.2: The radii of elements based on their bonding type [11, 12].

The radii of commonly used elements in semiconductors material systems are shown in Table 2.2. Measured radius of two atoms touching together when put in a very close proximity is called the covalent radius. There are two defining factors of ionic radii; ionization degree of an atom and the number of neighbouring

atoms are the two characterizing factors of ionic radii. The length of an ionic bond reflects a balance between the electrostatic Coulomb attraction of the unlike charges and the mutual Born repulsion of the positively charged nuclei.

Table 2.3 presents the classification of the semiconductor alloys in three categories according to the difference in the electronegativities between host and substituted atoms (isovalent atoms). Isovalent/impurity atom creates a perturbation to the host band structure. This perturbation is usually small, hybridizes with the host states and remains unnoticeable. But if electronegativity, size and ionization energy difference are big, these impurity atoms can act as a deep center with a localized potential. For example, substituting In for Ga or P for As in GaAs produces a very weak perturbation whereas substituting N for P in GaP produces excitonic bound states. Isovalent impurities creating bound states are generally referred to as isoelectronic impurities and impurities attractive to electrons and holes are often termed as pseudo-acceptors or pseudo-donors, respectively. Creating a highly localized center is attractive to one type of carrier via a short-range potential. The trapped carrier can subsequently bind a carrier of opposite charge via coulombic interaction. Therefore, an isoelectronic impurity can bind excitons [13].

Highly Mismatched Alloys	**Electronegativity difference (eV)**
II-O-S	1.0
II-O-Se	1.1
II-O-Te	1.4
III-N-As	1.0
III-N-Sb	1.2
III-N-P	0.9
Moderately Mismatched Alloys	**Electronegativity difference (eV)**
II-S-Te	0.4
II-Se-Te	0.3
Lightly Mismatched Alloys	**Electronegativity difference (eV)**
II-S-Se	0.1
III-P-As	0.1

Table 2.3: Electronegativity difference and mismatched classification for some semiconductors [14].

The energy levels of dopant atoms are not sensitive to the positions of conduction and valence band edges since the deep states have localized wavefunctions in real space which may involve Bloch functions from several bands

over a large region of k-space. Thus it is not expected to shift significantly in energy with a change in composition or pressure [10]. To calculate the energy positions of these deep levels, one needs to know the defect potential and then solve the corresponding Schrödinger equation. In many cases the exact functional form of the localized potential is not very crucial; the deep centre wave-function is predominantly determined by the host crystal rather than by the deep impurity. The main difficulty of the problem lies in the second step, i.e., finding the solution to the Schrödinger's equation. In 1980, Hjalmarson et al. made the first systematic theoretical investigation of this problem [15]. Employing a Koster-Slater model for the localized potential, they established the eigenvalue equation in a tight-binding-function basis.

2.4 History of Ga(NAsP) Alloys

The time and interest devoted to the research on Ga(NAsP) material systems have increased since the discovery of rapid bandgap reduction in GaNAs due to incorporation of N dopants [23, 24, 25]. This discovery quickly escalated the need of finding suitable substrate for GaNAs material system. With the incorporation of P into GaNAs not only provided a closer lattice match to GaP, but also to Si, and broadened the variation range of the bandgap that can be engineered. The emerging material system is Ga(NAsP) which is a promising application for 1.3–1.55 μm telecommunications devices[26].

Replacing of a small portion of the group V atoms in such as phosphide, arsenide or antimony in III/V compound semiconductors by nitrogen creates isoelectronic impurities, which form localized electronic states in the vicinity of dopant atoms, i.e. at small N concentrations. Figure 2.4 illustrates schematics of the positions for each energy level including GaAs, GaP and the localized N levels. Effects of N incorporation can be seen as the formation of N-induced energy states in GaNAs and GaNP. Event though both GaAs and GaP are zinc-blende semiconductor materails, at the Γ point of the Brillouin zone GaAs exhibits direct- whereas GaP indirect-transitions. The localization of dopant N atoms occur in the conduction band of GaAs, whereas in GaP these dopant atoms localize below the conduction band minima. Although $GaAs_{1-y}P_y$ alloy can be formed over the entire composition range y, for $y > 0.45$ [27] the bandgap becomes indirect. N dopant level is localized in the conduction states of $GaAs_{1-y}P_y$ for $y < 0.35$ and for $y > 0.35$ then N dopant states localizes below the conduction band minima [17, 28].

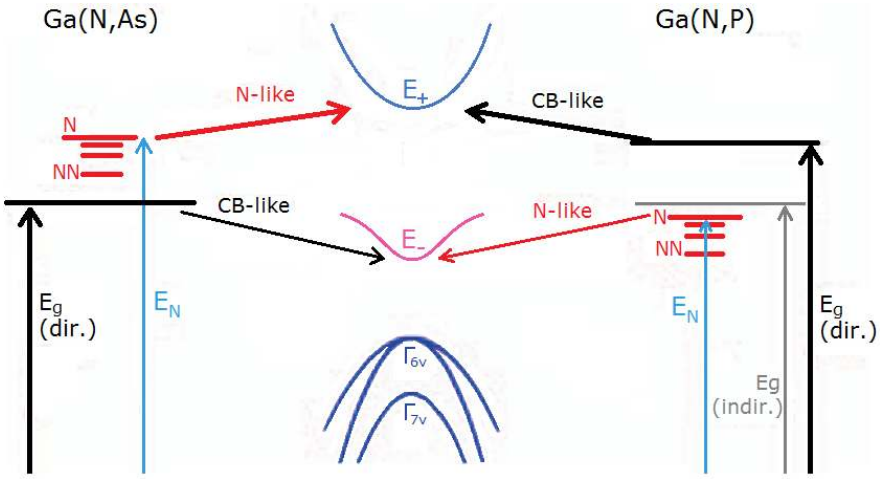

Figure 2.4: Band diagram of GaAs:N and GaP:N showing the effects of N incorporation, namely isolectronic impurities in GaAs and GaP binary semiconductors [10].

The potential which $GaN_xAs_{1-x-y}P_y$ would add into semiconductor technology was soon recognized and first steps were taken towards the realization of this efficient optoelectronic devices. When crystal growth could only be achieved by equilibrium methods in 1960s, diodes emitting green light were produced from GaP materials doped with N atoms. Because, excitation of electrons into the localized N states and then achieving radiative recombination of those excitons which are bound to N dopants is very efficient [29]. This phenomena occurs due to N dopants localizes below the conduction band minima of GaP and therefore these localized states serving as the new conduction band minima for the radiative transitions. These localized N dopant states was discovered by the help of photoluminescence spectroscopy [17, 30]. Shortly after, LEDs with emission energies in the range of 1.8 - 2.2 eV, which covers from red to yellow colour spectrum range, was fabricated from $GaAs_{1-x-y}P_y$:N material [31]. Direct ($y < 0.45$) and indirect ($y > 0.45$) stimulated emission of N dopant states from optically pumped $GaAs_{1-y}P_y$:N material was reported for the concentration of P being always around $y = 0.45$ [32, 33]. However in a similar experiment on N dopant states of GaP:N material, stimulated emission and gain were not observed [34].

As shown in Figure 2.4 N dopant states lies (about 200 meV above of conduction band minima) within the conduction band of GaAs. Additionally, bandgap transition-wise GaAs exhibit direct bandgap in contrast to GaP's indirect band gap. Therefore, there was no significant contribution from these N dopant states as it is in the GaP [35]. As a result, GaAs materials doped

with N atoms found place in optoelectronic application in later years. Doping concentrations of N have to exceed for GaAs:N to exhibit new emission characteristic for optoelectronic semiconductor applications. These doping concentrations was achieved in the early 1990s by the use of advanced non-equilibrium growth techniques; molecular beam epitaxy (MBE) and metalorganic vapour phase epitaxy (MOVPE) [25, 36]. It was demonstrated that increasing N concentration in GaNAs results a huge bowing in the bandgap in contrast to N free amalgamation-type III/V semiconductor allos i.e. AlGaAs, InGaAs or GaAsP [36, 37]. Incorporation of N into GaAs with accordance to Vegard's law of linear interpolation, one would expect blueshift since GaN having bandgap energy nearly 2 eV larger than that of GaAs. However redshift was observed [38, 39]. This phenomena was interpreted in terms of a repulsive interaction between conduction band minima states of host material GaAs and localized N dopant states. A simple two level model which is called band anti-crossing (BAC) model was successfully applied to parametrise N concentration dependence of bandgap energies of N containing semiconductor materials x [9]. Soon after the successful growth reports of GaN_xAs_{1-x} was received with the observation of extensive material parameter engineering by the incorporation of N, it was realized that the GaNAs and the related GaInNAs material systems are providing unique applications in optoelectronic devices [40]. Indeed, GaInNAs has now been demonstrated to be suitable as the active material of vertical-cavity surface-emitting lasers and edge-emitting lasers emitting at the wavelength region of 1.3 and 1.55 μm which is suitable for signal transmission over long-distance through optical fibers [40, 41]. Using the simple BAC model and its extension to a 10 band $k \cdot p$ Hamiltonian, electronic states of these material systems are calculated. These models describe well many of the major features of new N doped class of semiconductor alloys, including the low pressure coefficients of the bandgap energy, the optical gain spectra and the fact that there is a N-induced increase of the electron effective mass [42, 43], although the BAC model underestimates the experimentally observed increase in effective mass across a wide range of GaNAs samples [44, 45].

Non-equilibrium techniques used for the growth of GaNAs were also successfully applied to GaNP materials for increasing the incorporation percentage of N atoms [46, 47]. GaN_xP_{1-x} LED structures containing up to 1% N doping in the active region were soon fabricated [48, 49]. Since GaNP is a GaP based material the question of it being suitable as an active material on Si (GaP and Si has nearly-matched lattice constants) substrates for laser structure arose. Recent results of modulation spectroscopy reveal that model calculation of band structure analysis of the transitions in GaNP does not change with N concentration.

However, by increasing N concentration the Γ character of transitions stays distributed over a large variety of energy gaps originating from the localized states of N atoms in different spatial configurations [50].

2.4.1 Band Anti-crossing Model

Conduction Band Anti-crossing Model

Shan et al. [9] have shown that unusual behaviours of HMAs can be quite well understood within a simple band anti-crossing (BAC) model. The model explains the properties of HMAs, including the composition and pressure dependence of the bandgap, the presence of a new high energy transition and a nitrogen-induced enhancement of the electron effective mass. The BAC model treats the interaction of the localized defect states and the extended states of the conduction band in analogy to perturbation theory for a two-level system. This interaction leads to a splitting of the matrix band into two characteristic nonparabolic bands that are typically labeled E_+ and E_- for the high and low energy bands respectively. The resulting bands have mixed localized and delocalized character from the interaction of the two types of states [51].

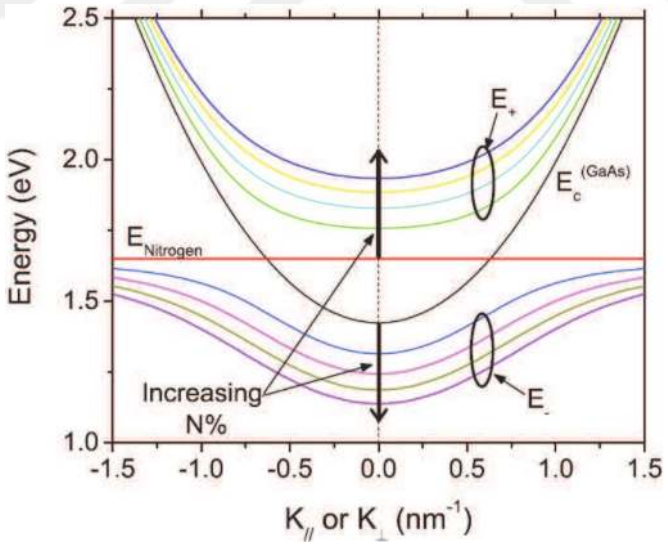

Figure 2.5: Illustration in k-space of the band anticrossing effects on the nitrogen level and GaAs conduction band [52].

The alloying of an HMA can be treated as an anti-crossing interaction if it is assumed that the defect states are randomly distributed over the lattice, replace the anion sites, and are weakly coupled to the host lattice. First for the

case of the substitution of a more electronegative anion into the lattice results in an energy level close to the conduction band. The eigenvalue problem for the perturbed system can be written as:

$$\begin{vmatrix} E_M(k) - E(k) & V_{MD} \\ V_{MD} & E_D - E(k) \end{vmatrix} = 0 \tag{2.4}$$

where $E_M(k)$ is the dispersion relation for the unperturbed host conduction band, E_D is the defect energy level, *E(k)* is the dispersion relation of the perturbed system that are all relative to the valence band edge (VBE). $E_{MD} =< k|V|D >$ is the matrix element describing the coupling between the localized defect states, D, and the extended host matrix conduction band states. The matrix element, V_{MD}, can be simplified to $C_{MN}x^{1/2}$ assuming that the defect states are randomly distributed and their concentration is low enough so there is no appreciable defect state wavefunction overlap. C_{MN} is an empirically determined coupling constant between the extended matrix states and the localized defect states and x is the mole fraction of the defect. The solution to Eqn. 2.4 is then

$$E_{\pm}(k,x) = \frac{E_M(k) + E_D \pm \sqrt{(E_M(k) - E_D)^2 + 4xC_{MD}^2}}{2} \tag{2.5}$$

so the original system of a parabolic band and a localized defect level results in a splitting into two highly non-parabolic bands, $E_+(k)$ and $E_-(k)$, that depend on the composition, x. $E_-(k)$ becomes the new conduction band dispersion relation of the alloy and defines the bandgap. Figure 2.5 shows the GaN_xAs_{1-x} where the defect level is resonant with the conduction band. As the alloying is increased, the separation between $E_+(k)$ and $E_-(k)$ increases and the bandgap decreases as can be seen in Figure 2.5.

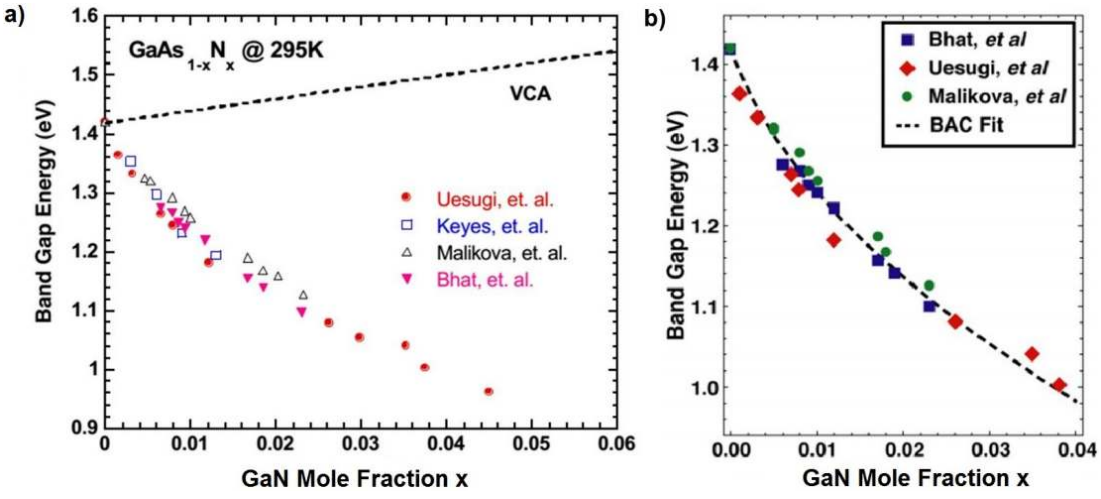

Figure 2.6: Measured bandgap of GaN_xAs_{1-x} as a function of x and its comparison with a)VCA [14] and b) BAC model [51].

The composition dependence of the bandgap of GaN_xAs_{1-x} according to measurements and virtual crystal approximation and BAC model are shown in Figure 2.6(a) and (b), respectively. As can be seen clearly the bandgap dependence deviates significantly from the VCA prediction. Even the trend of the change in the bandgap is reversed from the VCA dependence on the As-rich side. While the VCA predicts a slight increase in the bandgap, it is observed the bandgap energy dropping rapidly as a function of N concentration. If we use Eqn. 2.3, in the As-rich side a huge bowing parameter (more than 14 eV) is required to express this strong composition dependence by a quadratic polynomial with x up to about 0.05, and would predict a negative bandgap for a large range of compositions [14]. However, BAC fits show very good agreement with the experimental data and provide a physical explanation for how alloying with a highly dissimilar anion changes the band structure of the HMA (see Figure 2.6(b)). The BAC has been calculated for the bandgap dependence on composition for GaN_xAs_{1-x} with $C_{MN} = 2.70eV$ and $E_N = 1.65eV$.

Behaviour of anti-crossing effect due to variation of N concentration and temperature on the GaN_xP_{1-x} material system is shown in Figure 2.7. From the obtained experimental results the coupling parameter C_{NM} of GaNP is found to be 2.76 eV which is very close to that of GaNAs, 2.70 eV. These close values of coupling parameters indicate that their origin is similar, e.g. both extended and localized states having comparable hybridization degree. From the temperature measurements at 2K and RT, localized nitrogen energy level E_N is found to be at 2.33 eV and 2.25, respectively.

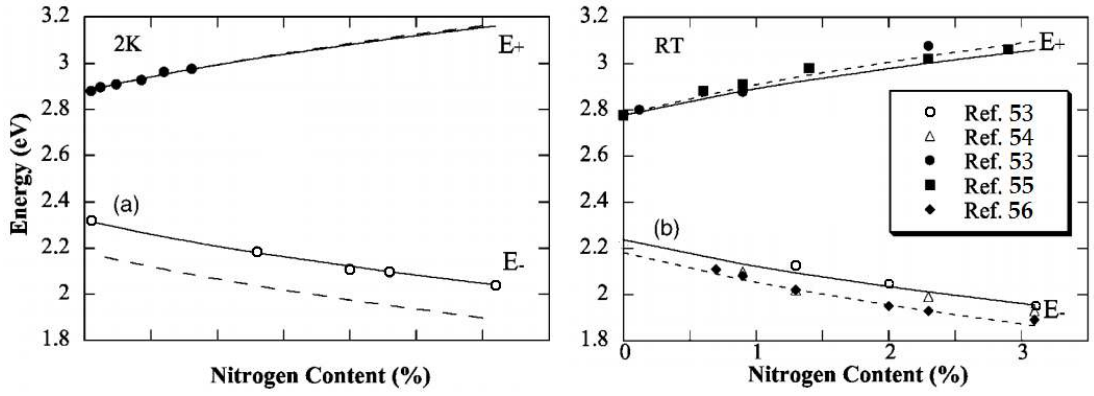

Figure 2.7: Concentration and temperature dependence of band anti-crossing effect on GaNP. Fitting curves are calculated (solid lines) using Eqn. 2.5 and parameters deduced in the Ref. [53] which provide very good agreement with the experimental data (dots) [54, 55]. The E_+ and E_- positions expected from Ref. [56] are shown by the dashed curves.

Valence Band Anti-crossing Model

The complimentary case to the nitrogen defect in GaAs is the arsenic defect in GaN. The more metallic and larger arsenic atom replaces the highly electronegative nitrogen anion. It has been reported that the doping of GaN with arsenic results in a new emission band at about 2.65 eV [57] and the arsenic defect level has been theoretically predicted to lie 0.4 eV above the valence band [58]. Figure 2.6 shows the experimentally determined bandgap for GaN_xAs_{1-x} (GaN-rich), along with the bowing parameter determined for GaN_xAs_{1-x} (GaAs-rich) and the virtual crystal approximation [59]. As GaAs is alloyed with GaN there is a discontinuous decrease in the bandgap as it shifts from 3.4 eV to about 2.6 eV, where the arsenic defect level resides. The bandgap continues to decrease with increasing arsenic concentration. Neither the bowing parameter nor the VCA fit the experimental data.

The full treatment of this system considers the perturbation of the valence band due to the presence of the metallic defects through $k \cdot p$ formalism. The approach is the same as the conduction band anti-crossing model, except that a 6x6 matrix element is needed to describe the valence bands and the p-type defect level. The metallic defects are p-type states with T_2 symmetry, which are represented by a 6x6 matrix. The valence band Hamiltonian is constructed on the basis of the six time-reversal symmetry invariant wavefunctions:

$$\left|\frac{3}{2}, \frac{3}{2}\right\rangle = \frac{1}{\sqrt{2}} |(X + iY) \uparrow\rangle \tag{2.6a}$$

$$\left|\frac{3}{2}, \frac{1}{2}\right\rangle = \frac{i}{\sqrt{6}} |(X + iY) \downarrow -2Z \uparrow\rangle \tag{2.6b}$$

$$\left|\frac{3}{2}, \frac{-1}{2}\right\rangle = \frac{i}{\sqrt{6}} |(X - iY) \uparrow +2Z \downarrow\rangle \tag{2.6c}$$

$$\left|\frac{3}{2}, \frac{-3}{2}\right\rangle = \frac{i}{\sqrt{2}} |(X - iY) \downarrow\rangle \tag{2.6d}$$

$$\left|\frac{1}{2}, \frac{1}{2}\right\rangle = \frac{i}{\sqrt{3}} |(X + iY) \downarrow +Z \uparrow\rangle \tag{2.6e}$$

$$\left|\frac{1}{2}, \frac{-1}{2}\right\rangle = \frac{i}{\sqrt{3}} |(-X + iY) \uparrow +Z \downarrow\rangle \tag{2.6f}$$

Using the standard 6x6 Kohn-Luttinger $k \cdot p$ matrix describing the Γ_7 and Γ_8 valence bands, the random distribution of impurities can be resolved through configurationally averaging within the coherent potential approximation. The 6x6 valence band matrix is enhanced by the 6x6 defect matrix resulting in a

12x12 matrix is given by: $H_v =$

$$\begin{pmatrix}
H & \alpha & \beta & 0 & \frac{i\alpha}{\sqrt{2}} & -\sqrt{2}i\beta & Vx & 0 & 0 & 0 & 0 & 0 \\
\alpha^* & L & 0 & \beta & \frac{iD}{\sqrt{2}} & \sqrt{\frac{3}{2}}i\alpha & 0 & Vx & 0 & 0 & 0 & 0 \\
\beta^* & 0 & L & -\alpha & -\sqrt{\frac{3}{2}}i\alpha & \frac{iD}{\sqrt{2}} & 0 & 0 & Vx & 0 & 0 & 0 \\
0 & \beta^* & -\alpha^* & H & -\sqrt{2}i\beta & -\frac{i\alpha^*}{\sqrt{2}} & 0 & 0 & 0 & Vx & 0 & 0 \\
\frac{i\alpha^*}{\sqrt{2}} & -\frac{iD}{\sqrt{2}} & \sqrt{\frac{3}{2}}i\alpha & \sqrt{2}i\beta & S & 0 & 0 & 0 & 0 & 0 & Vx & 0 \\
\sqrt{2}i\beta^* & -\sqrt{\frac{3}{2}}i\alpha^* & -\frac{iD}{\sqrt{2}} & \frac{i\alpha}{\sqrt{2}} & 0 & S & 0 & 0 & 0 & 0 & 0 & Vx \\
Vx & 0 & 0 & 0 & 0 & 0 & e_d + i\Gamma_d & 0 & 0 & 0 & 0 & 0 \\
0 & Vx & 0 & 0 & 0 & 0 & 0 & e_d + i\Gamma_d & 0 & 0 & 0 & 0 \\
0 & 0 & Vx & 0 & 0 & 0 & 0 & 0 & e_d + i\Gamma_d & 0 & 0 & 0 \\
0 & 0 & 0 & Vx & 0 & 0 & 0 & 0 & 0 & e_d + i\Gamma_d & 0 & 0 \\
0 & 0 & 0 & 0 & Vx & 0 & 0 & 0 & 0 & 0 & e_d + so\Gamma_d & 0 \\
0 & 0 & 0 & 0 & 0 & Vx & 0 & 0 & 0 & 0 & 0 & e_d + so\Gamma_d
\end{pmatrix} \tag{2.7}$$

where

$$H = -\frac{\hbar^2}{2m_o}\left[\left(k_x^2 + k_y^2\right)(\gamma_1 + \gamma_2) + k_z^2(\gamma_1 - 2\gamma_2)\right] \tag{2.8a}$$

$$L = -\frac{\hbar^2}{2m_o}\left[\left(k_x^2 + k_y^2\right)(\gamma_1 - \gamma_2) + k_z^2(\gamma_1 + 2\gamma_2)\right] \tag{2.8b}$$

$$\alpha = \sqrt{3}\frac{\hbar^2}{m_o}\left[k_x(k_x - ik_y)\gamma_3\right] \tag{2.8c}$$

$$\beta = \frac{\sqrt{3}}{2}\frac{\hbar^2}{m_o}\left[\left(k_x^2 - k_y^2\right)\gamma_2 - 2ik_xk_y\gamma_3\right] \tag{2.8d}$$

$$D = L - H \tag{2.8e}$$

$$S = \frac{1}{2}(L + H) - \Delta_0 \tag{2.8f}$$

and, γ_1, γ_2 and γ_3 are the Luttinger parameters of the host semiconductor and Δ_0 is the spin orbit splitting energy of the host semiconductor. Diagonalization of the matrix yields the dispersion relations for the E_- and and E_+ bands for each of the original valence bands. Again, V can be simplified to $C_{MN}x^{1/2}$ as for the conduction band. $C_{MN}x^{1/2}$ is the empirically determined coupling parameter. Figure 2.6 shows the VBAC fitting for the bandgap change of GaN_xAs_{1-x} with $C_{MAs} = 1.60eV$ and $E_{As} = 0.62eV$. The fit shows a good agreement with the experimental data and provides a physical explanation for the discontinuous bandgap change in GaN_xAs_{1-x} [51].

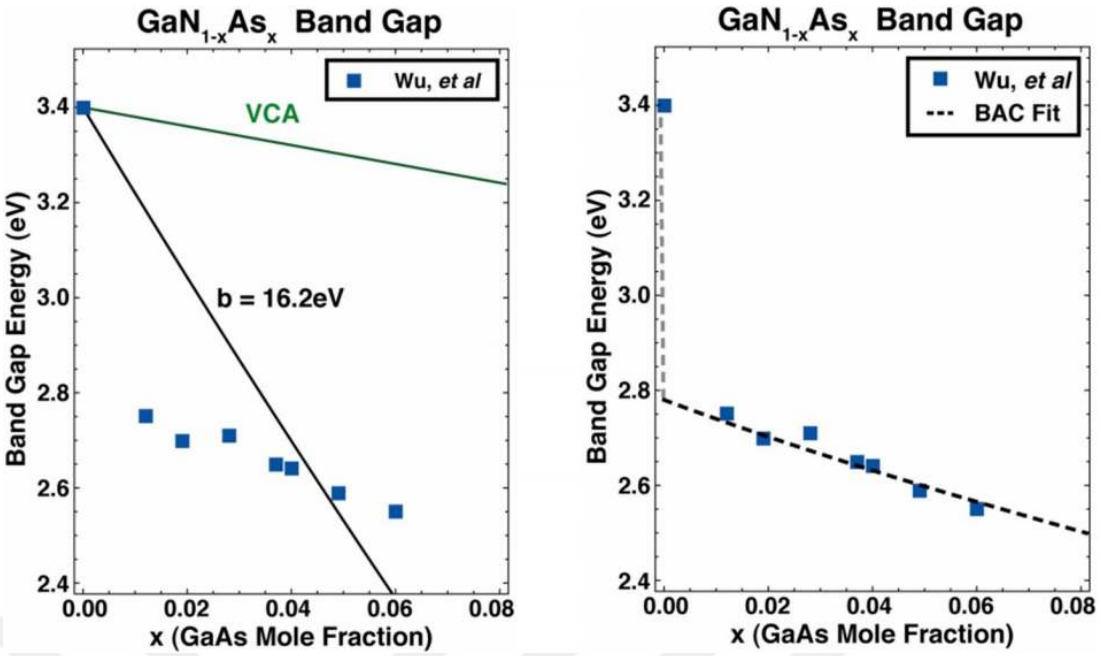

Figure 2.8: Measured bandgap of GaN_xAs_{1-x} as a function of x and its comparison with a) VCA [14] and b) VBAC model [51].

2.5 Summary

In this chapter, we reviewed different theoretical models and provided the calculation methods for III-N-V material systems used throughout this thesis. We also introduced some brief definitions which are necessary to understand topology of the structures.

CHAPTER 3

AN ANALYSIS OF BAND STRUCTURE AND CRITICAL THICKNESS OF Ga(NAsP) QWS ON Si SUBSTRATES

3.1 Introduction

The never ending quest to find easy to manufacture, efficient and cost effective optoelectronic devices that would satisfy the need to be high performance devices operating in the optical telecommunication wavelength range of 1.3 μm is brought us to GaP based III-N-V material systems. GaP based $GaAs_{1-y}P_y$ alloys have found applications in optoelectronic devices for a long time, and as a result the physical properties of theses alloys such as atomic structure, energy band structure, and effective mass have been studied in great detail. However, lack of suitable substrate leading $GaAs_{1-y}P_y$ alloys to be grown on GaP substrates has its shortcomings(deficiencies) such as lattice mismatch [60], matching refractive index, and poor band structure configuration [61] which yield in decreased layer thickness, poor carrier and optical confinement, and electron effective mass [62] much lighter than that of holes. With the incorporation of nitrogen (N) into $GaAs_{1-y}P_y$ alloy, these physical properties have been changed significantly and these major challenges are overcame. Arsenide (As) rich dilute nitride Ga(NAsP) exhibits a type I direct band gap material lattice matched to GaP and hence Si [63, 64] substrates.

The chapter is organized as follows; The optimum concentrations of the material systems which yields a direct band gap required for laser applications is presented in Section 3.2. The modelling of effective masses of $GaN_xAs_{1-x-y}P_y$ and its comparison with that of the host matrix $GaAs_{1-y}P_y$ is also studied in Section 3.2. The concentration dependence of band structure and band alignment is given in Section 3.3. Finally, the phenomena of critical thickness is investigated and the results are given in Section 3.4. The theoretical models that have been used throughout the calculations have been provided in each related section.

3.2 Electronic Band Structure of Ga(NAsP) Alloy on Si Substrates

3.2.1 Conduction Band Edge Energy Levels

We use the simple band anti-crossing model (BAC) [9, 65] in order to exploit the concentration range for which one might expect a direct energy gap for $GaN_xAs_{1-x-y}P_y$. The BAC model which yields reasonably good results with experiments can be used as a predictive tool to describe the dilute-nitride-phosphide materials in spite of the multiplicity of nitrogen levels [66, 67]. The model explains composition dependencies of the III-N-V semiconductors by conduction band (CB) splitting which is due to N-induced perturbation and N concentration enhances this splitting effect

The splitting is caused by N-induced perturbation and is enhanced with increasing N concentration. The new conduction bands are denoted as E_- and E_+, and the energy difference between them increases with N concentration. The model allows us to calculate the fundamental band gap, E_-, of $GaN_xAs_{1-x-y}P_y$/GaP laser structures through the eigenvalue of

$$\begin{vmatrix} E - E_M & -V_{MN} \\ -V_{MN} & E - E_N \end{vmatrix} = 0 \tag{3.1}$$

where E_M and E_N are the energies of extended state and localized N-level relative to the top of valence band (VB), respectively. V_{MN} is the matrix element describing the coupling between N and conduction band states and taken as

$$V_{MN} = C_{MN}\sqrt{x} \tag{3.2}$$

where x is the N concentration. C_{MN} is the coupling parameter determined by the strength between localized and extended states and taken as 1.9 [66]. The solution to this eigenvalue problem gives us the dispersion relation of

$$E_\pm = \left(E_N + E_M \pm \sqrt{(E_N - E_M)^2 + 4V_{MN}^2} \right) \Big/ 2 \tag{3.3}$$

The nitrogen level position E_N was determined by interpolation of isolated N level in ternary composition end points of GaAs:N (E_N=1.67 eV) and GaP:N (E_N=2.18 eV) [26]. The nitrogen dependence of the conduction band energy E_M of the matrix semiconductor is taken as E_M= E_0 - 3.5x [26] where E_0 is the bulk band gap energy in the absence of nitrogen. For band structure of quaternary alloy $GaN_xAs_{1-x-y}P_y$/GaP, the material parameters, except for band energies, are linearly interpolated from those of the binary materials using the following

relation of

$$\begin{aligned} T_{GaNAs} &= uB_{GaN} + (1-u)B_{GaAs} + u(1-u)C_{GaNAs} \\ T_{GaAsP} &= \upsilon B_{GaAs} + (1-\upsilon)B_{GaP} + \upsilon(1-\upsilon)C_{GaAsP} \\ T_{GaNP} &= \omega B_{GaN} + (1-\omega)B_{GaP} + \omega(1-\omega)C_{GaNP} \end{aligned} \tag{3.4}$$

where $u = (1-x-y)/2$, $\upsilon = (2-x-2y)/2$ and $\omega = (2-2x-y)/2$. C is bowing parameter for ternary alloys. Finally, by using the following expression we calculate bulk band gap energy E_0 of ternary alloys taking bowing parameters into account

$$Q_{GaN_xAs_yP_{1-x-y}}(x,y) = \frac{xyT_{GaNAs}(u)+y(1-x-y)T_{GaAsP}(\upsilon)+x(1-x-y)T_{GaNP}(\omega)}{xy+y(1-x-y)+x(1-x-y)} \tag{3.5}$$

The material parameters used in our calculations are tabulated in Table 3.1.

Material	**GaAs**	**GaN**	**GaP**	**AlP**
Lattice Constant a_0 (Å)	5.6532	4.5	5.4504	5.467
Energy gap E_o (eV)	1.424	3.299	2.777	3.56
Spin-orbit Splitting Δ_0 (eV)	0.341	0.017	0.08	0.07
Effective mass ($m^*_{e,\Gamma}$)	0.067	0.15	0.13	0.22
Effective mass ($m^*_{e,SO}$)	0.172	0.29	0.25	0.30
Hydrostatic deformation potential for CB a_c (eV)	-7.17	-2.2	-8.2	-5.7
Hydrostatic deformation potential for VB a_v (eV)	-1.16	-5.2	-1.7	-3.0
Luttinger parameter γ_1	6.98	2.67	4.05	3.35
Luttinger parameter γ_2	2.06	0.75	0.49	0.71
Luttinger parameter γ_3	2.93	1.10	2.93	1.23
Elastic Stiffness Constant C_{11} (GPa)	1221.0	293.0	1405.0	1330.0
Elastic Stiffness Constant C_{12} (GPa)	566.0	159.0	620.3	630.0
Elastic Stiffness Constant C_{44} (GPa)	600.0	155.0	703.3	615.0
Deformation Potential b (eV)	-2.0	-2.2	-1.6	-1.5
Average Valence Band Energy ($E_{v,av}$)	-6.92	×	-7.40	-8.09
1^{st} order pressure derivative α (10^{-2} eV/GPa) [69, 70, 71]	10.8	40	9.7	11.1
2^{nd} order pressure derivative β (10^{-4} eV/GPa) [69, 70, 71]	-14.0	-0.38	-35.0	×
Interband Matrix Element E_P^2 (eV)	22.66	25.0	20.0	17.7
Refractive Index(λ_g) [2]	3.6	2.6	3.4	3.0

Table 3.1: Binary material parameters used in our calculations. The parameters are taken from Vurgaftman *et al* [68].

Figure 3.1 presents the calculated variations of the Γ-, X-, and L- conduction band edge minimums, E_M's, for host $GaAs_{1-y}P_y$ as a function of phosphide concentration. Material parameters used for these calculations are presented in

Table 3.1. It is clear from Figure 3.1 that the position of the band edge minimums strongly depend on the phosphide alloy composition and $GaAs_{1-y}P_y$ has an indirect band gap when phosphide concentration is above 45%. So we prefer As-rich $GaAs_{1-y}P_y$ ternary material in order to maintain in the direct band gap region.

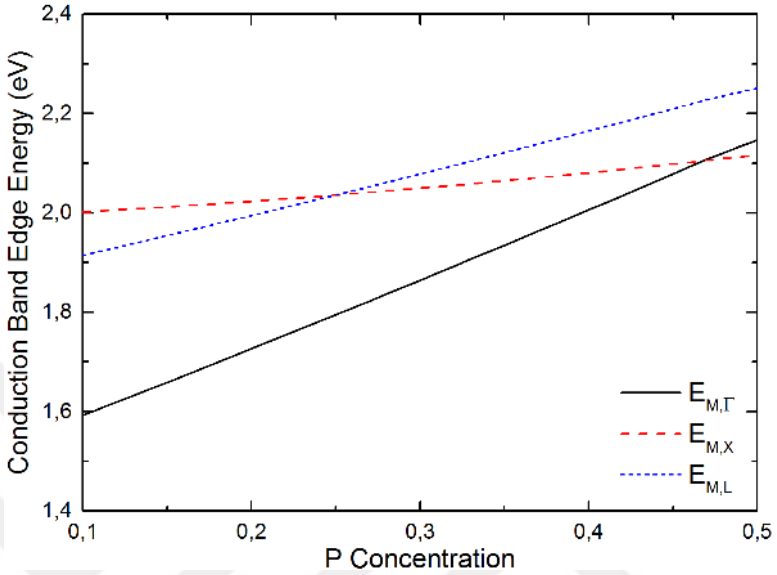

Figure 3.1: The calculated phosphide concentration dependence of Γ-, X- , and L- conduction band edge minimums of $GaAs_{1-y}P_y$ by using Vegard's Law.

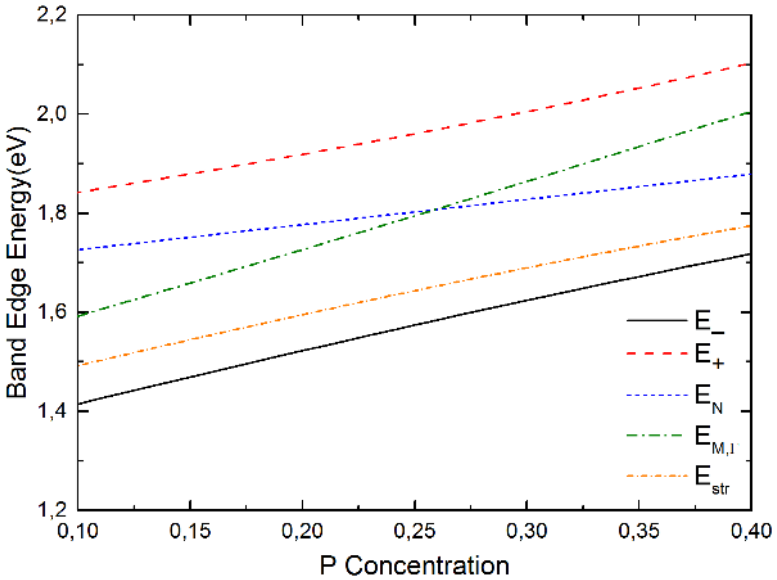

Figure 3.2: The calculated phosphide concentration dependence of Γ-, X- , and L- conduction band edge minimums and strained bandgap of host matrix GaAsP energy E_M, and bulk E_-, E_+ and E_{str} of quaternary $GaN_{0.01}As_{0.99-y}P_y$ using band anti-crossing model.

To determine the concentration range for which one might expect a direct energy gap for dilute nitride phosphide $GaN_xAs_{1-x-y}P_y$ alloy, the BAC is used to calculate the energies of E_- and E_+ as a function of phosphide concentration. The results of these calculations are presented in Figure 3.2. As is seen from the calculated results, the incorporation of nitrogen into $GaAs_{1-y}P_y$ causes a strong reduction in the band gap energy of dilute nitride phosphide $GaN_xAs_{1-x-y}P_y$ alloy. This is due to the strong interaction of the conduction band minima with the close-lying N energy level. The nitrogen incorporation into $GaAs_{1-y}P_y$ also allows the required adjustment of the lattice constant to that of the GaP. The nitrogen energy level E_N increases with increasing phosphide concentration due to the end points values of E_N=1.67 eV for GaAs:N and E_N=2.18 eV for GaP:N as seen in Figure 3.2. The variation of strained band gap E_{str} of $GaN_xAs_{1-x-y}P_y$ as a function of phosphide concentration for varying nitrogen concentrations of 1% - 4% is presented in Figure 3.3. The E_{str} of dilute-nitride-phosphide $GaN_xAs_{1-x-y}P_y$ alloy decreases with increasing nitrogen concentration.

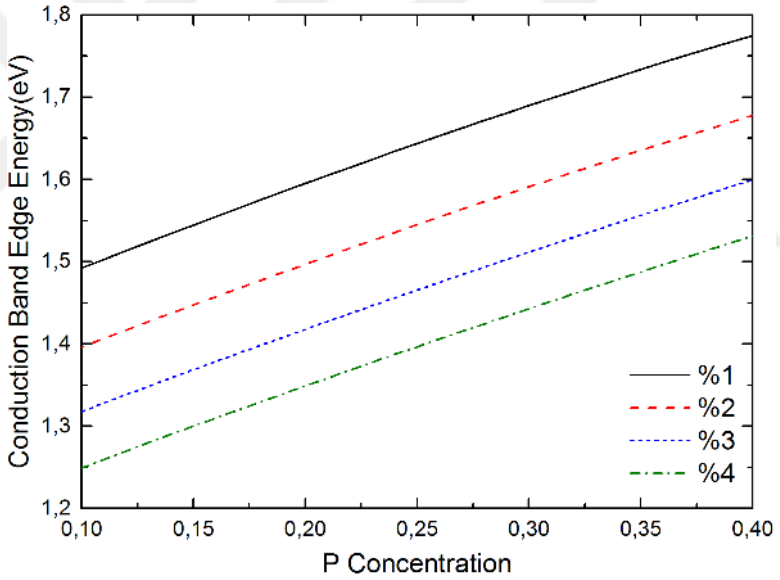

Figure 3.3: The nitrogen and phosphide concentration dependence of E_{str} of quaternary $GaN_xAs_{1-x-y}P_y$.

Figure 3.4 compares the magnitude of compressive strain in $GaAs_{1-y}P_y$ with that of the $GaN_xAs_{1-x-y}P_y$ alloy. As can be seen from calculations that strain is very large in $GaAs_{1-y}P_y$ and it decreases with increasing phosphide concentration. Figure 3.4 also shows clearly how the incorporation of nitrogen into $GaAs_{1-y}P_y$ effectively reduces the compressive strain. This rapid reduction in the magnitude of compressive strain with an increase in nitrogen- and phosphide concentration in $GaN_xAs_{1-x-y}P_y$ well material is a great advantage for a uniform growth. In

order to reveal the effect of nitrogen incorporation on the band structure of host $GaAs_{1-y}P_y$ we have changed the nitrogen concentration between 1%-4%.

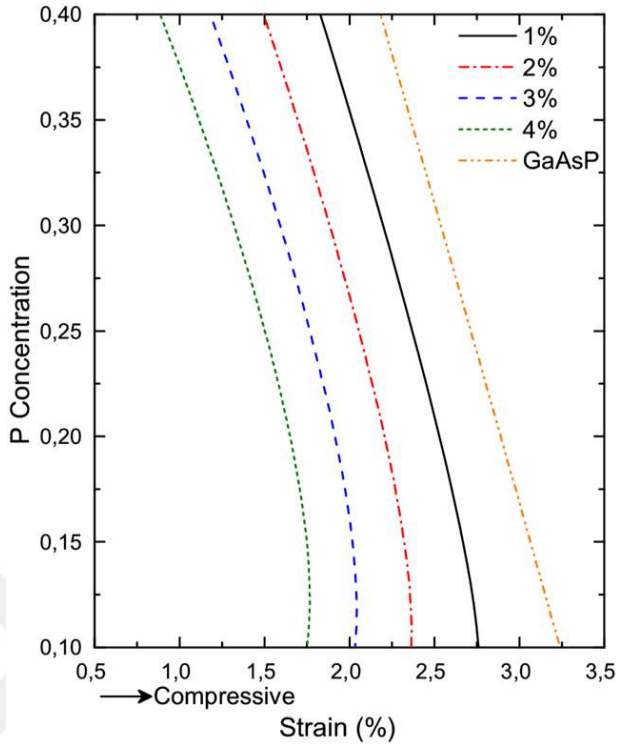

Figure 3.4: The calculated phosphide concentration dependence of compressive strain for ternary $GaAs_{1-y}P_y$ and quaternary $GaN_xAs_{1-x-y}P_y$ for varying nitrogen concentrations of 1% - 4%.

It can be concluded from these variations that $GaN_xAs_{1-x-y}P_y$ alloy is more advantageous compared to that of the $GaAs_{1-y}P_y$. The advantageous of the quaternary $GaN_xAs_{1-x-y}P_y$ in comparison to ternary $GaAs_{1-y}P_y$ lie in its quaternary nature which provides more degree of freedom to engineer more suitable E_- energy band resulting a narrow band gap in quaternary alloy compared to that of ternary alloy's. The splitting between E_+ and E_- energy bands increase with increasing nitrogen- and phosphide-concentration. Therefore, the predicted larger separation between E_+ and E_- energy bands possibly enhances the operation of the proposed laser systems since E_- energy band is extended from the nitrogen energy level E_N with increasing nitrogen- and phosphide-concentration. All these variations of E_N, E_- and E_{str} in terms of phosphide and nitrogen concentrations obtained in Figure 3.2 and 3.3 will play an important role for the determination of effective mass that will be provided in chapter Section 3.2.2.

3.2.2 Effective Mass of GaAsP and Ga(NAsP)

The strain is a new degree of freedom available to optimize the semiconductor laser characteristics: the structural modifications with respect to a bulk, relaxed semiconductor, added to the size quantization effects, lead to drastic changes of the electronic properties. Figure 3.5 shows that in a compressively strained structure, at k=0 the split between heavy- and light-hole bands splits apart increases resulting decreased heavy hole mass. This decrease in the heavy hole mass yields reduced density of states (DOS) for holes. This leads to reduced threshold current density in the laser structure. Moreover, as the light-hole states which do not participate in the lasing transition are pushed further back due to strain, rate of non-radiative transitions from the light-hole band to other subband also decreases . These states are thus less populated, which leads to an increase of the semiconductor laser efficiency. One can also demonstrate that the differential gain is higher in a strained structure than in a lattice matched one.

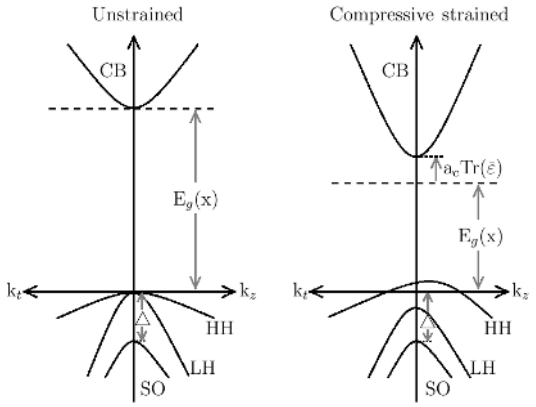

Figure 3.5: Schematic diagram showing the bulk band structure of $GaN_xAs_{1-x-y}P_y$ strained layers grown on GaP substrate.

Using Eqn. 3.3 , the effective mass is derived as [72]

$$\frac{1}{m^*} = \frac{1}{\hbar^2 k}\left|\frac{\partial E_-(k)}{\partial k}\right|_{k=0} = \frac{1}{2m_M}\left[1 - \frac{E_M(0) - E_N}{\sqrt{(E_M(0) - E_N)^2 - 4V_{MN}^2}}\right] \tag{3.6}$$

where m_M is the electron effective mass in the host crystal. Eqn. 3.6 can be simplified to the form

$$m^* = m_M\left(1 + \frac{V_{MN}^2}{(E_N - E_-)^2}\right) \tag{3.7}$$

The electron effective mass of GaN_xAs_{1-x} calculated with Eqn. 3.7 is shown in Figure 3.6. According to calculated data, effective mass increases rapidly for

low N concentrations and then saturates. Saturation occurs due to coupling of NN states and conduction band states does not benefit from coupling between N dopants.

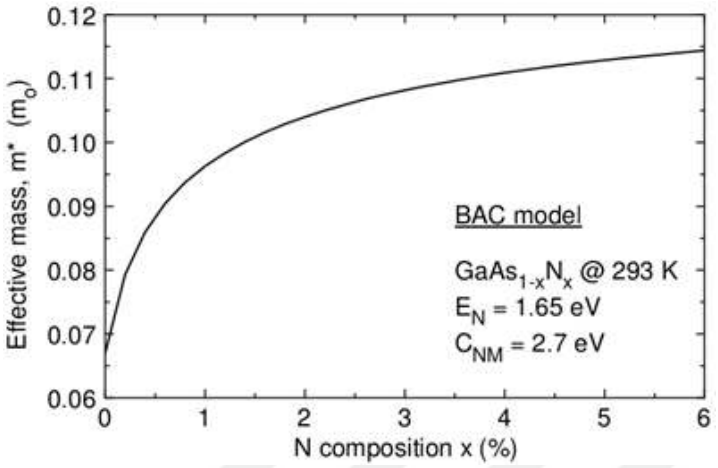

Figure 3.6: Electron effective mass in GaN_xAs_{1-x} calculated by Zhang et al. [73] with band anti-crossing model.

With the introduction of N into GaAs, effective mass of conduction band increases for GaN_xAs_{1-x} material system [74]. Effective mass values of $0.12m_0$ and $0.19m_0$ are reported for GaN_xAs_{1-x} material system containing 1.2% and 2.0% N compositions, respectively [75]. Their report suggests that the effective mass will continuously increase with increasing N composition x. This increasing trend in the electron effective mass as a function of the N doping has obtained further support recently [76].

We now intend to illustrate how the incorporation of N into $GaAs_{1-y}P_y$ will have a positive effect on the effective masses. Results of these calculations for the ternary $GaAs_{1-y}P_y$ and the proposed novel material system $GaN_xAs_{1-x-y}P_y$ as a function of nitrogen- and phosphide-concentration are presented in Figure 3.7. These variations point out that incorporation of nitrogen into GaAsP increases the effective mass of electron m_c in 1.4 orders of magnitude. Figure 3.7 also indicates how an increase in phosphide concentration in $GaN_xAs_{1-x-y}P_y$ will provide a close matching between m_c and m_v. The valence band effective mass m_v increases slightly whereas the conduction band effective mass m_c increases quickly with increasing phosphide concentration for $GaN_xAs_{1-x-y}P_y$.

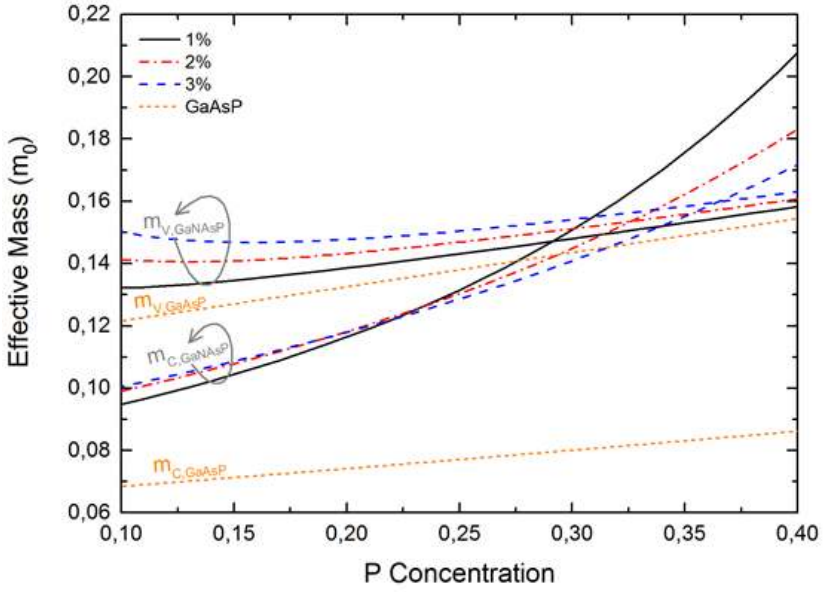

Figure 3.7: Carrier effective mass of $GaAs_{1-y}P_y$ and $GaN_xAs_{1-x-y}P_y$.

These variations enable the effective masses of m_c and m_v being equivalent or even m_c being greater than m_v. So by means of changing N and P concentrations it is possible to change the effective masses to a significant extent. The calculated substantial increase in m_c and the close matching between m_c and m_v of $GaN_xAs_{1-x-y}P_y$ are beneficial for device designing because of its effect on subband carrier populations. In addition, it is illustrated in Figure 3.7 that m_c of $GaN_xAs_{1-x-y}P_y$ increases slightly with increasing nitrogen concentration for low phosphide values whereas it decreases with increasing nitrogen concentration for higher phosphide values. This is due to the fact that our proposed material system of $GaN_xAs_{1-x-y}P_y$ includes three group VA element of N, As and P. This opposite behaviour can be understood by means of close investigation of Figure 3.2 which shows that the energy levels E_N and E_- varies at different rates with increasing phosphide concentration. On the other hand the energy difference (E_N - E_-) increases with increasing nitrogen concentration causing a decrease in effective mass of electron in $GaN_xAs_{1-x-y}P_y$y (see Eqn. 3.7). In spite of all these, the effective mass of electron in $GaN_xAs_{1-x-y}P_y$ is significantly greater than that of the host matrix $GaAs_{1-y}P_y$ and may improve the efficiency of laser devices. Figure 3.7 also indicates that both incorporation of N into host matrix $GaAs_{1-y}P_y$ and an increase in phosphide concentration removes the strong asymmetry in the effective masses of conduction- and valence-bands. This uncommon large effective mass of electron improves the matching between CB and VB density of states. This is due to the fact that ratio of m_c / m_v gets better in $GaN_xAs_{1-x-y}P_y$ than that of $GaAs_{1-y}P_y$.

3.3 Band Alignment of Ga(NAsP) alloy on Si Substrates with GaP and AlGaP Barriers

3.3.1 Model Solid Theory

For a well designed optoelectronic material, the structure and form of its band alignment is an important factor. The band alignment is defined by band discontinuity between the quantum well and barrier and the distribution of this discontinuity over the relative bands. The distributed discontinuity of conduction and valance bands are represented as ΔE_c and ΔE_v, respectively. Physical properties of the constituent semiconductor alloys characterizes how the band discontinuity generated. It has been commonly accepted that the nitrogen incorporation mainly affects the conduction band states of the Ga(NAsP) alloys leading to an increase in the conduction band offset Q_c, and a small discontinuity in the valence band edge [64]. According to Van de Walle's model solid theory [77] the band offset ratio for conduction and valence band, $Q_{c,v}$, is determined by discontinuity fractions of $\Delta E_c/\Delta E_g$. The energy of the potential barrier, ΔE_g, is determined from the difference between the bulk bandgap energy of the barrier layers and the strained bandgap energy of the active layer. The conduction band position can be calculated by simply adding the strained bandgap energy to the valence band position. The unstrained valence band-edge of the active region material is set as the reference energy of zero. The valence band position is given by

$$E_v(x,y) = \begin{cases} E_{v,av}(x,y) + \frac{\Delta_0(x,y)}{3} + \delta E_{hh}(x,y) \text{ for hh (compressive strain)} \\ E_{v,av}(x,y) + \frac{\Delta_0(x,y)}{3} + \delta E_{lh}(x,y) \text{ for lh (tensile strain)} \end{cases} \tag{3.8}$$

where $E_{v,av}(x,y)$ is the average valence subband energy and Δ_0 is the spin-orbit split-off band energy. These values are listed in Table 3.1. The conduction band is shifted by the energy $\delta E_c(x,y)$:

$$\delta E_c(x,y) = 2a_c \left(1 - \frac{C_{12}}{C_{11}}\right) \varepsilon. \tag{3.9}$$

The valence bands are shifted by the energy $\delta E_{hh}(x,y)$ and$\delta E_{lh}(x,y)$

$$\begin{aligned} \delta E_{hh}(x,y) &= -P_\varepsilon - Q_\varepsilon \\ \delta E_{lh}(x,y) &= -P_\varepsilon + Q_\varepsilon, \end{aligned} \tag{3.10}$$

where

$$\begin{aligned} P_\varepsilon &= -2a_v \left(1 - \tfrac{C_{12}}{C_{11}}\right) \varepsilon \\ Q_\varepsilon &= -b \left(1 + \tfrac{2C_{12}}{C_{11}}\right) \varepsilon, \end{aligned} \tag{3.11}$$

and where a_c and a_v are the conduction- and valence-band hydrostatic deformation potentials, b is the valence band shear deformation potential and C_{11} and C_{12} are elastic stiffness constants. The strained band gaps can be expressed as

$$\begin{aligned} E_{c-hh}(x,y) &= E_g(x,y) + \delta E_c(x,y) - E_{hh}(x,y) \\ E_{c-lh}(x,y) &= E_g(x,y) + \delta E_c(x,y) - E_{lh}(x,y). \end{aligned} \tag{3.12}$$

The conduction band position is

$$E_c(x,y) = \begin{cases} E_v(x,y) + E_{c-hh}(x,y) \text{ for hh (compressive strain)} \\ E_v(x,y) + E_{c-lh}(x,y) \text{ for lh (tensile strain)} \end{cases} \tag{3.13}$$

$$\frac{\Delta Ec}{\Delta Eg} = 1 - \frac{E_v^w - E_v^b}{E_g^b - E_g^w}, \tag{3.14}$$

where E_v^w and E_v^b are the valence band positions in the well and barrier materials, respectively, and E_g^w and E_g^b are the strain adjusted band gaps (E_{c-hh}, for the compressive strain and E_{c-lh}, for the tensile strain) for the well and barrier materials.

3.3.2 Band Alignment of Strained Ga(NAsP)/GaP QW on Si Substrates

We now extend our analysis to estimate the band alignment in these newly proposed As rich $GaN_xAs_yP_{1-x-y}$/GaP on Si substrates using Model Solid Theory. Figure 3.8(a) presents the calculated band offset ratios of Q_c and Q_v for compressively strained As-rich $GaN_xAs_{0.8}P_{0.2-x}$type I quantum well with GaP barriers on Si substrates. Upper and lower curves represent the variation of the conduction band offset ratio Q_c and the valence band offset ratio Q_v with increasing nitrogen concentration in well, respectively. These calculations show that the incorporation of N into $GaAs_{1-y}P_y$ increases the conduction band offset ratio Q_c and decreases the valence band offset ratio Q_v gradually. The corresponding band offset energies for conduction band ΔE_c and valence band ΔE_v are shown in Figure 3.8(b). It can be seen from Figure 3.8(b) that larger conduction band offset energies can be achieved with an increase in nitrogen concentration of $GaN_xAs_{0.8}P_{0.2-x}$. Larger conduction band offset energies, in turn, cause an improved confinement in well and a decreased spill out of electrons. It can be concluded from Figure 3.8 that the incorporation of nitrogen into $GaAs_{1-y}P_y$ mainly affects the conduction band offset energy and there are only minor changes in the valence band offset energy. Hence, we illustrate that the incorporation of nitrogen into $GaAs_{1-y}P_y$ leads the N-containing system having a band alignment of that of the ideal case (deep conduction- and shallow valence-wells).

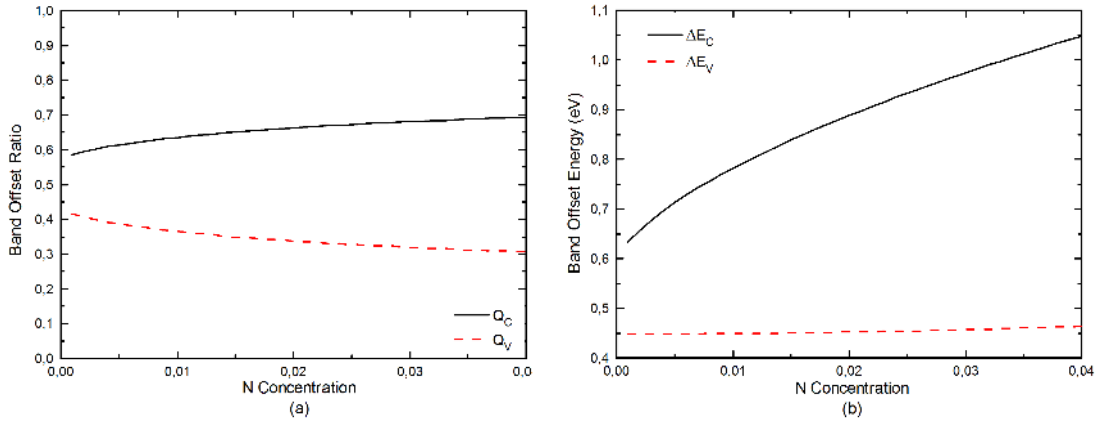

Figure 3.8: The variation of the (a) band offset ratio of Q_c and Q_v and (b) band offset energies of ΔE_c and ΔE_v in $GaN_xAs_{0.8}P_{0.2-x}$/GaP QW structure on GaP substrate as a function of nitrogen concentration [64].

Figure 3.9(a) presents the calculated band offset ratios of Q_c and Q_v for compressively strained $GaAs_{1-y}P_y$ and As-rich $GaN_xAs_{1-x-y}P_y$ type I quantum well with GaP barriers on Si substrates. A closer investigation of Figure 3.9 shows clearly that the incorporation of N into $GaAs_{1-y}P_y$ improves the band alignment substantially. The valence band offset ratio Q_v is greater than the conduction band offset ratio Q_c for $GaAs_{1-y}P_y$ causing the band offset energy of valence band ΔE_c being greater than that of the conduction band offset energy ΔE_c. This is an undesired band alignment structure which may cause an electron spill out to the barriers. By incorporating N into $GaAs_{1-y}P_y$, band alignment is improved substantially.

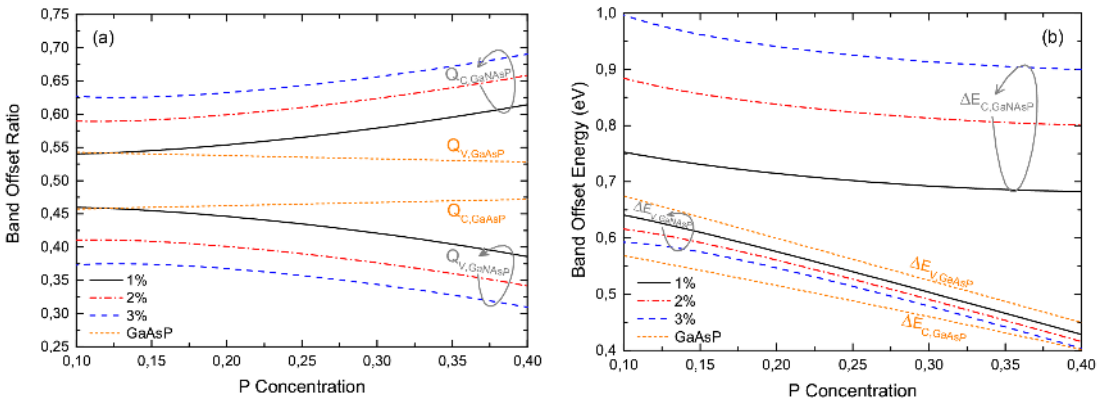

Figure 3.9: Variation of (a) band offset ratio of Q_c and Q_v and (b) band offset energies of ΔE_c and ΔE_v in $GaN_xAs_{1-x-y}P_y$/GaP QW structure on Si substrate as a function of phosphide and nitrogen concentration.

The calculations presented in Figure 3.9 show distinctly the improvement in band alignment due to incorporation of N into host matrix $GaAs_{1-y}P_y$. The conduction band offset ratio Q_c is now greater than the valence band offset ratio Q_v and the incorporation of N into $GaAs_{1-y}P_y$ increases Q_c and decreases Q_v gradually. The increase in phosphide concentration has a similar effect to that of the nitrogen. Corresponding band offset energies for conduction band ΔE_c and valence band ΔE_v shown in Figure 3.9(b) shows the significant development of the band alignment of $GaN_xAs_{1-x-y}P_y$ compared to that of the host matrix $GaAs_{1-y}P_y$. It can also be seen from Figure 3.9(b) that larger conduction band offset energies can be achieved with a higher nitrogen- and a lower phosphide-concentration in $GaN_xAs_{1-x-y}P_y$. Larger conduction band offset energies, in turn, cause an improved electron confinement in well and a decreased electron spill out. As is seen in Figure 3.9 the incorporation of nitrogen into $GaAs_{1-y}P_y$ mainly affects conduction band offset energy and there are only minor changes in valence band offset energy. As an overall, an ideal band alignment of deep conduction- and shallow valence-wells can be achieved in $GaN_xAs_{1-x-y}P_y$/GaP structure with a lower phosphide concentration.

3.3.3 Band Alignment of Ga(NAsP)/AlGaP/GaP QW on Si Substrates

We aim to reveal whether the optimization of the quaternary $GaN_xAs_y P_{1-x-y}$ well material on GaP substrates can be achieved by means of using $Al_zGa_{1-z}P$ barriers. Figure 3.10(a) presents the effect of aluminium concentration in barrier on the calculated band offset ratios of Q_c and Q_v for compressively strained type I $GaN_xAs_{0.8}P_{0.2-x}/Al_zGa_{1-z}P$ QW structure on GaP substrate for different N concentrations. It is seen from Figure 3.10(a) that valence band offset ratio Q_v increases and conduction band offset ratio Q_c decreases with increasing Al concentration. However it is clear from Figure 3.10(b) that combined effect of N concentration in well and Al concentration in barrier improves the both band offset energies of conduction band ΔE_c and valence band ΔE_v. Thus, replacing GaP barriers with that of $Al_zGa_{1-z}P$ barriers causes a further increase at the depth of the conduction- and valence-wells leading better carrier confinement in both conduction- and valence-bands.

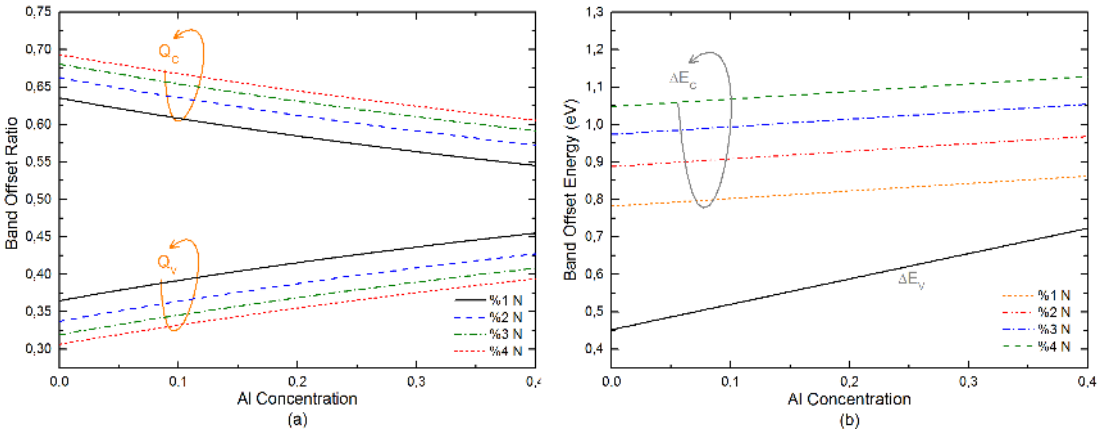

Figure 3.10: Effect of N concentration (in well) and Al concentration (in barrier) on (a) band offset ratio of Q_c and Q_v and (b) band offset energies of ΔE_C and ΔE_V in $GaN_xAs_{0.8}P_{0.2-x}/Al_zGa_{1-z}P$ on GaP substrates [64].

3.4 The Phenomena of Critical Thickness

Essentially all high performance semiconductor devices are based on crystalline materials. There are some devices that use low cost amorphous or polycrystalline semiconductors, but their performance is quite poor. Crystals are made up of identical building blocks, the block being an atom or a group of atoms. While in "natural" crystals the crystalline symmetry is fixed by nature, new advances in crystal growth techniques are allowing scientists to produce artificial crystals with modified crystalline structure. In an epitaxial process, the epilayer that is grown on the substrate could have a lattice constant that may differ from that of the substrate. Such epitaxy is called strained epitaxy and is one of the important emerging areas of crystal growth studies. The motivation for strained epitaxy is twofold:

(1) Incorporation of built-in strain: When a lattice mismatched semiconductor is grown on a substrate and the thickness of the epilayer is very thin, the epilayer has a built-in strain. This built-in strain has important effects on the electronic and optoelectronic properties of the material and can be exploited for high performance devices.

(2) Generation of a new effective substrate: It has been noted that in semiconductor technology, high quality substrates are only available for Si, GaAs and InP (sapphire and quartz substrates are also available and used for some applications). Most semiconductors are not lattice-matched to

these substrates. So how can one grow these semiconductors epitaxially? One solution that has emerged is to grow the epilayer on a mismatched substrate. If the conditions are right, a lot of dislocations as illustrated in Figure 3.11 are generated and eventually the epilayer forms its own substrate. This process allows a tremendous flexibility in semiconductor technology. Not only can it, in principle, resolve the substrate availability problem, it also allows the possibility of growing GaAs on Si, CdTe on GaAs, etc. Thus different semiconductor technologies can be integrated on the same wafer.

Consider a case where an epilayer with lattice constant a_e is grown on a substrate with lattice constant a_s. This situation is shown schematically in Figire 3.12. The strain between the two materials is defined as

$$\varepsilon = \frac{a_s - a_e}{a_e} \tag{3.15}$$

Consider a conceptual exercise one where we deposit a monolayer of the epilayer on the substrate. If the lattice constant of the epilayer is maintained to be a_e, it is easy to see that after every 1/bonds between the epilayer and the substrate, either a bond is missing or an extra bond appears as shown in Figure 3.12(b). In fact, there would be a row of missing or extra bonds since we have a 2-dimensional plane. These defects are the dislocations. The presence of these dislocations costs energy to the system since a number of atoms do not have proper chemical bonding at the interface.

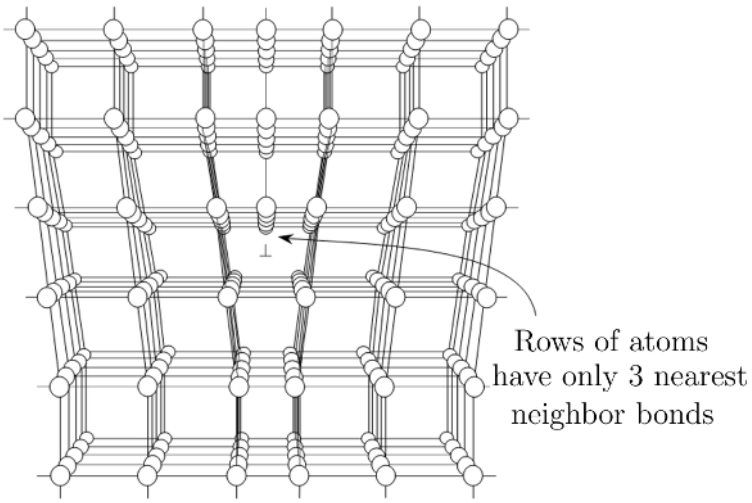

Figure 3.11: A schematic showing the presence of a dislocation. This line defect is produced by adding an extra half plane of atoms. At the edge of the extra plane, the atoms have a missing bond [78].

For small lattice mismatch (<0.1), the epilayer initially grows in perfect registry with the substrate, as shown in Figure 3.12(c). However, as noted before, the strain energy will grow as the epilayer thickness increases. As a result, it will eventually be favorable for the epilayer to generate dislocations. In simplistic theories this occurs at an epilayer thickness called the critical thickness, h_c, which is approximately given by

$$h_c = \frac{a_S}{2\,|\varepsilon|} \tag{3.16}$$

In reality, the point in growth where dislocations are generated is not so clear cut and depends upon growth conditions, surface conditions, dislocation kinetics, etc. However, one may use the criteria given by Eqn. 3.16 for loosely characterizing two regions of epilayer thickness for a given lattice mismatch. Below critical thickness, the epilayer grows without dislocations and the film is under strain. Under ideal conditions above critical thickness, the film has a dislocation array, and after the dislocation arrays are generated, the epilayer grows without strain with its free lattice constant.

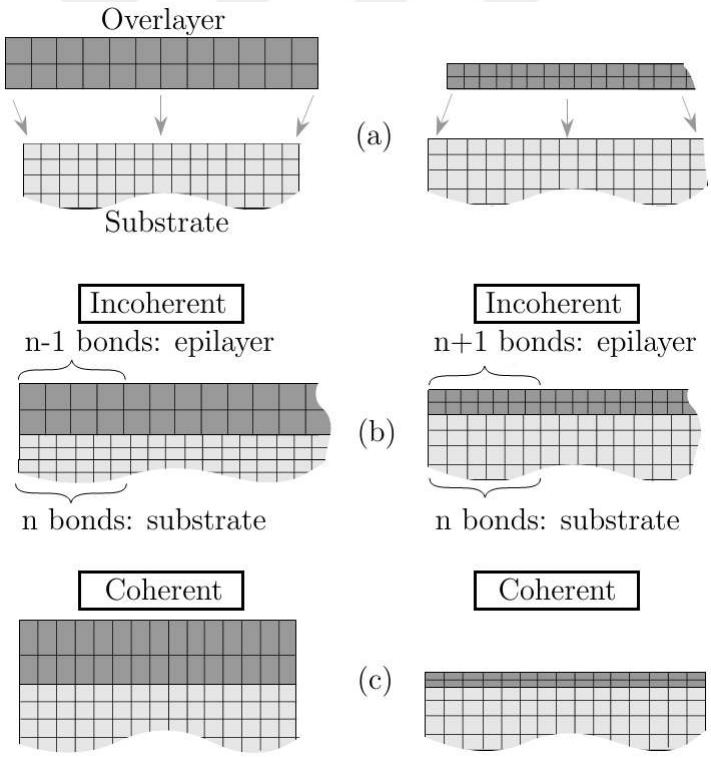

Figure 3.12: (a) The conceptual exercise in which an epilayer with one lattice constant is placed without distortion on a substrate with a different lattice constant. (b) Dislocations are generated at positions where the interface bonding is lost. (c) The case is shown where the epilayer is distorted so that no dislocation is generated [78].

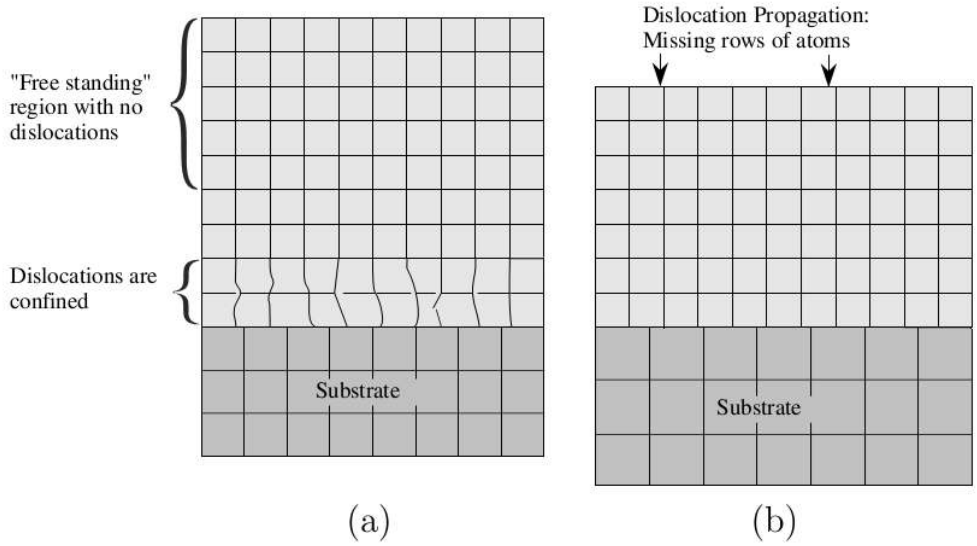

Figure 3.13: Strained epitaxy above critical thickness. (a) A structure whose dislocations are confined in the interface of epilayer and substrate. This is a desirable mode of epitaxy. (b) The dislocations are penetrating the epilayer, rendering it useless for most optoelectronic applications [78].

While strained epitaxy below critical thickness is an extremely powerful tool for tailoring the optoelectronic properties of semiconductors, epitaxy beyond the critical thickness is important to provide new effective substrates for new material growth. For these applications the key issues center on ensuring that the dislocations generated stay near the overlayer-substrate interface and do not propagate into the overlayer as shown in Figure 3.13.

For layer-by-layer growth, the epitaxial semiconductor layer is biaxially strained in the plane of the substrate, by an amount $\varepsilon_{\parallel}$, and uniaxially strained in the perpendicular direction, by an amount $\varepsilon_{\perp}$. For a thick substrate, the in-plane strain of the layer is determined from the bulk lattice constants of the substrate material, a_s, and the layer material, a_e:

$$\varepsilon_{\parallel} = \frac{a_S}{a_E} - 1 \tag{3.17}$$

Since the layer is subjected to no stress in the perpendicular direction, the perpendicular strain, $\varepsilon_{\perp}$, is simply proportional to $\varepsilon_{\parallel}$:

$$\varepsilon_{\perp} = \frac{-\varepsilon_{\parallel}}{\sigma} \tag{3.18}$$

where the constant σ is known as Poisson's ratio.

For each of these cases, a critical thickness h_c, below which the misfit strain is accommodated without formation of misfit dislocations, can be defined in terms of the elastic constants of the materials. Matthews and Blakeslee [79] introduced the model for the calculation of critical thickness for layers having equal elastic constants in a superlattice

$$h_c = \frac{a_o}{\kappa\sqrt{2}\pi\varepsilon}\frac{1-0.25\sigma^{(001)}}{1+\sigma^{(001)}}\ln\left(\frac{h_c\sqrt{2}}{a_o}+1\right) \tag{3.19}$$

where h_c is the critical thickness, and a_o is the lattice constant of the strained layer, $\sigma^{(001)}$ is the Poisson ratio, κ is a coefficient having a value of 1 for a strained layer superlattice, 2 for a single quantum well and 4 for a single layer strained layer. For (001) and (111) directions Poisson ratio calculated by the following equations:

$$\sigma^{(001)} = \frac{C_{12}}{C_{11}+C_{12}} \tag{3.20}$$

$$\sigma^{(111)} = \frac{C_{11}+2C_{12}-2C_{44}}{2\left(C_{11}+2C_{12}+C_{44}\right)} \tag{3.21}$$

where the necessary constants are listed in Table 3.2.

Material	**GaAs**	**GaN**	**GaBi**
Lattice Constant a_0 (Å)	5.6532	4.5	6.324
Energy gap E_o (eV)	1.424	3.299	-1.45
Spin-orbit Splitting Δ_0 (eV)	0.341	0.017	2.2
Hydrostatic deformation potential for CB a_c (eV)	-7.17	-2.2	-7.17
Hydrostatic deformation potential for VB a_v (eV)	-1.16	-5.2	-1.16
Elastic Stiffness Constant C_{11} (GPa)	1221.0	293.0	81.6
Elastic Stiffness Constant C_{12} (GPa)	566.0	159.0	28.1
Elastic Stiffness Constant C_{44} (GPa)	600.0	155.0	59.7
Deformation Potential b (eV)	-2.0	-2.2	×
Poisson Ratio $\sigma^{(001)}$	0.3167	0.3517	0.2561
Poisson Ratio $\sigma^{(111)}$	0.1952	0.1964	0.0465

Table 3.2: Binary material parameters used in our calculations. The parameters are taken from Vurgaftman *et al* [80].

3.4.1 Calculation of Critical Thickness for GaAsP and Ga(NAsP) on Si Substrates

Critical thickness of $GaAs_{1-y}P_y$ and $GaN_xAs_{1-x-y}P_y$ are simulated for a single quantum well layer on (001) GaP substrate. The results are presented in Figure 3.14.

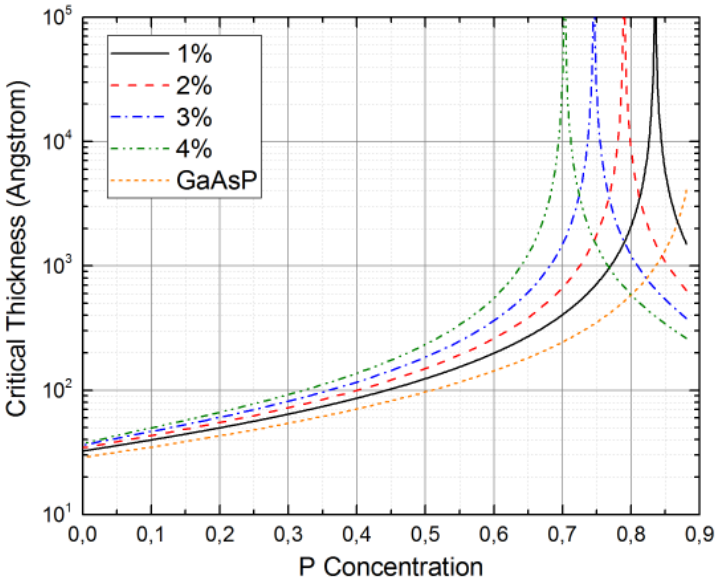

Figure 3.14: Phosphide concentration dependence of critical thickness.

The lattice mismatch between epilayer and substrate decreases with increasing N concentration and this reduces the amount of compressive strain, therefore uniform growth can be expected with lesser defects being generated. For higher P concentration, critical thickness values reach a peak value for each N concentration for $GaN_xAs_{1-x-y}P_y$. These peak values represent the material composition of $GaN_xAs_{1-x-y}P_y$ to be lattice match on (001) GaP substrates.

3.5 Summary

In this chapter, we have presented an analysis of electronic band structure of quaternary system $GaN_xAs_{1-x-y}P_y$ and GaAsP by employing conduction band anti-crossing model and model solid theory.

By varying the N and P concentration in the well material $GaN_xAs_{1-x-y}P_y$, we demonstrated that the bandgap of dilute nitride arsenide phosphide decreases rapidly with an increase in nitrogen and arsenide concentrations. We also shown that $GaN_xAs_{1-x-y}P_y$ is lattice matched to GaP/Si, removing possible strain induced growth effects on the epilayer as well as critical thickness being disregarded. As an overall, the presented theoretical analysis to investigate and optimize the band structure of $GaN_xAs_{1-x-y}P_y$/GaP QW on Si proved to be worthy.

Using model solid theory on $GaN_xAs_{1-x-y}P_y$/GaP material system, band offset energy and ratio is calculated. As results indicate with increasing N incor-

poration percentage band offset of $GaN_xAs_{1-x-y}P_y$/GaP improves significantly. Also incorporation of Al into barrier slightly increases the conduction band offset energy. However band offset ratio decreases with increased Al concentration in the barrier material $Al_zGa_{1-z}P$.

Lastly, effective mass of $GaN_xAs_{1-x-y}P_y$ is analysed and compared to that of $GaAs_{1-y}P_y$. N incorporation improves band offset as well as the mass ratio, conduction band effective mass over valence band effective mass.

CHAPTER 4

AN ANALYSIS OF BAND STRUCTURE AND CRITICAL THICKNESS OF Ga(NAsBi) QWS ON GaAs SUBSTRATES

4.1 Introduction

Bismide (Bi) III-Bi-V alloys has attracted much attention due to its interesting band structure. Alloying III-V compounds with small amounts of nitrogen leads to dramatic reduction of fundamental bandgap energy in the resulting dilute nitride alloys. This effect originates from an anti-crossing interaction between extended conduction band states and N defect states. In case of Bi, the interaction occurs between valence band states and localized Bi states. This can be achieved by replacing small amount of group V element by Bi. Major advantage of this newly proposed novel laser material system is the fact that Auger recombination loss mechanism being eliminated. To achieve that, incorporation of high concentrations of N and Bi is necessary. However with these concentration levels, defects and dislocations is a major concern. Therefore it is necessary to investigate the material composition dependent parameters such as bandgap, strain and critical thickness for this laser material system.

We present a theoretical investigation to optimize the concentration levels of N and Bi for $GaN_xAs_{1-x-y}Bi_y$/GaAs. Our theoretical calculations indicate that incorporation of N and Bi into GaAs host material yield bandgap energies corresponding to 1.33 and 1.55 μm. Investigation of strain and critical thickness for this material system is also a necessity. To ensure high quality growth of the material system, various concentrations of N and Bi are used in the calculations. Furthermore, with a well found ratio y/x of 1.7, $GaN_xAs_{1-x-y}Bi_y$ is a lattice match to GaAs, which potentially enables high quality III-V epitaxial films on GaAs substrates. The ability to substantially change the band gap energy while maintaining lattice matching to common substrates makes Ga(NAsBi) a promising material for a wide range of near infrared optoelectronics applications, includ-

ing light-emitters and detectors in the long-wavelength region, high-performance optoelectronic devices, and efficient solar cells.

4.2 Electronic Band Structure of Ga(NAsBi) Alloy on GaAs Substrates

We have used band anti-crossing model to describe the effects of N incorporation into III-V semiconductor alloys and we have presented its effects on $GaN_xAs_{1-x-y}P_y$ alloy in Chapter 3 in details. However, modelling of electronic band structure of Ga(NAsBi) differs from Ga(NAsP) due to effects of Bi incorporation are observed on both conduction- and valance band edge. In this section we will cover the effects of Bi incorporation starting with its influence on valance band edge energy levels.

4.2.1 Valence Band Edge Energy Levels

Alberi et al proposed that same principles that conduction band anti-crossing model (explained in Section 3.2.1) use can be adopted to explain large band gap reduction in $GaAs_{1-y}Bi_y$, as the atomic radii of As and Bi are highly mismatched too [81]. This extended model is called the valence band anti-crossing (VBAC) model.

Bi incorporation into GaAs produces Bi defect states that interact with the extended states of the host (GaAs). Since Bi has a lower electronegativity than As, the defect level is in close proximity to the valence band energy levels of GaAs. The interaction between these states results in a splitting of the valence band into two sub-bands, called E_+ and E_- bands. The former is located at a higher energy than the Bi level while the latter is located at a lower energy. Based on the VBAC model, the energies of the E_+ and E_- levels are given by

$$E_{\pm}(GaAsBi) = \frac{E_{V,GaAs} + E_{Bi} \pm \sqrt{(E_{V,GaAs} - E_{Bi})^2 + 4V_{MBi}^2}}{2} \tag{4.1}$$

where $E_{V,GaAs}$ is the energy of valence band maximum (VBM) of GaAs, $E_{Bi} = 0.4\ eV$ is the energy of the Bi level and below the VBM of GaAs [81], $C_{Bi} = 1.6\ eV$ is the coupling parameter between the Bi level and GaAs VBM. The values of E_+, E_- and E_{Bi} are referenced to the VBM of GaAs, which is in turn referenced to zero. Assuming a parabolic band for GaAs,

$$E_V(GaAs) = -\frac{\hbar^2 k^2}{2m^*} \tag{4.2}$$

where $\hbar$ is the Planck constant, k is the momentum and m^* is the hole's effective mass. Figure 4.1 shows the calculated energy dispersion of the valence band of $GaAs_{0.98}Bi_{0.02}$. The anti-crossing interaction between the VBM of GaAs and Bi level causes the valence band maximum of $GaAs_{1-y}Bi_y$ to increase, consequently reducing the band gap.

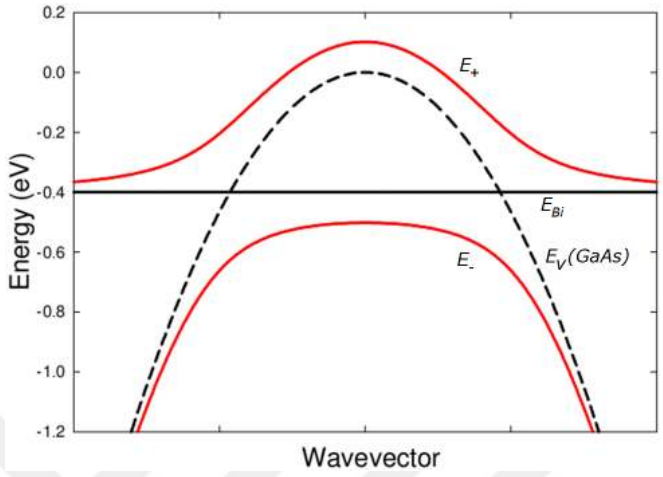

Figure 4.1: The calculated valence band structure of $GaAs_{0.98}Bi_{0.02}$ using the VBAC model. Solid black and dashed lines refer to the Bi level and the valence band edge of GaAs, respectively [82].

If the conduction band is assumed to be unaffected, since the Bi level is located at much lower energy than the conduction band, the band gap of $GaAs_{1-y}Bi_y$ is given by,

$$E_{g,GaAsBi} = E_{C,GaAs} - E_{+,GaAsBi} \tag{4.3}$$

which can be simplified to

$$E_{g,GaAsBi} = E_{g,GaAs} - \Delta E_{VBAC} \tag{4.4}$$

where ΔE_{VBAC} refers to the band gap reduction due to Bi incorporation. The valence band of $GaAs_{1-y}Bi_y$ is described by,

$$E_{\pm}(GaAsBi) = \frac{E_{V,GaAs} + E_{Bi} \pm \sqrt{(E_{V,GaAs} - E_{Bi})^2 + 4V_{MBi}^2}}{2} \tag{4.5}$$

Assuming that the conduction band is constant, the band gap of $GaAs_{1-y}Bi_y$ is

$$E_{g,GaAsBi} = E_{C,GaAs} - E_{+,GaAsBi} \tag{4.6}$$

where E_C is the conduction band minimum of GaAs. Since,

$$E_{Bi} = E_{V,GaAs} - \Delta E_{VBM-Bi} \tag{4.7}$$

and

$$E_{g,GaAs} = E_{C,GaAs} - E_{V,GaAs} \tag{4.8}$$

where ΔE_{VBM-Bi} is the energy difference between the VBM of GaAs and the Bi level. Using Eqn. 4.5 to 4.8, the band gap of $GaAs_{1-y}Bi_y$ can be simplified to

$$E_{g,GaAsBi} = E_{g,GaAs} - \Delta E_{VBAC} \tag{4.9}$$

Here, ΔE_{VBAC} refers to the band gap reduction due to bismuth incorporation, which is given by,

$$\Delta E_{VBAC} = \frac{\Delta E_{VBM-Bi}}{2}\left(\sqrt{1 + \frac{4V_{MBi}^2}{\left(\Delta E_{VBM-Bi}\right)^2}} - 1\right) \tag{4.10}$$

The VBAC model was then modified to include the reduction of the conduction band minima. The values calculated using the modified VBAC model are in agreement with the experimental data for the whole Bi concentration range, as shown in Figure 4.2. The data fitting was obtained with $C_{Bi} = 1.55\,eV$. The fitting also shows that the Bi concentration needed to achieve 1.33 and 1.55 μm emission in bulk material is 0.072 and 0.102, respectively. For quantum well structures, higher Bi concentration is required to achieve similar wavelength emission due to quantum effects.

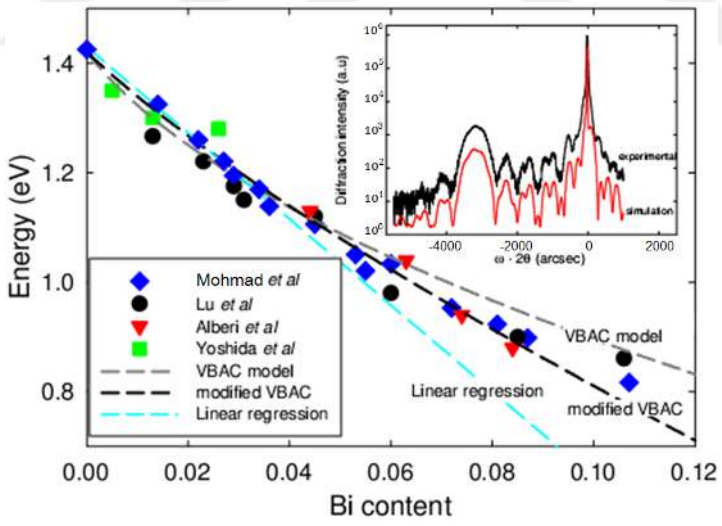

Figure 4.2: Bi concentration dependence of $GaAs_{1-y}Bi_y$ samples grown by Mohmad *et al* [82]. The grey and black dashed lines correspondes to the bandgaps which are estimated by VBAC and modified VBAC models, respectively. The inset shows the HR-XRD spectra of $GaAs_{0.892}Bi_{0.108}$.

Recently, Usman et al reported a tight-binding analysis to investigate the electronic structure of $GaAs_{1-y}Bi_y$ [83]. This method is an atomistic approach

which allows for quantitative investigation of the effect of isolated impurity atoms (in this case replacing an As atom with a Bi atom) on the electronic structure of the host material [83, 84]. Usman et al reported the evolution of Bi resonant states in ordered $GaAs_{1-y}Bi_y$ supercells (4096 atoms) which contained a single Bi atom, a single Bi pair and a small Bi clusters [83]. Similar calculations were then extended to calculate the electronic properties of randomly disordered $GaAs_{1-y}Bi_y$ supercells (4096 atoms) in which the number of Bi pairs and n-atom clusters increased by y^2 and y^n [83]. The results confirm that the evolution of the valence band edge of $GaAs_{1-y}Bi_y$ can be described by the VBAC model. However, the VBAC model only partially explains the band gap reduction of $GaAs_{1-y}Bi_y$.

Usman et al found that the conduction band minima also reduces linearly with Bi incorporation at a rate of 28 meV/%Bi [83]. The conduction band of $GaAs_{1-y}Bi_y$ ($y \leq 0.05$) retains the Γ character of the GaAs conduction band for $y \geq 97$ % [83]. The dominant GaAs character and linear energy reduction suggest that the evolution of the conduction band with Bi concentration can be best described by the conventional alloy model [83]. As the evolution of the valence band maxima becomes less pronounced at high Bi concentrations, the contribution from the conduction band becomes increasingly significant. For example, the conduction band offset and the valence band offset of the 0.8 eV band gap $GaAs_{1-y}Bi_y$ are $280meV$ and 340 meV, respectively. This could explain the divergence between experimental data and theoretical values predicted by the VBAC model at high Bi concentrations.

The lattice constant of the $GaN_xAs_{1-x-y}Bi_y$ structure is determined by the linear relation:

$$a(x, y) = x \cdot a_{GaN} + y \cdot a_{GaBi} + (1 - x - y) \cdot a_{GaAs} \tag{4.11}$$

The nitrogen concentration required to maintain a lattice match to GaAs substrate for different bismuth concentration is given by the relation [85, 86]:

$$y \cong 1.7x \tag{4.12}$$

a_{GaBi} is assumed to be 6.324 Å [87], and all the other parameters of binaries are taken from Vurgaftman et al.[80]. It has been proposed that the incorporation of Bi might improve the electronic properties of GaN_xAs_{1-x} by strain compensating the small N atom with the larger Bi atom [85, 88].

In the light of these information, we have carried out calculations for GaAs based ternary GaN_xAs_{1-x} on GaAs substrates by using conduction band anticrossing model (see Section 3.2.1) to investigate the effects of N incorporation

in GaAs. Since GaNAs is not lattice-matched to GaAs, build-up strain energy will result a reduction in bandgap of GaN_xAs_{1-x}. The reduction in bandgap of GaN_xAs_{1-x} on GaAs substrates due to these effects is shown in Figure 4.3. There is an energy difference between E_- and E_{str} and this difference gets wider with N concentration. This is due to increased number of N atoms in the formation of lattice structure of GaAs host matrix which build-up more and more strain energy then the lattice structure could handle.

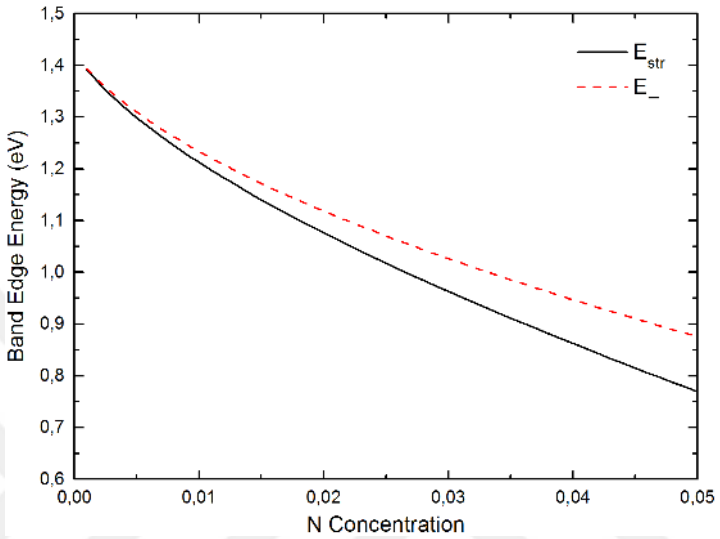

Figure 4.3: Band anti-crossing effect (dash line) of N and the corresponding strained bandgap (solid line) in GaN_xAs_{1-x} on GaAs substrate.

As discussed earlier, effect of Bi incorporation into GaAs host material is not limited on valence band edge but it also affects the conduction band edge energy levels too. Presence of large Bi atoms in the lattice structure of $GaAs_{1-y}Bi_y$ generates strain on GaAs substrates. Therefore bandgap energy is reduced rapidly under these effects. To identify how each effect influences bandgap of $GaAs_{1-y}Bi_y$, we have calculated these effects separately and present them in Figure 4.4. Rapid decrease in the bandgap of $GaAs_{1-y}Bi_y$ is due to ΔE_{VB} which is upward energy shift in VB_{min} (dash-dot line), and ΔE_{CB} which is downward energy shift in CB_{min} (dash line) occurring simultaneously. Effect of strain on bandgap reduction ΔE_{Str} (dot line) is also presented. Summation of ΔE_{VB}, ΔE_{CB} and ΔE_{Str} gives us the total decrease in the bandgap of $GaAs_{1-y}Bi_y$. Continuous line represents strained bangap of $GaAs_{1-y}Bi_y$ as well as the corresponding strain percentage in the well.

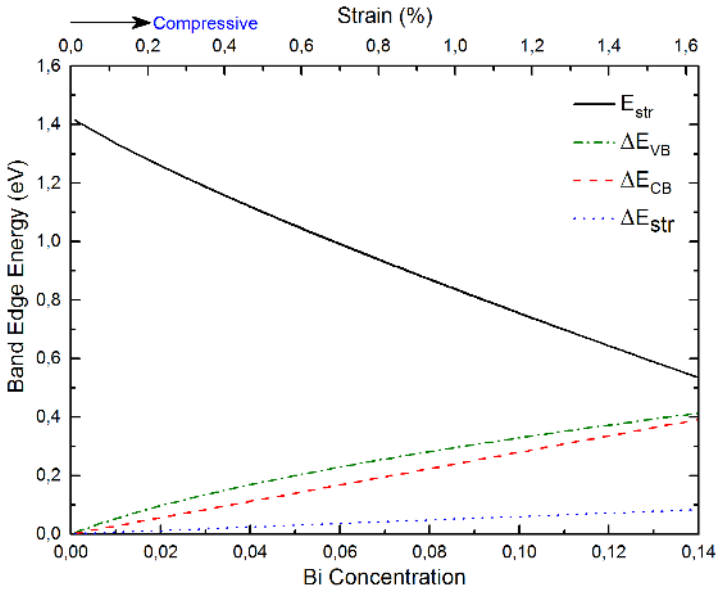

Figure 4.4: Estimated variation of bandgap in $GaAs_{1-y}Bi_y$ and shift in energy (ΔE_{CB}, ΔE_{VB}, ΔE_{str}) due to Bi incorporation and strain.

In the case of GaN_xAs_{1-x} the strain is tensile while for $GaAs_{1-y}Bi_y$ the strain is compressive. So with the aforementioned ratio of $y \cong 1.7x$ in Eqn. (4.12) the $GaN_xAs_{1-x-y}Bi_y$ quaternary alloy can be grown on GaAs substrates without strain in between layers. The ratio can be obtained from the data that is presented in Figure 4.5.

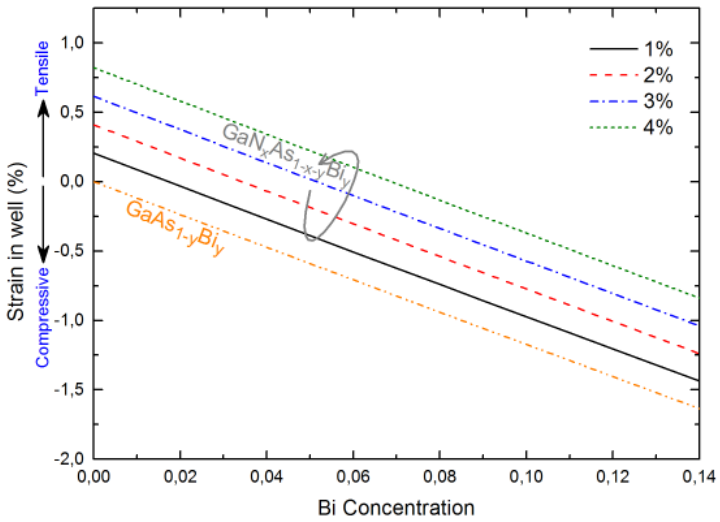

Figure 4.5: Estimated variation of strain due to Bi incorporation in $GaAs_{1-y}Bi_y$ and $GaN_xAs_{1-x-y}Bi_y$. N content is varied from zero to four percent for comparison.

Estimated bandgap of $GaN_xAs_{1-x-y}Bi_y$ is calculated by employing the following equation:

$$E_{g,GaNAsBi} = E_{g,GaNAs} - \Delta E_{VBAC,GaAsBi} - \Delta E_{CB_{\min},GaNAsBi} \tag{4.13}$$

$E_{g,GaNAs}$ is calculated by conduction band anti-crossing model. Derivation of $\Delta E_{VBAC,GaAsBi}$ is shown previously. $\Delta E_{CB_{\min},GaNAsBi}$ is assumed 28 meV/% Bi [83]. To compare the effect of N concentration in $GaN_xAs_{1-x-y}Bi_y$, various concentrations of N are included in Fig. 4.6.

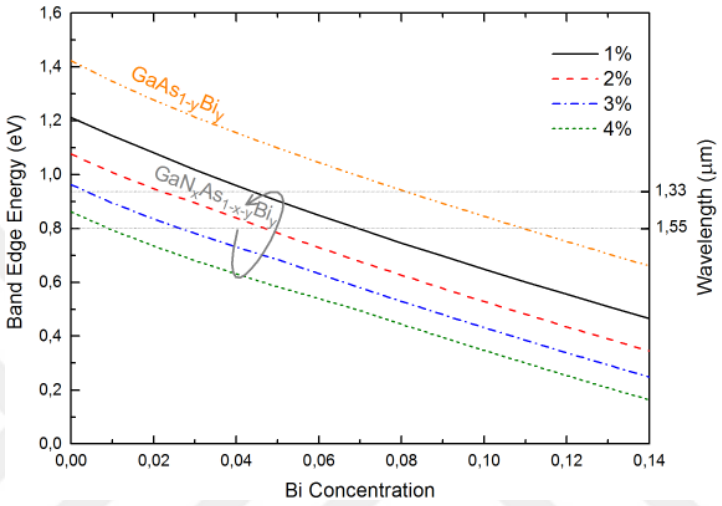

Figure 4.6: Estimated variation of bandgap due to Bi and N incorporation in $GaN_xAs_{1-x-y}Bi_y$. N content is varied from zero percent to five percent for comparison.

Reduction of bandgap energy can be seen in Figure 4.6. Effects of N incorporation on the GaAsBi conduction band minima has a diminishing strength. This may be explained by closeness of conduction- and valence bands to each other which affects the N states that lies below the conduction band, and there the coupling strength in between them. Small changes in bandgap energy can be observed in Figure 4.6 due to Bi concentration variation. Effects of Bi incorporation in the $GaAs_{1-y}Bi_y$ is shown in Figure 4.4 and we have shown that not only valence band gets effected but also conduction band minima. Now with the N doping into $GaAs_{1-y}Bi_y$, energy corresponding to conduction band minima pushed back further into the range of long wave-length region. This broad energy spectrum can easily be obtained by incorporating even small concentration of N and Bi into Ga(NAsBi) and as an optoelectronic device that can be used in a wide variety of applications.

4.2.2 Calculation of Critical Thickness for GaNAs and GaNAsP on GaAs Substrates

Strained expitaxy that does not exceed critical thickness is a useful method of engineering the properties of optoelectronic semiconductor material systems. For these applications the key issues focus around ensuring that the dislocations generated stay near the epilayer-substrate interface and do not propagate into the epilayer. The phenomena of critical thickness is explained and discussed in details for GaNAs and Ga(NAsP) on GaP substrates in Section 3.4. With those in mind, we investigate the material systems of GaNAs, GaAsBi and Ga(NAsBi) on GaAs substrates.

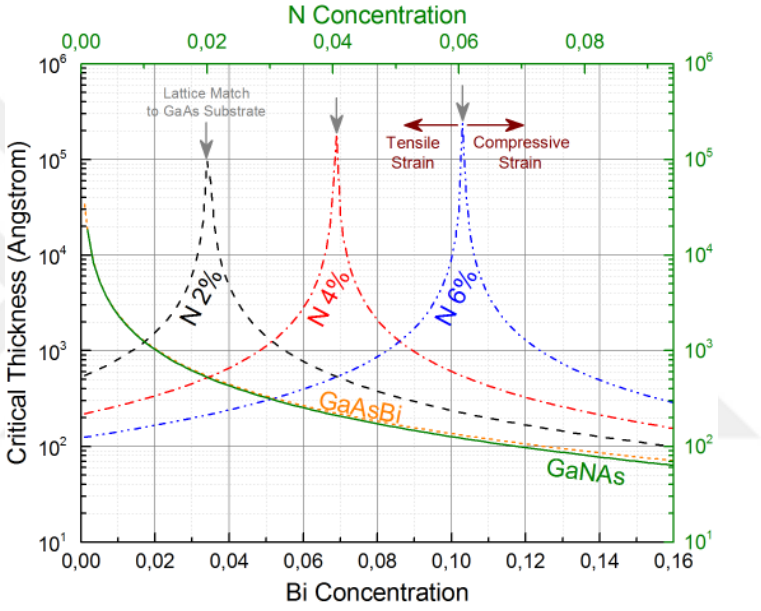

Figure 4.7: Concentration dependece of critical thickness of GaN_xAs_{1-x}, Ga $As_{1-y}Bi_y$ and $GaN_xAs_{1-x-y}Bi_y$ on GaAs substrate (001) for a single quantum well layer.

For the ternary GaN_xAs_{1-x} and $GaAs_{1-y}Bi_y$ on GaAs substrates, critical thickness decreases due to lattice mismatch on GaAs substratse getting large with increased N and Bi concentration. However, in the case of $GaN_xAs_{1-x-y}Bi_y$ presence of both N and Bi atoms compensate the strain generated by one another. This compensative effect is shown in Figure 4.7 for 2%, 4% and 6% N concentration of $GaN_xAs_{1-x-y}Bi_y$/GaAs material system. For each N concentration critical thickness for $GaN_xAs_{1-x-y}Bi_y$ reaches to a peak value and each peak represent Bi to N concentration ratio of 1.7 as well as required material composition of $GaN_xAs_{1-x-y}Bi_y$ for it to be lattice match on GaAs substrates. This compen-

sative property of N to Bi (or vice versa) of Ga(NAsBi) is an advantage over most III-V material system. Up to now, common III-V semiconductors alloys could not constitute high N concentration due to strain generated from N atoms in the structure could not be managed by, and therefore high N concentration were avoided in order not to create undesirable dislocations. By incorporating Bi and N with a reasonable ratio, dislocations can be avoided and epilayer of desired thickness of $GaN_xAs_{1-x-y}Bi_y$ QW can be grown on GaAs substrates.

4.3 Summary

In this chapter, we have presented an analysis of electronic band structure of quaternary system $GaN_xAs_{1-x-y}Bi_y$ on GaAs substrates by employing conduction and valence band anti-crossing model.

We have presented the results of VBAC calculations on newly proposed dilute nitride bismide $GaN_xAs_{1-x-y}Bi_y$/GaAs material system. These results indicate that by varying the N and Bi concentration in the well material, the bandgap of dilute nitride bismide decreases rapidly. This creates a broad range of bandgap energy corresponding to long wavelength region and possible new optoelectronic applications. We have investigated the role of Bi and N on the critical thickness of $GaN_xAs_{1-x-y}Bi_y$ QWs on GaAs substrate for (001) orientations. The yielding results indicate that the N concentration has strain compensating effect on Bi related strain or vice versa. We also shown that $GaN_xAs_{1-x-y}Bi_y$ is lattice matched to GaAs for Bi to N ratio being 1.7, removing possible strain induced growth effects on the epilayer as well as critical thickness being disregarded.

CHAPTER 5

A THEORETICAL INVESTIGATION OF OPTICAL MODE CONFINEMENT IN Ga(NAsP) QWS ON Si SUBSTRATES

5.1 Introduction

Primary and important factor of designing a semiconductor quantum well laser is the confinement of both carrier and optical mode. Confinement of carriers ultimately determined by the band offset design of the heterostructures. Optical mode is related with the refractive index difference between the core of wave guide and that of its the cladding layer. It is known that the refractive index strongly depends on the direct band gap of the semiconductor materials and the band gap of the III-N-V semiconductor material system can be engineered by means of adding nitrogen into the host semiconductor GaAsP. In this chapter, we investigate the refractive indices of the heterostructures and corresponding optical confinement factors of the proposed III-N-V laser material systems GaNAsP with AlGaP cladding layer on Si substrates.

5.2 Theory

5.2.1 Adachi's Model for Refractive Index

A more physics-based model of dielectric function for photon energies close to and above the band gap is Adachi's model. This model can be simplified for the transparency region $\hbar\omega < E_g$ by considering only the first band gaps (E_g; $E_g + \Delta_0$)

$$n_r^2(\omega) = Af(x_1) + 0.5\left(\frac{E_g}{E_g + \Delta_0}\right)^{1.5} f(x_2) + B \tag{5.1}$$

where A and B are the empirical parameters which are given in Table 5.1.

$$f(x_1) = \frac{1}{x_1^2}\left(2 - \sqrt{1 + x_1} - \sqrt{1 - x_1}\right) \tag{5.2}$$

where $x_1 = \frac{\hbar\omega}{E_g}$ and

$$f(x_2) = \frac{1}{x_2^2}\left(2 - \sqrt{1+x_2} - \sqrt{1-x_2}\right) \tag{5.3}$$

where $x_2 = \frac{\hbar\omega}{E_g+\Delta_0}$. A and B parameters of quaternary compound semiconductors are calculated by interpolation method [89].

5.2.2 Five-layer Symmetric Slab Theory

The obtained laser light should also be confined in heterostructure as electron. For this aim different type waveguides have been produced. One of these waveguides is five-layer slab waveguide so we made our calculations according this type waveguide. The structure of this waveguide is shown in Figure 5.1.

Parameter	A	B	E_g (eV)	Δ_0 (eV)
GaAs	6.3	9.4	1.424	0.341
GaP	22.25	0.9	2.777	0.08
AlP	24.1	-2.0	3.56	0.07
GaN	9.31	3.03	3.299	0.017

Table 5.1: The required parameters related to the refractive index of the materials [68, 89].

(1) Electric field distribution for core region (well region):

$$\xi_{y1}(x,z,t) = A\cos(h_1 x)\, e^{i(\omega t-\beta z)}; 0 \le |x| \le a \tag{5.4}$$

(2) Electric field distribution for barrier region :

$$\xi_{y2}(x,z,t) = B\cos(h_2 x)\, e^{i(\omega t-\beta z)}; a \le |x| \le b \tag{5.5}$$

(3) Electric field distribution for cladding layer region :

$$\xi_{y3}(x,z,t) = Ce^{-h_3 x}e^{i(\omega t-\beta z)} \quad ; b \le |x| \le c \tag{5.6}$$

The field distributions for even-order modes are written:

$$kn_2 \ge \beta \ge kn_3 \tag{5.7}$$

For now, we don't consider exponential complex part; If we apply the boundary conditions to electric fields, we can see that; At $x = a$; $\xi_{y1}(\mathrm{a}) = \xi_{y2}(\mathrm{a})$ and so $Acos(h_1 a) = Bcos(h_2 a)$

$$B = \frac{A\cos(h_1 a)}{cos(h_2 a)} \Rightarrow E_{y2}(x) = \frac{A\cos(h_1 a)}{cos(h_2 a)}\cos(h_2 x) \tag{5.8}$$

At $x = b$; $\xi_{y2}(b) = \xi_{y3}(b)$ and so

$$\frac{A\cos(h_1 a)}{cos(h_2 a)}\cos(h_2 b) = Ce^{-h_3 b} \tag{5.9}$$

$$C = \frac{A\cos(h_1 a)e^{h_3 b}}{cos(h_2 a)}\cos(h_2 b) \Rightarrow E_{y3}(x) = \frac{A\cos(h_1 a)}{cos(h_2 a)}\cos(h_2 b)e^{h_3(b-x)} \tag{5.10}$$

At $x = a$; $\frac{\partial \xi_{y1}(x)}{\partial x} = \frac{\partial \xi_{y2}(x)}{\partial x}$ and so

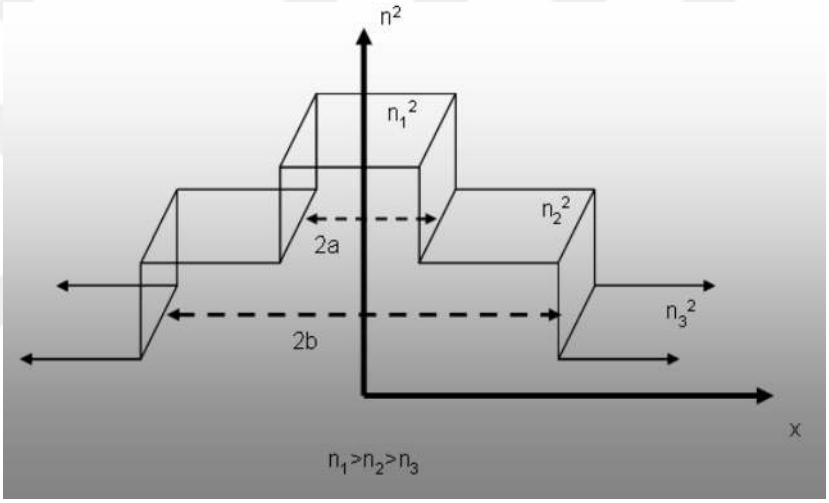

Figure 5.1: The illustration of the five layer slab waveguide [89].

$$\begin{aligned} -h_1 A\sin(h_1 a) &= -h_2 \frac{A\sin(h_1 a)}{\cos(h_2 a)}\sin(h_2 a) \\ \tan(h_1 a) &= \frac{h_2}{h_1}\tan(h_2 a) \end{aligned} \tag{5.11}$$

At $x = b$; $\frac{\partial \xi_{y1}(x)}{\partial x} = \frac{\partial \xi_{y3}(x)}{\partial x}$ and so

$$\begin{aligned} -h_2 \frac{A\sin(h_1 a)}{\cos(h_2 a)}\sin(h_2 b) &= -h_3 \frac{A\sin(h_1 a)}{\cos(h_2 a)}\cos(h_2 b)\, e^{h_3(b-b)} \\ \tan(h_1 b) = h_3 \Rightarrow h_2 &= \frac{1}{b} arctan\left(\frac{h_2}{h_3}\right) \end{aligned} \tag{5.12}$$

substituting Eqn. 5.11 to 5.12

$$\tan(h_1 a) = \frac{h_2}{h_1}\tan(h_2 a) \Rightarrow h_1 a = \arctan\left(\frac{h_2}{h_1}\tan\left(\frac{a}{b}\arctan\left(\frac{h_3}{h_2}\right)\right)\right) \tag{5.13}$$

where $h_1^2 = k^2 n_1^2 - \beta^2$; $h_2^2 = k^2 n_2^2 - \beta^2$; $h_3^2 = \beta^2 - k^2 n_3^2$; $M\pi$ is eliminated because we will study $M = 0$ mode. In addition, exponential terms have not been considered because they are cancelled in confinement factor calculation (electric field is multiplied by its conjugate). If $kn_1 \geq \beta \geq kn_2$ then Eqn. 5.13

$$\begin{aligned} &\tan(h_1 a) = \frac{h_2}{h_1}\tan(h_2 a) \\ &\Rightarrow h_1 a = M\pi + \arctan\left(\frac{h_2}{h_1}\tan\left(\frac{a}{b}\text{arctanh}\left(\frac{h_3}{h_2}\right)\right)\right) \end{aligned} \tag{5.14}$$

where $h_1^2 = k^2 n_1^2 - \beta^2$; $h_2^2 = \beta^2 - k^2 n_2^2$; $h_3^2 = \beta^2 - k^2 n_3^2$; We have two options:

$$\begin{aligned} &\sqrt{\frac{n_1^2 - n_2^2}{n_1^2 - n_3^2}} \leq \frac{h_1}{k\sqrt{n_1^2 - n_3^2}} \leq 1 \quad \textit{condition 1} \\ &0 \leq \frac{h_1}{k\sqrt{n_1^2 - n_3^2}} \leq \sqrt{\frac{n_1^2 - n_2^2}{n_1^2 - n_3^2}} \quad \textit{condition 2} \end{aligned} \tag{5.15}$$

To understand these equations, we may view at relationship between the equations of electric fields, refractive index, propagation constant and wavelength.

$$\Gamma = \frac{\int_0^a \xi_{y1}^2(x,z,t)\,dx}{\int_0^a \xi_{y1}^2(x,z,t)\,dx + \int_a^b \xi_{y2}^2(x,z,t)\,dx + \int_b^c \xi_{y3}^2(x,z,t)\,dx} \tag{5.16}$$

Optical confinement factor calculation can be made merely with above equation. However, electric fields are obtained from the calculations which have refractive indices analysis. These indices are dependent on wavelengths. This condition causes complications and requires different type solution ways.

Above calculations have all analogy about optical confinement factor. We have used an approximation which belongs to M.J.Adams [90] to obtain simply optical confinement factor as

$$v^2 = a^2 k^2 \left(n_1^2 - n_3^2\right) \tag{5.17a}$$
$$u^2 = a^2 \left(k^2 n_1^2 - \beta^2\right) = a^2 h_1^2 \tag{5.17b}$$
$$w^2 = a^2 \left(\beta^2 - k^2 n_3^2\right) = v^2 - u^2 = a^2 h_3^2 \tag{5.17c}$$
$$t^2 = a^2 \left(k^2 n_2^2 - \beta^2\right) = u^2 - v^2 c^2 = a^2 h_2^2 \tag{5.17d}$$
$$t''^2 = a^2 \left(\beta^2 - k^2 n_2^2\right) = v^2 c^2 - u^2 = a^2 h_2''^2 \tag{5.17e}$$

$$c = \frac{n_1^2 - n_2^2}{n_1^2 - n_3^2} \approx \frac{n_1 - n_2}{n_1 - n_3} \tag{5.18}$$

$$u = M\pi + \arctan\left(\frac{t}{u}\tan\left(\arctan\left(\frac{w}{t}\right) - t\left(\frac{b}{a} - 1\right)\right)\right) \tag{5.19}$$

if $t \to it''$

$$u = M\pi + \arctan\left(\frac{t''}{u}\tanh\left(\operatorname{arctanh}\left(\frac{w}{t''}\right) - t''\left(\frac{b}{a} - 1\right)\right)\right) \tag{5.20}$$

if $c \leq u/v \leq 1$

$$\Gamma = \frac{u + \sin u \cos u}{u + \sin u \cos u\left(1 - \frac{u^2}{t^2}\right) + u\left(\cos^2 u + \frac{u^2}{t^2}\sin^2 u\right)\left(\frac{b}{a} - 1 + \frac{1}{w}\right)} \tag{5.21}$$

if $0 \leq u/v \leq c$

$$\Gamma = \frac{u + \sin u \cos u}{u + \sin u \cos u\left(1 - \frac{u^2}{t''^2}\right) + u\left(\cos^2 u + \frac{u^2}{t''^2}\sin^2 u\right)\left(\frac{b}{a} - 1 + \frac{1}{w}\right)} \tag{5.22}$$

Examples for concentration dependence of refractive indices of well- and cladding layer material are given in Table 5.2. From Table 5.2, refractive index of $GaN_xAs_{1-x-y}P_y$ decreases with N. Therefore to satisfy and improve the conditions of internal reflection for the five layer slab waveguide shown in Figure 5.1, refractive index of $GaN_xAs_{1-x-y}P_y$ layer, which is denoted as n_1, must be greater than that of barrier and cladding layer, which are denoted as n_2 and n_3 respectively. To achieve that we need to decrease refractive index of cladding layer. We offer incorporation of Al into GaP and use $Al_zGa_{1-z}P$ as a cladding layer to decrease the refractive index of cladding layer without adding strain to material system. The effects of Al incorporation on the cladding layer is also shown in Table 5.2.

Content	1%	2%	3%	4%
$GaN_xAs_{0.8-x}P_{0.2}$	3.51380	3.47350	3.43818	3.40713

Content	5%	10%	15%	20%
$Al_zGa_{1.0-z}P$	3.38000	3.36000	3.34000	3.32000

Table 5.2: Refractive index for GaNAsP and AlGaP.

5.3 Calculation of Refractive Index and Optical Confinement Factor in Ga(NAsP) by Using the Analytical Model

In the previous section we show how the refractive indices change with material composition. We now want to illustrate at this point the Adachi's model can be used to investigate the refractive index of III-V and III-N-V semiconductors. We assume a total loss of 50 cm^{-1} for the Fabry Perot laser cavity and the cavity length L is taken as 1500μm. The refractive index of GaN is much smaller than that of GaAs and GaP. Therefore the introduction of nitrogen into $GaAs_{1-y}P_y$ decreases the refractive index of $GaN_xAs_{1-x-y}P_y$ QW and so do the index difference between $GaN_xAs_{1-x-y}P_y$ well and GaP barrier. This reduced index difference between well and barrier is expected to cause a decrease in optical confinement factor, Γ. In order to improve Γ, we offer $Al_zGa_{1-z}P$ as a cladding layer. $Al_zGa_{1-z}P$ is nearly lattice matched to GaP barrier in Ga(NAsP)/GaP material system. Thus, a five layer dielectric slab waveguide model is employed to calculate numerical values of optical confinement factor [90] for Ga(NAsP)/GaP/AlzGa(1-z)P. All required parameters are provided in Table 3.1.

Figure 5.2(a) compares the rate of change of optical confinement factor of the two proposed 70Å single quantum well (QW) laser systems of $GaAs_{1-y}P_y$ /GaP /$Al_{0.3}Ga_{0.7}P$ and $GaN_xAs_{1-x-y}P_y$ /GaP /$Al_{0.3}Ga_{0.7}P$ on Si substrates. We first try to show phosphide concentration dependence of Γ for the two QW system taking into account the index of refraction of well, barrier and confining layers at each composition. We choose the aluminium concentration in confining layer as 30% in both offered systems. As can be seen from Figure 5.2(a), $GaAs_{1-y}P_y$ /GaP /$Al_{0.3}Ga_{0.7}P$ material system has a higher confinement factor than that of $GaN_xAs_{1-x-y}P_y$ /GaP /$Al_{0.3}Ga_{0.7}P$ due to the low refractive index values of GaN and GaP. In addition, the increase in phosphide concentration reduces Γ in both systems. Secondly, these calculations show clearly how Γ decreases with increasing nitrogen concentration for $GaN_xAs_{1-x-y}P_y$ /GaP /$Al_{0.3}Ga_{0.7}P$ material system. Thus, the increase in phosphide and nitrogen concentration in well lead a poor photon confinement in $GaN_xAs_{1-x-y}P_y$ /GaP /$Al_{0.3}Ga_{0.7}P$. However, the optical confinement can be improved by means of increasing the Al concentration in cladding layer $Al_zGa_{1-z}P$. As is seen in Figure 5.2(b) compressively strained laser system of $GaN_xAs_{0.9-x}P_{0.1}$ /GaP /Al_zGa_{1-z}Ps optical confinement factor increases with Al concentration and its value approaches to that of the host matrix $GaAs_{0.9}P_{0.1}$. So, the analysis of strained quantum well structure $GaN_xAs_{1-x-y}P_y$ that contains high As-, moderate N- and low P- concentrations

which maintains acceptable strain levels translating into lesser dislocations in the grown material compared to host matrix $GaAs_{1-y}P_y$ (see Figure 3.4), appears to show promising properties as far as optical confinement factor is concerned.

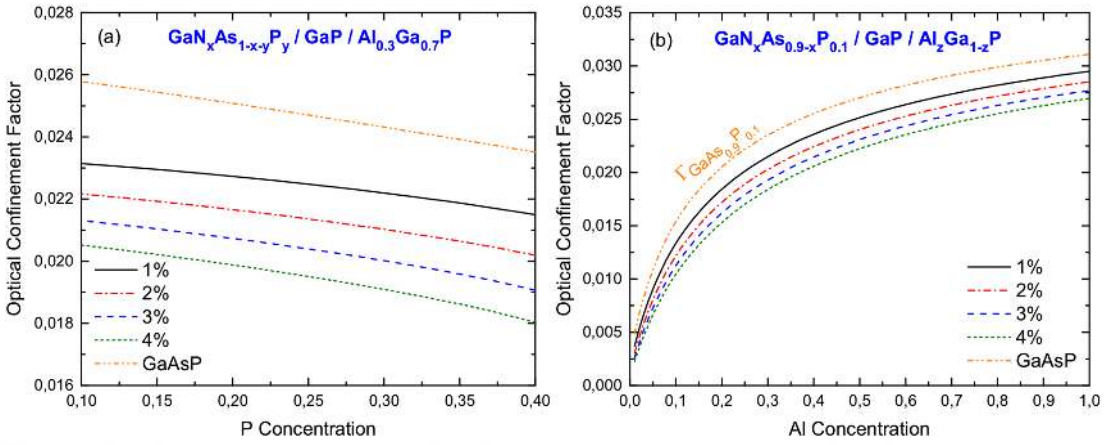

Figure 5.2: (a) The calculated values of optical confinement factor as a function of phosphide concentration in well for $GaAs_{1-y}P_y$ / GaP / $Al_{0.3}Ga_{0.7}P$ and $GaN_xAs_{1-x-y}P_y$ / GaP / $Al_{0.3}Ga_{0.7}P$. b) The variation of Γ versus aluminium concentration in cladding layer for $GaAs_{0.9}P_{0.1}$ / GaP / $Al_zGa_{1-z}P$ and that of $GaN_xAs_{0.9-x}P_{0.1}$ / $Al_zGa_{1-z}P$. The nitrogen concentration is varied between 1% - 4% for quaternary system.

5.4 Summary

In this chapter, we have presented an analysis of concentration dependence of refractive indices and optical confinement for $GaN_xAs_{1-x-y}P_y$/GaP and $GaAs_{1-y}P_y$/GaP material systems on GaP substrates.

Although the band offsets of $GaN_xAs_{1-x-y}P_y$/GaP systems are close to that of the ideal case which leads to have an improved carrier confinement, the optical confinement of $GaN_xAs_{1-x-y}P_y$/GaP laser system is slightly worse than that of $GaAs_{1-y}P_y$/GaP laser systems while holding an advantage on the strain levels over $GaAs_{1-y}P_y$/GaP laser systems. However, the optical confinement can be improved by means of introducing barrier of $Al_zGa_{1-z}P$ to the $GaN_xAs_{1-x-y}P_y$/GaP heterojunction. As a summary, compressively strained laser system of $GaN_xAs_{1-x-y}P_y$ /GaP /$Al_zGa_{1-z}P$ improve optical confinement significantly.

CHAPTER 6

GAIN ANALYSIS IN Ga(NAsP) QWS ON Si SUBSTRATES

6.1 Introduction

We have analysed in previous chapters how band structure, effective mass and optical confinement factor vary with nitrogen and phosphide concentration. The ability to calculate these important parameters allows us to reveal the concentration dependence of carrier density and gain in Ga(NAsP)/GaP QW laser systems. This will aid in the design and optimization of efficient laser device structures of Ga(NAsP)/GaP on Si substrates. In order to provide some insight into basic design rules, we analyse differential gain, transition matrix element, transparency and threshold carrier density, and threshold gain in two of the proposed GaP-based 70Å single quantum well (QW) laser systems of $GaAs_{1-y}P_y$ /GaP and $GaN_xAs_{1-x-y}P_y$/GaP on Si substrates.

6.2 Modelling of Peak Gain

We aim to obtain the band-edge peak gain for electron- and hole carrier density n at the QW band edge using an idealized band model as [91]

$$G_{max} = G_o[1 - e^{-n/n_c} - e^{-n/n_v}] \tag{6.1}$$

with

$$\mathrm{G_o} = \frac{\Gamma E_g \mu^2 m_r}{\varepsilon_\mathrm{o} c \eta \hbar^3 \mathrm{L_z}}, \quad n_{\mathrm{c,v}} = \frac{m_{\mathrm{c,v}} k_B T}{\pi \hbar^2 \mathrm{L_z}} \tag{6.2}$$

where Γ is the optical confinement factor, E_g is the optical energy gap, μ^2 is the squared dipole moment along a polarization of light, m_r is the reduced mass, ε_o is the dielectric constant of vacuum, η refractive index, L_z is the well width, and finally n is the injected carrier density. Transparency occurs when G_{max}=0, and

we calculate the transparency carrier density n_{tr} required for population inversion solving the following of

$$1 - e^{-\alpha} = e^{-\alpha/R_m} \tag{6.3}$$

with $\alpha = n_{tr}/n_v$ and $R_m = m_c/m_v$. The differential material gain at transparency, $\beta = dG_{max}/dn$, is defined as the derivative of the modal gain with respect to the number of charge carriers at transparency in active region and it can be found by differentiating the peak gain in Eqn. 6.1 as a function of carrier density as

$$\beta = \frac{\beta_o E_g}{(1+R_m)} \left[1 + e^{-\alpha}(R_m - 1)\right], \tag{6.4}$$

where $\beta_o = \mu^2\pi/\varepsilon_o cn\hbar k_B T$. Assuming a linear relationship between carrier density n and the peak laser gain g, we can calculate the threshold carrier density n_{th} using the following relationship of

$$n_{th} = n_{tr} + \frac{g_{th}}{\beta}, \tag{6.5}$$

with g_{th} is the threshold material gain and it takes the form of

$$g_{th} = \alpha_a + \frac{(1-\Gamma)}{\Gamma}\,\alpha_c + \frac{1}{\Gamma L}\ln\left(\frac{1}{R}\right) \tag{6.6}$$

where α_a and α_c are the active- and cladding layer losses, respectively, L is the laser cavity length, R is the reflectivity of the end mirrors and finally Γ is the optical confinement factor which defines the fraction of the optical mode power confined in active region.

6.3 Analysis of Peak Gain

Figure 6.1 shows the calculated variation of the differential gain for $GaAs_{1-y}P_y$ /GaP/$Al_{0.3}Ga_{0.7}P$ and that of $GaN_xAs_{1-x-y}P_y$ /GaP/$Al_{0.3}Ga_{0.7}P$ as a function of phosphide concentration in well. Nitrogen concentration dependence of GaN_x $As_{1-x-y}P_y$/GaP/$Al_{0.3}Ga_{0.7}P$ is also revealed. The differential gain in $GaN_xAs_{1-x-y}P_y$ /GaP/$Al_{0.3}Ga_{0.7}P$ is decreased significantly in comparison with the nitrogen free counter part of $GaAs_{1-y}P_y$ /GaP/$Al_{0.3}Ga_{0.7}P$. The concentration dependence of differential gain is determined by the variation of band gap, momentum matrix element and mass ratio with concentration. We can analyze the effect of all these on the differential gain as follows:

- Both band gap and momentum matrix element decrease with increasing nitrogen concentration resulting a decrease in differential gain.

- Mass ratio increases with increasing nitrogen concentration for low P concentration whereas it decreases with increasing nitrogen concentration for high P concentration causing a crossover in differential gain in $GaN_xAs_{1-x-y}P_y$ /GaP/$Al_{0.3}Ga_{0.7}P$ system around 23% of phosphide concentration.

- As an overall, differential gain decreases with increasing P concentration and it decreases/increases as a function of N concentration for low/high values of P concentration.

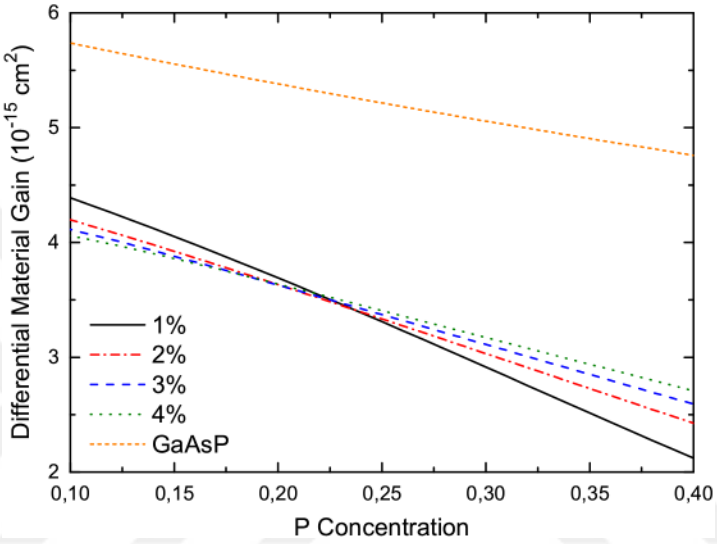

Figure 6.1: The comparison of the differential peak gain of $GaAs_{1-y}P_y$/ GaP/ $Al_{0.3}Ga_{0.7}P$ with that of $GaN_xAs_{1-x-y}P_y$/ GaP/ $Al_{0.3}Ga_{0.7}P$ as a function of phosphide concentration in well. The nitrogen concentration dependence of $GaN_xAs_{1-x-y}P_y$/ GaP/ $Al_{0.3}Ga_{0.7}P$ is also given for 1% - 4 % nitrogen range.

We now determine the transparency and threshold carrier densities of n_{tr} and n_{th} using Eqn.'s 6.3 and 6.5, respectively, for the two laser systems. The theoretical n_{tr} and n_{th} calculations presented in Figure 6.2(a) show that both n_{tr} and n_{th} increase with increasing P concentration in both laser systems. The inset corresponds to the calculations belonging to $GaAs_{1-y}P_y$/ GaP/ $Al_{0.3}Ga_{0.7}P$ system. In addition, the transparency and threshold carrier densities of $GaN_xAs_{1-x-y}P_y$ /GaP/ $Al_{0.3}Ga_{0.7}P$ is higher than that of $GaAs_{1-y}P_y$/ GaP/ $Al_{0.3}Ga_{0.7}P$ due to the variations obtained above. Figure 6.2(a) shows the effect of N concentration of n_{tr} and n_{th} in $GaN_xAs_{1-x-y}P_y$ /GaP/ $Al_{0.3}Ga_{0.7}P$ as well. These presented calculations are interesting that both n_{tr} and n_{th} increase with increasing N concentration for low P values whereas it decreases with increasing N concentration for high P values. A close investigation of Figure 3.7 explains this behaviour

noticing that m_v is being greater than m_c until 38% of P concentration whilst it is smaller than m_c above this point. When m_v is being greater than m_c, the density of states in VB becomes greater than that of CB. This means that the condition for transparency occurs when the quasi-Fermi level for holes is well above to the top of VB and hence quasi-Fermi level for electrons is correspondingly high above the bottom of CB. This means that there is a large spread in the energy distribution of the electrons and only a small percentage of them can directly contribute to gain while all the others are able to recombine spontaneously or via non-radiative processes and hence add to the threshold current. On the other hand, the increase in N and P concentration cause a decrease in compressive strain. This will in turn provide a close matching of the effective masses of m_c and m_v for $GaN_xAs_{1-x-y}P_y$. Then the density of states becomes comparable and quasi Fermi level for VB and CB moves at a similar rate for a given injected carrier density which will be beneficial for device performance.

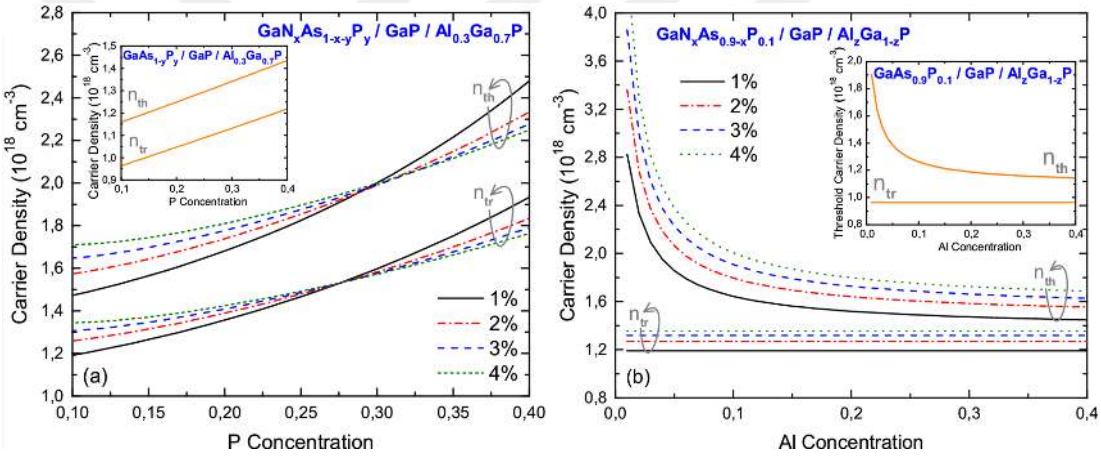

Figure 6.2: The variation of transparency carrier density n_{tr} and threshold carrier density n_{th} a) as a function of phosphide concentration for $GaAs_{1-y}P_y$/ GaP/ $Al_{0.3}Ga_{0.7}P$ (inset) and that of $GaN_xAs_{1-x-y}P_y$ /GaP/ $Al_{0.3}Ga_{0.7}P$, and b) as a function of aluminium concentration in barrier for $GaAs_{0.9}P_{0.1}$/ GaP/ $Al_zGa_{1-z}P$ (inset) and that of $GaN_xAs_{0.9-x}P_{0.1}$/ GaP/ $Al_zGa_{1-z}P$ for varying nitrogen concentrations of 1% - 4%.

In order to achieve the optimal laser performance the transparency and threshold carrier density must have its minimum value whereas the differential gain and transition matrix element must have its maximum value. It is possible to reduce n_{tr} and n_{th} values by means of using $Al_zGa_{1-z}P$ cladding layers. Figure 6.2(b) shows how n_{th} decreases rapidly as a function of aluminium concentration in barrier both for $GaAs_{0.9}P_{0.1}/GaP/Al_zGa_{1-z}P$ (inset) and that of $GaN_xAs_{0.9-x}P_{0.1}/GaP/Al_zGa_{1-z}P$ for varying nitrogen concentrations of 1%-4%.

This rapid decrease is mostly due to the rapid increase in optical confinement factor by means of using $Al_zGa_{1-z}P$ cladding layer.

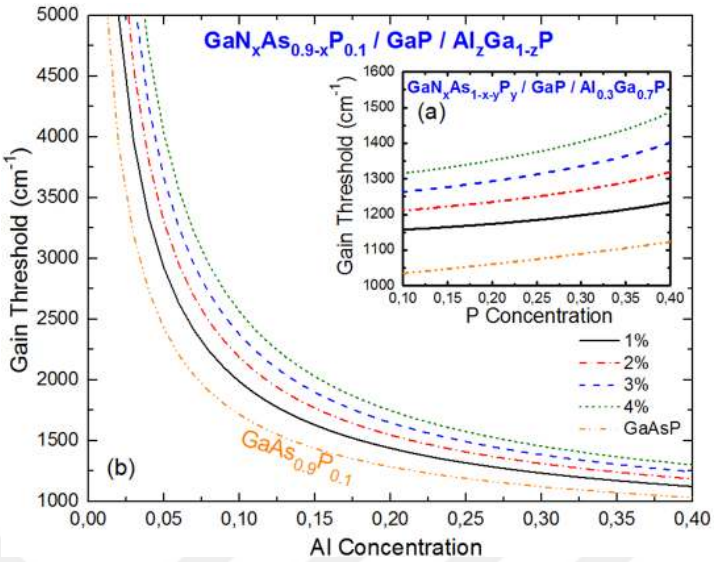

Figure 6.3: The variation of threshold material gain of $GaAs_{1-y}P_y/GaP/Al_zGa_{1-z}P$ and that of $GaN_xAs_{1-x-y}P_y/GaP/Al_zGa_{1-z}P$ for varying nitrogen concentrations of 1% - 4% as a function of a) P concentration in well (inset) and b) Al concentration in barrier.

Finally, we calculate the threshold gain as a function of P concentration in well (inset) and Al concentration in barrier by means of using Eqn. 6.6. Figure 6.3(a) (inset) illustrates the variation of the threshold gain as a function of P concentration in well for varying nitrogen concentrations of 1% - 4%.

It can be observed that an increase in P concentration and a simultaneous reduction in As concentration increases the threshold gain. The increase in N concentration cause a further increase in threshold gain. The increase in threshold gain becomes significant especially at high P concentration. As it is proposed previously it is possible to decrease the threshold gain by means of using $Al_zGa_{1-z}P$ cladding layers as shown in Figure 6.3(b). The rapid decrease in threshold gain is again mostly due to the rapid increase in optical confinement factor by means of using$Al_zGa_{1-z}P$ cladding layer. It has been calculated that an increase in P concentration and a simultaneous reduction in As concentration increase the density of carriers at transparency and threshold and degrades the differential gain. Therefore to obtain the optimal laser performance of lowest possible transparency and threshold carrier density whereas the highest possible differential gain and transition matrix element one must prefer highest possible As- and N- and lowest possible P- concentration in well.

6.4 Summary

We have made a comprehensive theoretical comparative analysis of the gain material properties in $GaAs_{1-y}P_y/GaP/Al_zGa_{1-z}P$ and $GaN_xAs_{1-x-y}P_y/GaP/Al_zGa_{1-z}P$ laser systems on Si substrates. The main objective of this chapter is to exploit the gain properties of the compressively strained Ga(NAsP)/GaP QW heterostructures to design a laser diode. Modelling calculations mainly has been concentrated on the carrier density, differential and threshold gain. Gain properties in $GaN_xAs_{1-x-y}P_y$ clearly shows that laser related parameters such as optical confinement (see Figure 5.2) and effective mass (see Figure 3.7) strongly depend on P and N concentrations. Therefore, we can conclude that when $GaN_xAs_{1-x-y}P_y$ is intended to be used as an active layer in a laser configuration, the route of highest possible As- and N- and lowest possible P- concentration must be followed. By this way

- the transparency and threshold carrier density is minimised,
- the differential gain is maximised.

In summary, these calculations show clearly the relative benefits of the use of the $Al_zGa_{1-z}P$ cladding layers for the proposed $GaN_xAs_{1-x-y}P_y/GaP$ QW laser system.

CHAPTER 7

THEORETICAL ANALYSIS AND COMPARISON TO EXPERIMENTAL RESULTS OF THE VARIATION OF CURRENT DENSITY WITH PRESSURE IN Ga(NAsP) QWS ON GaP

7.1 Introduction

The technological interest in the superior electronic and optoelectronic properties of III–N-V semiconductors promotes research in heteroepitaxy on silicon (Si) substrates for integration in established micro-electronics. Highly mismatched dilute nitride alloy GaNAsP having type-I direct bandgap is a perfect example of promising III-N-V semiconductor. The most remarkable properties of $GaN_xAs_{1-x-y}P_y$ quantum well (QW) lasers are that the ability to be doped both n-type and p-type [92] and have a wide range of material composition due to its quaternary nature enabling bandgap-tailoring as well as lattice matched growth on to GaP substrates. Lattice matched growth on GaP substrates also allows the possibility of this laser material system to be grown on Si(100) substrates as recently shown by Döscher [93]. On the other hand these promising laser diodes on Si substrates have large threshold current densities. This high threshold current density is due to significant non-radiative recombination mechanisms present in the structures mentioned. Therefore an optimised design for the wave guide structures is required to allow the improvements in optical confinement factor and in electrical confinement. It is also necessary to investigate effective loss mechanisms in this laser material system.

It is known that the application of hydrostatic pressure cause an increase in the direct bandgap of the Ga(NAsP) semiconductors. Therefore hydrostatic pressure can be used to vary the interaction between the nitrogen energy level and the conduction band edge of the host matrix GaAsP. So hydrostatic pressure is a useful mean of developing a further understanding of the behaviour of such materials. We present a comprehensive theoretical analysis of dilute nitride highly mismatched quaternary $GaN_xAs_{1-x-y}P_y/GaP/Al_zGa_{1-z}P$ type-I

QW laser structure to reveal the effects of hydrostatic pressure on band structure, optical confinement factor, effective loss mechanisms and threshold current density. The chapter is organized as follows; Pressure dependencies of all band edges is calculated with band anti-crossing (BAC) model and presented in Section 7.2. Nitrogen and pressure dependence of effective mass of GaAsP (host matrix) and $GaN_xAs_{1-x-y}P_y$/GaP is studied in Section 7.3. Aluminium and pressure dependence of optical confinement factor of $GaN_xAs_{1-x-y}P_y$/GaP is studied in Section 7.4. Aluminium, Nitrogen and pressure dependence of carrier density of GaAsP (host matrix) and $GaN_xAs_{1-x-y}P_y$/GaP is studied in Section 7.5. Calculated nitrogen and pressure dependence of threshold current due to direct and phonon-assisted Auger recombination rates are given in Section 7.6. A summary of our conclusions is provided Section 7.7. The theoretical models that have been used throughout the calculations have been provided or cited in each related section.

7.2 Pressure Dependence of the Band Structure

Applied hydrostatic pressure cause an increase in direct bandgap at Γ-point and a reduction in indirect X minima in the band structure of semiconductors. Due to this fact hydrostatic pressure can be used to vary continuously the band structure of a semiconductor material system allowing to a systematic study of the internal electronics and optoelectronic processes. These processes include mostly the loss mechanism of non-radiative Auger recombinations. In order to examine pressure dependence of threshold current of the proposed structure, we first theoretically determine the pressure dependence of band structure over a pressure range of 0-1 GPa. The pressure dependence of the conduction band is taken as [70]:

$$E_0(p) = E_0(0) + \alpha p + \beta p^2 \ \ (eV) \tag{7.1}$$

where $E_0(0)$ is the bandgap of host $GaAs_{1-y}P_y$ and $GaN_xAs_{1-x-y}P_y$ alloy at equilibrium. The constants α and β are the linear and non-linear pressure coefficients, respectively. These pressure coefficients are tabulated in Table 3.1 for direct bandgap binary materials.

Figure 7.1 presents the calculated pressure dependence of Γ-conduction band edge minimum E_M of $GaAs_{1-y}P_y$ using equation 7.1. Our calculation indicates a rapid increase in E_M with an increase in pressure. We also present the calculated pressure dependence of the fundamental energy bandgap E_- of dilute-phosphide-nitride $GaN_xAs_{0.9-x}P_{0.1}$ using BAC model with varying nitro-

gen concentrations of 1% - 4%. The nitrogen level location was obtained by interpolation of isolated N level (E_N) in GaP and GaAs and assumed negligibly vary with pressure [67]. Our calculations shows that the incorporation of nitrogen into $GaAs_{1-y}P_y$ causes a strong reduction in fundamental energy bandgap E_-. This reduction is a result of strong interaction of the conduction band minima with the close-lying N energy level. The rapid decrease in E_- for $GaN_xAs_{0.9-x}P_{0.1}$ is non-monotonic for varying nitrogen concentrations of 1% - 4% at 0 GPa.

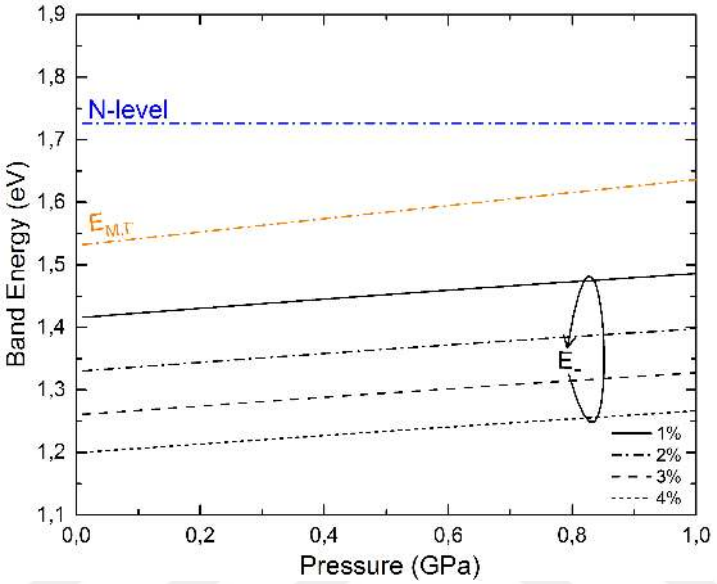

Figure 7.1: The pressure dependence of Γ- conduction band edge minimum energy (E_M) of host matrix $GaAs_{0.9}P_{0.1}$ and fundamental energy gap E_- of quaternary $GaN_xAs_{0.9-x}P_{0.1}$ for varying nitrogen concentrations of 1%-4%. The nitrogen energy level E_N is taken as insensible to applied pressure.

It is clear that the quaternary $GaN_xAs_{0.9-x}P_{0.1}$ provides more degree of freedom in comparison to ternary $GaAs_{1-y}P_y$ in order to engineer a suitable E_- energy band with a narrow bandgap. In addition, the nitrogen incorporation into $GaAs_{1-y}P_y$ lets the required adjustment of the lattice constant to that of the GaP. $GaAs_{1-y}P_y$/GaP structure is compressively strained and the magnitude of strain decreases with increasing phosphide concentration. The incorporation of N into $GaAs_{1-y}P_y$ cause further reductions in compressive strain. This rapid reduction in the magnitude of compressive strain with an increase in phosphide- and nitrogen-concentration in $GaN_xAs_{0.9-x}P_{0.1}$ brings an advantage for a uniform growth.

The calculated pressure dependence of band edges presented in Figure 7.1 indicates that both E_M and E_- shifts to higher energies with increasing pres-

sure over a pressure range of 0-1 GPa. The pressure dependent variations of E_- for different nitrogen concentrations show a similar trend. However the Γ-conduction band edge minimum E_M of GaAsP and the fundamental bandgap E_- of $GaN_xAs_{0.9-x}P_{0.1}$ shift at different rates under hydrostatic pressure. Clearly E_- of $GaN_xAs_{0.9-x}P_{0.1}$ has a weaker pressure dependence than the direct bandgap of host matrix $GaAs_{1-y}P_y$. This allows us to continuously tune the repulsion effects between the energy states using hydrostatic pressure. These nitrogen concentration and pressure dependent variations of E_N and E_- will play an important role for the determination of effective mass that will be provided in the following section.

7.3 Pressure Dependence of the Effective Mass

As we have shown in Figure 7.1, Γ-conduction band edge minimum (E_M) of $GaAs_{0.9}P_{0.1}$ and the fundamental bandgap (E_-) of $GaN_xAs_{0.9-x}P_{0.1}$ broadens with hydrostatic pressure. This change in the band structure is expected to cause an increase in the effective mass of electron (m^*). In order to verify this prediction, we determine the pressure induced modifications of electron effective mass in $GaN_xAs_{0.9-x}P_{0.1}$ with nitrogen concentration and compare with that of $GaAs_{0.9}P_{0.1}$. The effective mass (m_M) of $GaAs_{0.9}P_{0.1}$ is calculated taking into account the broadening in the bandgap of the host material through the k·p relation [94] of

$$\frac{m_0}{m_e^{\Gamma}(P)} = 1 + \frac{E_P^2}{3}\left(\frac{2}{E_0(p)} + \frac{1}{E_0 + \Delta_0(p)}\right). \tag{7.2}$$

Here E_0 corresponds to $E_{M,\Gamma}$, E_p is the momentum matrix element and Δ_0 is spin-orbit splitting energy. All these parameters are tabulated in Table 3.1. The effective mass of $GaN_xAs_{0.9-x}P_{0.1}$ material system is calculated using the modified band anti-crossing model as

$$m^* = \frac{m_0}{1 + \frac{E_P^2}{3}\left(\frac{2}{E_0(p)} + \frac{1}{E_0+\Delta_0(p)}\right)}\left(1 + \frac{V_{MN}^2}{(E_N - E_-(p))^2}\right). \tag{7.3}$$

Equation (7.3) shows how the effective mass is closely related to energy bandgap. Our calculated results are presented in Figure 7.2 and these variations show a pressure induced enhancement of electron effective mass for both material systems as we expect. The results can be analysed as follows:

- The effective mass of $GaN_xAs_{0.9-x}P_{0.1}$ material system is remarkably greater than that of the host matrix element $GaAs_{0.9}P_{0.1}$.

- The effective mass of $GaN_xAs_{0.9-x}P_{0.1}$ increases with increasing N concentration. These variations point out that the incorporation of 1% N concentration yields a rapid increase in the effective mass and a further increase in N concentration cause a slower increment.

- The effective mass of both $GaAs_{0.9}P_{0.1}$ and $GaN_xAs_{0.9-x}P_{0.1}$ increase as applied pressure increases. It is noted that the effective mass of quaternary $GaN_xAs_{0.9-x}P_{0.1}$ material system strongly depends on pressure whereas pressure dependence of effective mass of ternary $GaAs_{0.9}P_{0.1}$ is weaker.

- The effective mass of $GaN_xAs_{0.9-x}P_{0.1}$ alloy tend to have a similar value at high pressure.

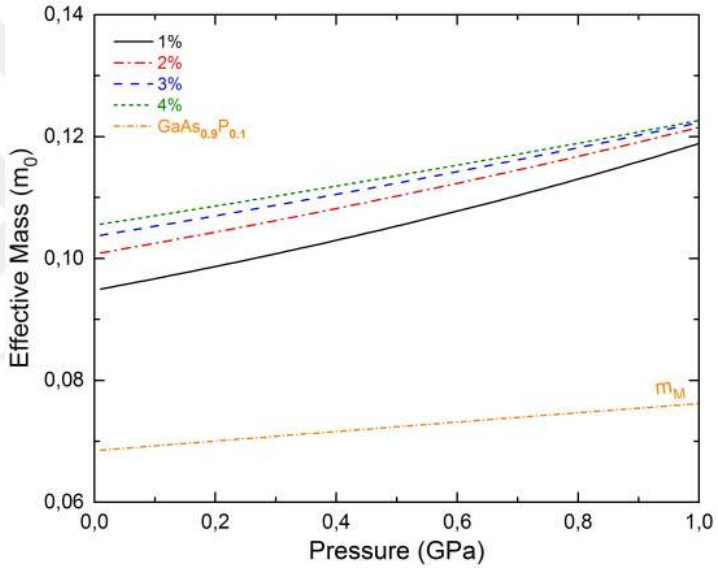

Figure 7.2: The variation of the effective mass m_M of electron in $GaAs_{0.9}P_{0.1}$ and $GaN_xAs_{0.9-x}P_{0.1}$ as a function of pressure for varying nitrogen concentrations of 1% - 4% using band anti-crossing model.

7.4 Pressure Dependence of the Optical Confinement Factor

Photon confinement is one of the important requirement to satisfy the lasing conditions. We use the five layer dielectric slab waveguide model, which is discussed elaborately in Chapter 5, to calculate optical confinement factor (Γ) [90] for $GaN_xAs_{1-x-y}P_y$/GaP/ $Al_zGa_{1-z}P$ taking into account the index of refraction of confining and barrier layers. All the required binary parameters are provided in Table 3.1. Since the refractive index of GaN is much smaller than that

of GaAs, the incorporation of nitrogen into $GaAs_{1-y}P_y$ decreases the refractive index of well layer. Thus in order to improve the optical confinement factor (Γ), we offer $Al_zGa_{1-z}P$ as a cladding layer which is nearly lattice matched to GaP barrier in $GaN_xAs_{1-x-y}P_y$/GaP material system. The calculated rate of change of Γ as a function of Al concentration and pressure for 10% and 20% of phosphide concentrations is given in Figure 7.3(a) for 1% of N and in Figure 7.3(b) for 3% of N. We take into account the index of refraction of well and confining layers at each composition.

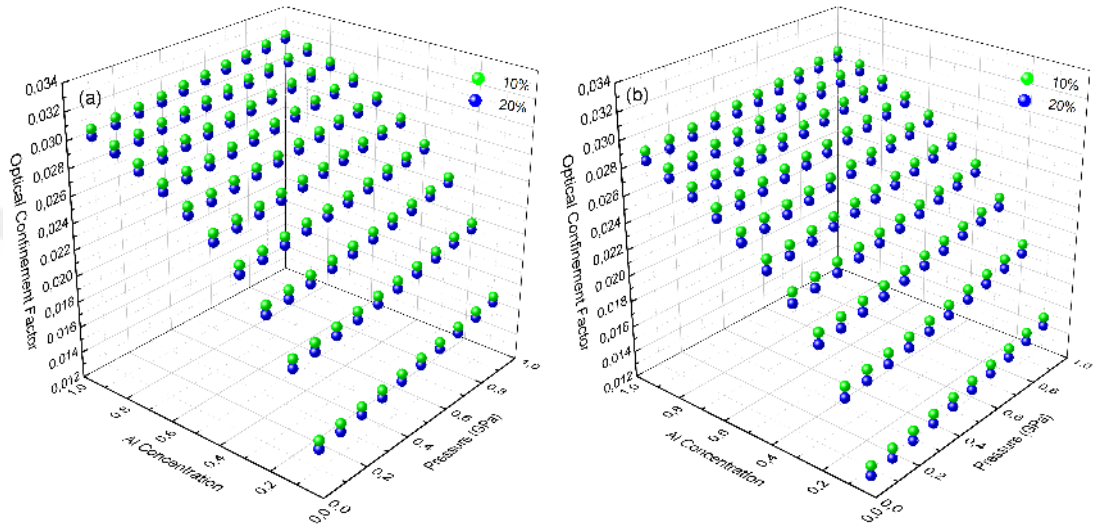

Figure 7.3: The calculated values of optical confinement factor Γ as a function of Al concentration in cladding-layer and applied pressure for 10% and 20% of phosphide concentrations in a) $GaN_{0.01}As_{0.99-y}P_y$/ GaP/ $Al_zGa_{1-z}P$ and b) $GaN_{0.03}As_{0.97-y}P_y$/ GaP/ $Al_zGa_{1-z}P$ using five layer dielectric slab waveguide model.

It is clear from the plotted data, an increase in phosphide and nitrogen concentration in well cause a decrease in Γ due to the low refractive index values of GaN and GaP. As a result, the optical confinement factor of $GaN_xAs_{1-x-y}P_y$/ GaP/ $Al_zGa_{1-z}P$ becomes smaller than that of host matrix $GaAs_{1-y}P_y$ leading a poor optical confinement. However, the optical confinement can be improved by means of increasing the Al concentration in cladding-layer of $Al_zGa_{1-z}P$. As is seen in Figure 7.3 the optical confinement of compressively strained laser system of $GaN_xAs_{1-x-y}P_y$/GaP/$Al_zGa_{1-z}P$ increases rapidly with increasing Al concentration in cladding-layer. Thus strained quantum well structure $GaN_xAs_{1-x-y}P_y$ that contains high As-, low P- and moderate N- concentration with GaP barriers and $Al_zGa_{(1-z)}P$ cladding-layers offers acceptable strain levels which also translates into lesser dislocations in the grown material and appears to show promising

properties as far as optical confinement factors are concerned. As it also seen from Figure 7.3 the optical confinement factor increases with increasing pressure.

7.5 Pressure Dependence of the Carrier Density

The increase in N concentration will result a narrow bandgap and an increased effective mass. The increase in effective mass will determine the amplitude between electron-electron and electron-phonon interactions. These variations directly influence the threshold carrier density and also the non-radiative recombination mechanism of the material system which determines the performance of laser device. Therefore, an optimization of all these parameters can be described as below:

- The calculated variations shown in Figure 7.4 clearly states that the increase in Al concentration decreases the threshold carrier density (n_{th}). This reduction saturates around 40% of Al concentration. As it is stated previously the optical confinement factor Γ has been increased with an increase in Al concentration. This increase in Γ results a decrease in threshold material gain leading a decrease in n_{th} too. On the other hand, transparency carrier density (n_{tr}) is independent of Al concentration. Additionally, the increase in N concentration yields much higher n_{th}'s as well.

- The pressure dependence of n_{th} comes from the pressure dependence of n_{tr} as it is a major parameter, see Eqn. 6.5. Transparency carrier density is mainly determined by the effective masses of electrons and holes. As the electron effective mass (m_c) increases under the influence of applied pressure, the mass ratio (R_m) also increases. Therefore, n_{tr} increases, see Eqn. 6.4, causing an increase in n_{th}. Additionally, the increase in N concentration yields higher n_{tr}'s as well.

- Both transparency carrier density n_{tr} and threshold carrier density n_{th} increase with pressure. It is clear from Figure 7.4 that the increase in n_{tr} and n_{th} with pressure is faster for low N concentration than that of high N concentration. This is due to the variation in effective mass with respect to individual N concentration; for low N concentration the variation in effective mass is higher whereas it is lower for high N concentration as indicated in Figure 7.2

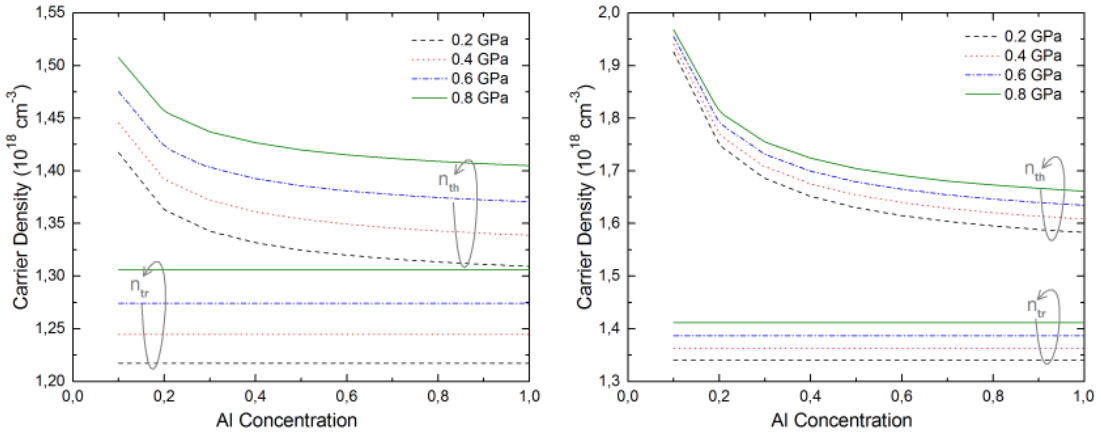

Figure 7.4: The calculated values of transparency and threshold carrier density as a function of Al concentration in the cladding-layer and applied pressure for a) $GaN_{0.01}As_{0.89}P_{0.1}/GaP/Al_zGa_{1-z}P$ and b) $GaN_{0.03}As_{0.87}P_{0.1}/GaP/Al_zGa_{1-z}P$.

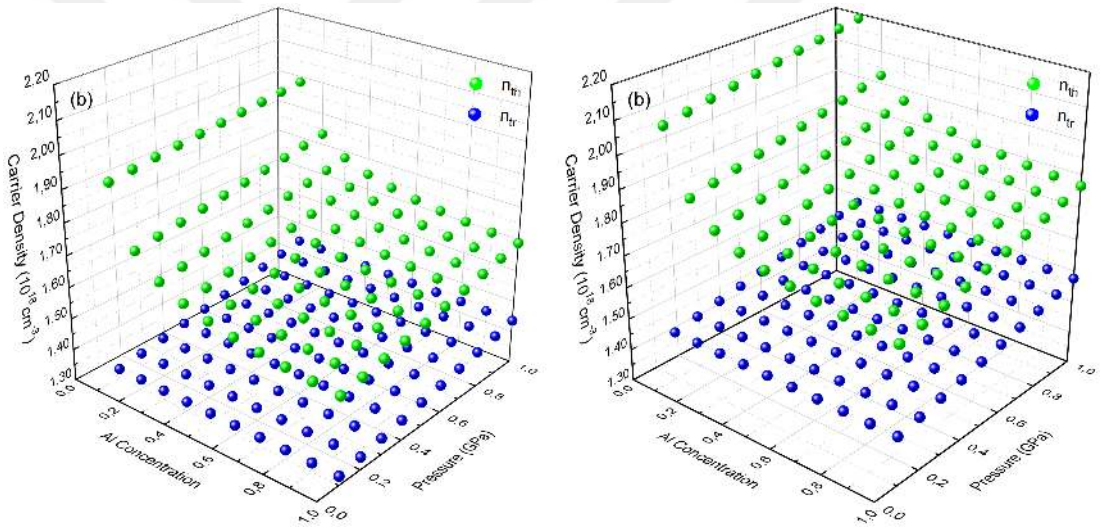

Figure 7.5: The variation n_{tr} andn_{th} versus Al concentration in the cladding-layer and applied pressure for a) $GaN_{0.03}As_{0.87}P_{0.1}/GaP/Al_zGa_{1-z}P$ and b) $GaN_{0.03}As_{0.77}P_{0.2}/GaP/Al_zGa_{1-z}P$.

Figure 7.5 shows the variation of n_{tr} and n_{th} values as a function of applied pressure and Al concentration in cladding-layer for 10% and 20% phosphide concentration. The nitrogen concentration is held at 3%. As clearly seen from Figure 7.5, n_{tr} increases with increasing phosphide concentration and pressure. Therefore, in order to keep the n_{tr} values as low as possible, one should prefer the lowest possible phosphide concentration. As we have shown in Figure 7.3 optical confinement factor Γ decreases with phosphide concentration. This reduction cause a significant increase in n_{th} with an increase in phosphide concentration

as illustrated in Figure 7.5. Therefore, an increase in phosphide concentration decreases the effectiveness of aluminium incorporation to reduce the threshold carrier density.

7.6 Pressure Dependence of the Threshold and Radiative Current Density and Comparison to Experimental Results

We now investigate the normalized radiative current density (J_{rad}) versus pressure for different nitrogen concentrations at 300K, see Figure 7.7(a). As seen from these variations radiative current density increases with pressure and nitrogen concentration. Even though the effective mass of electron increases with pressure, the broadening in bandgap and the increment in threshold carrier concentration cause an increase in normalized radiative current density with pressure. These theoretical results are in good agreement with the experimental data taken at 100K by Chamings et. al. [66].

To make an accurate analysis of the threshold current density (J_{th}), we need to understand how intrinsic loss mechanism contributes to non-radiative recombination, which affects the device performance negatively. For the opto-electronic devices that operate in long wavelength region, Auger recombination mechanism, can be considered as a major intrinsic loss mechanism. In Auger recombination , an electron and a hole recombine across the bandgap without emitting a photon, instead this energy is used up by a third carrier to promote itself into a higher energy level. Such processes are very important for narrow bandgap lasers where this process causes carrier recombination without producing useful photons, therefore causing an increase in the threshold current density (J_{th}). There are two possible Auger recombination mechanism as illustrated in Figure 7.6: band-to-band (direct) and phonon-assisted Auger recombination processes which contributes to (J_{th}). When the recombination energy of an electron and hole is used up by an electron to promote itself into a higher energy level in the conduction band, this process is called CHCC process. Alternatively, the recombination energy can be used up by a hole to promote itself deeper into the valance band. This process is called CHSH process.

Auger recombination process involves three carriers and using Boltzmann statistics, the Auger term varies as n_{th}^3. The threshold current density is simply given by

$$J_{th} = Cn_{th}^3 \tag{7.4}$$

where C is the Auger recombination coefficient. This expression is based on Boltz-

mann statistics, parabolic conduction and valance bands, and assumes therefore that the Auger term C is not carrier density dependent.

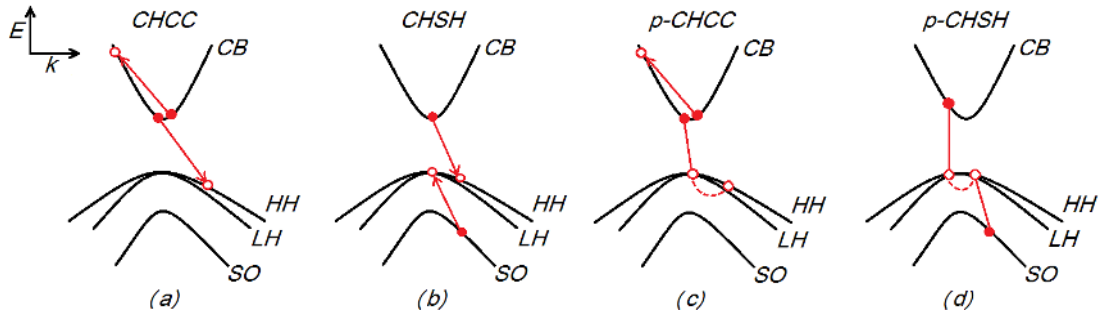

Figure 7.6: Auger processes can be categorized as follows: a) Direct CHCC, b) direct CHSH, c) phonon-assisted CHCC and d) phonon-assisted CHSH.

Direct Auger processes

The direct Auger recombination rate can be expressed as [95]

$$C_d = C_o e^{-E_a/k_B T} \tag{7.5}$$

where E_a is the activation energy which can be written for CHCC process as

$$E_a\left(CHCC\right) = \frac{m_c}{m_c + m_{hh}} E_g \tag{7.6}$$

$$C_o\left(CHCC\right) = \frac{4\pi}{\hbar}\frac{e^4}{\varepsilon^2}\frac{m_c\left(m_{hh}+m_c\right)}{\left(2m_{hh}+m_c\right)^2}\frac{\left|M_{ee}\right|^2}{k_B T} \tag{7.7}$$

where m_c and m_{hh} are the conduction band electron and valence band heavy-hole mass respectively. $|M_{ee}|$ is the matrix element of the electron-electron interaction which can be taken for the CHCC process as [95]

$$\left|M_{ee}\right|^2\left(CHCC\right) = \left(\frac{\hbar^2}{2m_o}\right)^2 \frac{m_o}{m_c}\frac{E_p}{3E_g^3} \tag{7.8}$$

Substituting Equation (7.6), Equation (7.7) and Equation (7.8) into Equation (7.5) and considering only pressure dependent terms, the direct Auger recombination rate for the CHCC process becomes

$$C_d\left(CHCC\right) \propto \frac{m_o\left(m_{hh}+m_c\right)}{\left(2m_{hh}+m_c\right)^2}\frac{1}{E_g^3}\exp\left(-\frac{m_c}{m_c+m_{hh}}\frac{E_g}{k_B T}\right) \tag{7.9}$$

Using the same model, the activation energy and coefficient for the direct CHSH Auger process can be written as

$$E_a\left(CHSH\right) = \frac{m_s\left(E_g-\Delta\right)}{2m_{hh}+m_c-m_s} \tag{7.10}$$

$$C_o\left(CHSH\right)=\frac{4\pi}{\hbar}\frac{e^4}{\varepsilon^2}\left(\frac{m_{hh}}{m_v}\right)^2\frac{m_s\left(2m_{hh}+m_c-m_s\right)}{\left(2m_{hh}+m_c\right)^2}|M_{ee}|^2 \tag{7.11}$$

with the matrix element for the electron-electron interaction in the CHSH process given by

$$|M_{ee}|^2\left(CHSH\right)=\left(\frac{\hbar^2}{2m_o}\right)^2\frac{f_{CH}f_{SH}}{E_g\Delta} \tag{7.12}$$

where f_{CH} and f_{SH} are oscillator strengths which can be represented in the Kane model by [95]

$$f_{CH}=\frac{E_p}{3E_g}, f_{SH}=\frac{E_p}{3\Delta\left(E_g+\Delta\right)}\frac{\hbar^2k_2^2}{2m_o}\left(1+\frac{m_s}{m_o}\right) \tag{7.13}$$

where E_p is the energy equivalent of the momentum matrix element which is evaluated for different semiconductors by Lawaetz [95]. Here k_2 is the solution of

$$E_g-\Delta-\varepsilon_s\left(k_2\right)=0. \tag{7.14}$$

Thus $|M_{ee}|^2$ can be written as

$$|M_{ee}|^2\left(CHSH\right)=\left(\frac{\hbar^2}{2m_o}\right)^2\frac{E_p^2}{9E_g\Delta\left(E_g+\Delta\right)} \tag{7.15}$$

Similarly, the pressure dependence of the direct CHSH Auger rate can be found by substituting Equation (7.15), Equation (7.11) and Equation (7.10) into Equation (7.5)

$$\begin{aligned}C_d\left(CHSH\right)\propto&\left(\frac{m_{hh}}{m_v}\right)^2\frac{m_s\left(2m_{hh}+m_c-m_s\right)}{\left(2m_{hh}+m_c\right)^2}\frac{1}{E_g\Delta^2\left(E_g+\Delta\right)}\\&\times\exp\left(-\frac{m_s}{2m_{hh}+m_c-m_s}\frac{E_g-\Delta}{k_BT}\right)\end{aligned} \tag{7.16}$$

where m_s is the mass of the spin-split-off band, Δ the spin-split off energy, and $m_v=m_{hh}+m_{lh}$.

Phonon-assisted Auger processes

In phonon-assisted Auger process conservation of momentum can be fullfilled by the phonon (see Figure 7.6). The phonon-assisted Auger recombination rate is given by Gönül [95] as

$$C_p=\frac{A}{2\hbar^3}\left(\frac{4\pi e^2}{\varepsilon}\right)^2m_{hh}\bar{\mu}\frac{|M_{ep}|^2|M_{ee}|^2}{e^{\hbar\omega/k_BT}-1}\left[\frac{1}{\left(\bar{\mu}\bar{E}_g+\hbar\omega\right)^2}+\frac{e^{\hbar\omega/k_BT}}{\left(\bar{\mu}\bar{E}_g-\hbar\omega\right)^2}\right] \tag{7.17}$$

with

$$\bar{E}_g=E_g, \bar{\mu}=m_c/m_{hh} \tag{7.18}$$

for CHCC process and

$$\bar{E}_g = E_g - \Delta, \bar{\mu} = m_s/m_{hh} \tag{7.19}$$

for CHSH process. A is the area of the QW, $\bar{\mu}E_g$ is the kinetic energy associated with the forbidden intermediate state, and $\hbar\omega$ is the phonon energy. In addition to electron-electron interaction $|M_{ee}|$, in this case the electron-phonon interaction $|M_{ep}|$ is involved and this is described by [95]

$$|M_{ep}|^2 = \frac{\Omega_0}{AL_z}\frac{D^2\hbar\omega}{2Mv_s^2} \tag{7.20}$$

where D is the deformation potential, v_s is the velocity of the sound and M is the sum of the masses of the atoms in the elementary cell of volume Ω_0. The matrix element for electron-electron interaction $|M_{ee}|$ is given by Equation 7.8 and 7.15 for the CHCC and CHSH Auger processes, respectively. Therefore, the pressure dependence of the CHCC Auger rate can be derived by substituting Equation 7.18, Equation 7.20, and Equation 7.8 into Equation 7.17, gives

$$C_p(CHCC) \propto m_o\left(\frac{m_{hh}}{m_c}\right)^2\left(\frac{1}{E_g^5}\right). \tag{7.21}$$

Similarly, substitution of Equation 7.15, Equation 7.19, and Equation 7.20 into Equation 7.17 yields

$$C_p(CHSH) \propto \frac{m_{hh}^2}{m_s}\frac{1}{E_g\Delta^2\left(E_g+\Delta\right)\left(E_g-\Delta\right)^2} \tag{7.22}$$

Using these expressions, the pressure dependence of threshold current density for direct and phonon-assisted Auger rates in $GaN_xAs_{0.9-x}P_{0.1}/GaP/Al_{0.3}Ga_{0.7}P$ for different nitrogen concentrations are calculated and presented in Figure 7.7 over a pressure range of 0-1 GPa. The pressure dependence of direct and phonon-assisted CHCC and CHSH Auger rates, C's, have been determined at 300 K using above expressions [96] based on parabolic bands and Boltzmann approximations. The calculated results that are illustrated in Figure 7.7 and can be summarized as follows:

- J_{th} due to direct and phonon-assisted Auger CHCC and CHSH processes increase with increasing pressure as shown in Figure 7.7. Thus these non-radiative recombination processes becomes significant with an increase in bandgap.

- J_{th} due to direct CHSH Auger process is insignificant at low pressure and it becomes significant with an increase in pressure, see Figure 7.7(a).

- J_{th} due to phonon assisted Auger processes varies strongly with nitrogen concentration, see Figure 7.7(b). Phonon-assisted CHSH process becomes an insignificant loss mechanism at high pressure region for highly N incorporated material systems. In contrast, J_{th} due to phonon-assisted CHCC Auger process increases with both N concentration and pressure.

- J_{th} due to direct CHCC process increases more rapidly with pressure than the others. As a result direct CHCC can be considered as the major loss mechanism at 300K. Therefore, there is a photon loss and the energy of this lost photon is absorbed by an electron in conduction band to promote itself into a higher lying energy.

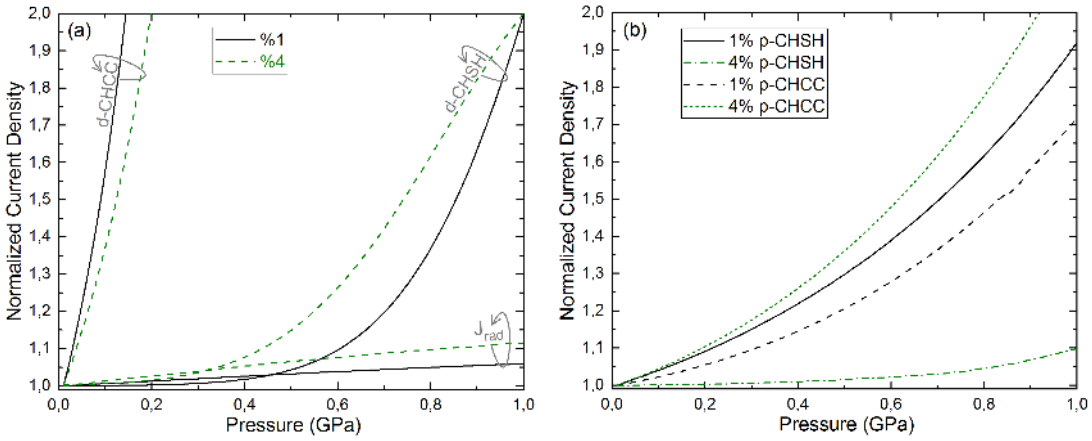

Figure 7.7: Theoretical values of normalized threshold current density corresponding to a) radiative and direct CHCC and CHSH processes and b) phonon-assisted CHCC and CHSH processes for GaN_x $As_{0.9-x}P_{0.1}/GaP/Al_{0.3}Ga_{0.7}P$ as a function of pressure for %1 and %4 nitrogen concentrations at 300K.

As an overall, it can be concluded that the unusual increase of the Auger threshold current density with pressure in $GaN_xAs_{0.9-x}P_{0.1}$ is due to the rapid increase in threshold carrier density.

There exists an experimental data of threshold current density for $GaN_{0.04}$ $As_{0.8}P_{0.16}/GaP/Al_{0.23}Ga_{0.77}P$ material system obtained by Chamings at el [66]. These experimental values are obtained at 100K. In order to provide a comparison of our threshold current calculations with that of the experimental results, we repeat our calculations for $GaN_{0.04}As_{0.8}P_{0.16}/GaP/Al_{0.23}Ga_{0.77}P$ at 300K. We perform our calculations at 300 K since there is no available consistent parameter set obtained at 100 K. Our corresponding results are illustrated in Figure 7.8. As can be seen from these variations our calculations belonging radiative

and non-radiative parts are in agreement with experimental results. Keeping the temperature difference in our mind, we can state that CHCC process dominates the threshold current density.

The threshold current of diode lasers typically increases with temperature [97]. Therefore we should expect that our calculated Auger recombination rates and the corresponding threshold current densities at 300 K must be greater than that of the experimental values obtained at 100K. The comparison of the experimental data obtained by Chamings at el [66] with that of our calculated results provided in Figure 7.8 shows that this is indeed the case.

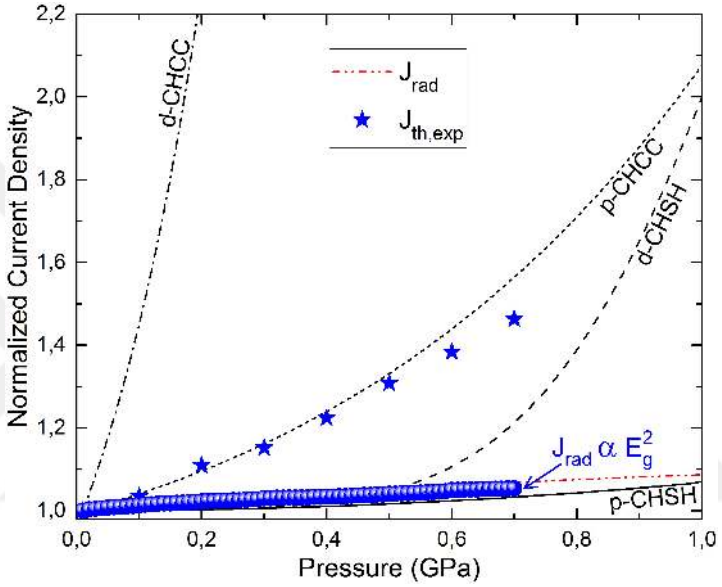

Figure 7.8: Experimental (at 100K) [2] and our theoretical normalized current density (at 300K) corresponding to $GaN_{0.04}As_{0.8}P_{0.16}$/ GaP/ $Al_{0.23}Ga_{0.77}P$ as a function of pressure.

Finally, in order to reveal the overall effect of phosphide concentration on non-radiative threshold current density we provide a comparison of the current density of highly strained nitrogen-free $GaAs_{1-y}P_y$ with that of $GaN_{0.03}As_{0.97-y}P_y$ as a function of pressure for 10% and 20% phosphide concentrations at 300K. We kept the N concentration as being 3%. A close investigation of Figure 7.9 points out the followings;

- The normalized threshold current density due to different Auger processes increases with pressure at different rates. These differences arise as a result of the increase in threshold carrier density with increasing pressure and the different rate of increase of Auger recombination processes with

hydrostatic pressure.

- The comparison of normalized threshold current density due to different Auger processes for ternary $GaAs_{1-y}P_y$ with that of quaternary $GaN_x As_{1-x-y}P_y$ shows that the incorporation of N into $GaAs_{1-y}P_y$ decreases the threshold current density, see Figure 7.9(a).
- The threshold current density increases with P concentration for both direct and phonon assisted processes apart from direct CHCC process.

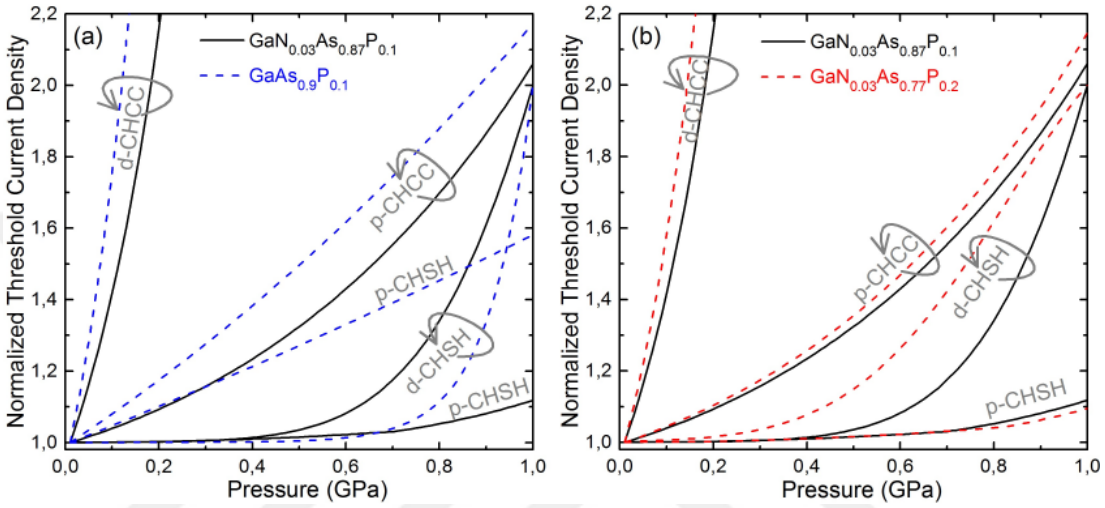

Figure 7.9: Normalized threshold current density corresponding to direct and phonon-assisted Auger rates for a) $GaAs_{0.9}P_{0.1}$/ GaP/ $Al_{0.3}Ga_{0.7}P$ and $GaN_{0.03}As_{0.87}P_{0.1}$/ GaP/ $Al_{0.3}Ga_{0.7}P$ b) $GaN_{0.03}As_{0.97-y}P_y$/ GaP/ $Al_{0.3}Ga_{0.7}P$ containing 10% and 20% P concentration in terms of pressure.

7.7 Summary

The results of a theoretical threshold current density of dilute nitride phosphide $GaN_xAs_{1-x-y}P_y$ well material with GaP barriers and $Al_zGa_{1-z}P$ cladding layer on GaP substrates and hence on Si substrates is provided for the first time up to our knowledge. We have shown that optical confinement factor increases with an increase in Al concentration in cladding layer which is essential for better optical confinement. It has been calculated that the incorporation of N into GaAsP increases the effective mass of electron causing the quaternary $GaN_xAs_{1-x-y}P_y$ having an idealized band structure. The pressure dependent calculations showed that all Auger recombination rates and threshold carrier density increase with hydrostatic pressure. These cause in turn an increase in threshold current density which is in agreement with experimental data.

It has been shown that the threshold current density of $GaN_xAs_{1-x-y}P_y$/$GaP/Al_zGa_{1-z}P$ is lower than that of nitrogen free counterpart. In order to lower the threshold current density one should prefer $GaN_xAs_{1-x-y}P_y/GaP/Al_zGa_{1-z}P$ material system with a higher As concentration since it provides better carrier and optical confinement. Threshold current density J_{th} due to different Auger processes have shown that CHCC Auger mechanism is the most important loss mechanism in $GaN_xAs_{1-x-y}P_y/GaP/Al_zGa_{1-z}P$ QW laser systems at 300K. On the other hand, J_{th} due to phonon-assisted CHSH mechanism is the less significant one in the same material system. Therefore, CHCC process should be the primary concern for optimization of Ga(NAsP)/GaP laser devices for all N concentrations.

CHAPTER 8

THESIS SUMMARY AND FUTURE WORK

The work carried out in this thesis is the results of a detailed comparative theoretical analysis of dilute nitride direct bandgap $GaN_xAs_{1-x-y}P_y/GaP$ as well as $GaAs_{1-y}P_y/GaP$ alloys on Si substrates. The nitrogen and phosphide concentration dependence of band gap, band alignment, strain and effective mass is studied, and their influence on optical gain are identified. Optical confinement factor, differential gain, transparency and threshold carrier density, and threshold gain as functions of nitrogen and phosphide concentration in well and aluminium concentration in barrier are determined. We have shown that it is practical to engineer the band gap of $GaN_xAs_{1-x-y}P_y/GaP$ in comparison to $GaAs_{1-y}P_y$ due to its quaternary nature which provides more degree of freedom to engineer suitable E_- energy band. Although conclusions of each chapter have already been presented at the end of the related chapter, we briefly summarize the major conclusions that could be derived from the thesis work and gather them in this chapter.

Our theoretical calculations indicate that incorporation of nitrogen concentration into host matrix $GaAs_{1-y}P_y$ improves the band alignment and effective mass of carriers of $GaN_xAs_{1-x-y}P_y$ determinedly. The calculations of optical confinement factor Γ by using five layer dielectric slab waveguide model indicates that optical confinement factor of $GaN_xAs_{1-x-y}P_y/GaP$ is poor. The combined effect of the effective mass and optical confinement factor on differential gain, transparency and threshold carrier density, and threshold gain in $GaN_xAs_{1-x-y}P_y/GaP$ degrades compared to that of highly strained $GaAs_{1-y}P_y$. However, the optical confinement factor of $GaN_xAs_{1-x-y}P_y/GaP$ can recover by means of using $Al_zGa_{1-z}P$ cladding layer. Our calculated results suggest that carrier confinement can be markedly improved and strain values are decreased with introduction of N concentration into host matrix $GaAs_{1-y}P_y$ while reducing the threshold current of the laser device generated by the dominant loss mechanism direct CHCC process. Therefore, $GaN_xAs_{1-x-y}P_y/GaP/Al_zGa_{1-z}P$

compressively strained type I QW with larger As and N concentration can be offered as an innovative laser system on Si substrates.

Recent experiments and theoretical investigations have shown that nitrogen-based heterostructures have an important role in future device applications because of their unusual fundamental properties. Ga(NAsP) and related materials is the center of great interest as QW lasers to be used in telecommunication. There are great number of studies about Ga(NAsP) being a successful candidate for high speed transistors, high efficient solar cells, long wavelength infrared photodetectors etc. As a future work, we want to deal with transport properties of Ga(NAsP) quantum wells, wires and dots and investigate surface characteristics of N-based layers.

Band gap, effective mass and spin-orbit-splitting energy are the most important band structure parameters which determine the Auger recombination mechanisms. As we have shown that incorporation of N and Bi into GaAs results a unique material system Ga(NAsBi) whose bandgap corresponds to a wide energy spectrum in the long wavelength region. This narrow bandgap property arises the question of how does the increased spin-orbit splitting band interact with the bandgap? As a future work we aim to reveal the consequences of strong increase in spin-orbit-splitting energy with increasing Bi composition on the Auger recombination loss mechanisms.

REFERENCES

[1] Takahashi K., Yoshikawa A., Sandhu A. (2007). Wide Bandgap Semiconductors: Fundamental Properties and Modern Photonic and Electronic Devices. Springer.

[2] Kasap S., Capper P. (2007). Springer Handbook of Electronic and Photonic Materials. Springer.

[3] Adachi S. (1992). Physical Properties of III-V Semiconductor Compounds. Wiley-Interscience publication, Wiley.

[4] Vegard L. (1921). Die konstitution der mischkristalle und die raumfllung der atome. *Zeitschrift fr Physik A Hadrons and Nuclei*. **5 1**, 17-26.

[5] Pauling L. (1932). The nature of the chemical bond. IV. The energy of single bonds and the relative electronegativity of atoms. *Journal of the American Chemical Society*. **54 9**, 3570-3582.

[6] Pauling L. (1960). The Nature of the Chemical Bond and the Structure of Molecules and Crystals: An Introduction to Modern Structural Chemistry. George Fisher Baker lectures, Cornell University Press.

[7] Schwingenschlögl U. , Chroneos A., Schuster C., Grimes R. W. (2012). Electronegativity and doping in semiconductors. *Journal of Applied Physics*. **112**, 046101.

[8] Walukiewicz W., Shan W., Yu K., Ager III J., Haller E., Miotkowski I., Seong M., Alawadhi H., Ramdas A. (2000). Interaction of localized electronic states with the conduction band: Band anticrossing in II-VI semiconductor ternaries. *Physical Review Letters*. **85 7**, 1552-1555.

[9] Shan W., Walukiewicz W., Ager III J., Haller E., Geisz J., Friedman D., Olson J., Kurtz S.R. (1999). Band anticrossing in GaInNAs alloys. *Physical Review Letters*. **82 6**, 1221-1224.

[10] Erol A. (2008). Dilute III-V Nitride Semiconductors and Material Systems: Physics and Technology. volume **105**. Springer.

[11] Sólyom J. (2007). Fundamentals of the Physics of Solids: Volume **1**: Structure and Dynamics. Springer-Verlag Berlin Heidelberg.

[12] Basak C., Sengupta A., Kamath H. (2003). Classical molecular dynamics simulation of UO to predict thermophysical properties. *Journal of Alloys and Compounds*. **360 1**, 210-216.

[13] Henini M. (2004). Dilute nitride semiconductors. Access Online via Elsevier.

[14] Wu J. (2002). Band anti-crossing effects in highly mismatched semiconductor alloys. Ph.D. thesis, University of California, Berkeley

[15] Hjalmarson, H. P., Vogl, P., Wolford, D., Dow, J. D. (1980). Theory of substitutional deep traps in covalent semiconductors. *Physical Review Letters*. **44**, 810813.

[16] Wolford, D., Bradley, J., Fry, K., Thompson, J. (1984). Physics of Semiconductors, ed JD Chadi and WA Harrison.

[17] Thomas, D., Hopfield, J., Frosch, C. (1965). Isoelectronic traps due to nitrogen in gallium phosphide. *Physical Review Letters*. **15 22**, 857.

[18] Yu, K., Walukiewicz, W., Wu, J., Shan, W., Beeman, J., Scarpulla, M., Dubon, O., Becla, P. (2003). Diluted II-VI oxide semiconductors with multiple band gaps. *Physical Review Letters*. **91 24**. 246403.

[19] Mattila, T., Zunger, A. (1998). Deep electronic gap levels induced by isovalent P and As impurities in GaN. *Physical Review B*. **58 3**, 1367.

[20] Wu, J., Walukiewicz, W., Yu, K., Denlinger, J., Shan, W., Ager III, J., Kimura, A., Tang, H., Kuech, T. (2004). Valence band hybridization in N-rich $GaN_{1x}As_x$ alloys. *Physical Review B*. **70 11**, 115214115221.

[21] Trumbore, F. A., Gershenzon, M., Thomas, D. G. (1966). Luminescence due to the isoelectronic substitution of bismuth for phosphorus in gallium phosphide. *Applied Physics Letters*. **9 1**, 46.

[22] Alberi, K., Wu, J., Walukiewicz, W., Yu, K., Dubon, O., Watkins, S., Wang, C., Liu, X., Cho, Y. J., Furdyna, J. (2007). Valence-band anticrossing in mismatched III-V semiconductor alloys. *Physical review B*. **75 4**, 045203.

[23] Harris, J. S., Jr. (2002). GaInNAs long-wavelength lasers: progress and challenges. *Semiconductor Science and Technology*. **17**, 880891.

[24] Kaiser, P. (2001). Photonic network trends and impact on optical components. Digest of LEOS Summer Topical Meetings: WDMComponents, Keystone, CO, July 30, pp. 34, private communication.

[25] Weyers, M., Sato, M. Ando, H. (1992). Red shift of photoluminescence and absorption in dilute GaAsN alloy layers. *Japanese Journal of Applied Physics*. **31**, 853.

[26] Kunert B., Volz K., Stolz W. (2007). Dilute nitride Ga(NAsP)/GaP-heterostructures: toward a material development for novel optoelectronic functionality on Si-substrate. *Physica Status Solidi B*. **244** 2730-2739.

[27] Bugajski M., Kontkiewicz A. M., Mariette H. (1983). Energy bands of ternary alloy semiconductors: coherent-potential-approximation calculations. *Physical Review B.* **28**, 7105.

[28] Wolford D. J., Streetman B. G., Hsu W. Y., Dow J. D., Nelson R. J., Holonyak Jr N. (1976). Evidence for Radiative Recombination in $GaAs_{1-x}P_x$:N ($0.28 \leq x \leq 0.45$) Involving an Isolated Nitrogen Impurity State Associated with the Γ 1 Minimum. *Physical Review Letters.* **36**, 1400.

[29] Logan R. A., White H. G., Wiegmann W. (1968).Efficient Green Electroluminescence in Nitrogen-Doped GaP p-n Junctions. *Applied Physics Letters.* **13**, 139.

[30] Thomas D. G., Hopfield J. J. (1966). Isoelectronic Traps Due to Nitrogen in Gallium Phosphide. *Physical Review.* **150**, 680.

[31] Groves W. O., Herzog A. H., Crawford M. G. (1971). The Effect of Nitrogen Doping on $GaAs_{1x}P_x$ Electroluminescent Diodes. *Applied Physics Letters.* **19**, 184.

[32] Holonyak Jr N., Scifres D. R., Burnham R. D., Crawford M. G., Groves W. O., Herzog A. H. (1971). Stimulated Emission Involving the Nitrogen Isoelectronic Trap in $GaAs_{1x}P_x$. *Applied Physics Letters.* **19**, 254.

[33] Wolford D. J., Streetman B. G., Nelson R. J., Holonyak Jr N. (1976). Stimulated emission on N x ("Aline") recombination transitions in nitrogenimplanted $GaAs_{1x}P_x$ (x$\approx$0.37). *Applied Physics Letters.* **28**, 711.

[34] Leheny R. F., Shah J. (1975). Optical pumping in nitrogen-doped GaP. *Physical Review B.* 12, 3268.

[35] Wolford D. J., Bradley J. A., Fry K., Thompson J., 1984. in Proc. of the 17th International Conference on the Physics of Semiconductor, Springer, New York.

[36] Kondow M., Uomi K., Hosomi K., Mozume T. (1994). Gas-Source Molecular Beam Epitaxy of GaN_xAs_{1-x} Using a N Radical as the N Source. *Japanese Journal of Applied Physics*, *33*, L1056.

[37] Klar P. J., Grüning H., Heimbrodt W., Koch J., Höhnsdorf F., Stolz W., Vicente P. M. A., Camassel J. (2000). From N isoelectronic impurities to N-induced bands in the GaN_xAs_{1-x} alloy. *Applied Physics Letters.* **76**, 3439.

[38] Sturge M. D. (1962). Optical Absorption of Gallium Arsenide between 0.6 and 2.75 eV. *Physical Review.* **127**, 768.

[39] Lorenz M. R., Pettit G.D., Taylor R.C. (1968). Band Gap of Gallium Phosphide from 0 to 900K and Light Emission from Diodes at High Temperatures. *Physical Review.* **171**, 876.

[40] Kondow M., Uomi K., Niwa A., Watahiki S., Yazawa Y. (1996). GaInNAs: A Novel Material for Long-Wavelength-Range Laser Diodes with Excellent High-Temperature Performance. *Japanese Journal of Applied Physics.* **35**, 1273.

[41] Sato S., Satoh S. (1998). Metalorganic chemical vapor deposition of GaInNAs lattice matched to GaAs for long-wavelength laser diodes. *Journal of Crystal Growth*. **192**, 381.

[42] Lindsay A., OReilly E. P. (1999). Theory of enhanced bandgap non-parabolicity in GaN_xAs_{1-x} and related alloys. *Solid State Communications*. **112**, 443.

[43] Skierbiszewski C., Pfeffer P., Lusakowski J. (2005). Effective g factor in the diluted nitrides $Ga_{1-y}In_yN_xAs_{1-x}$. *Physical Review B*. **71**, 205203.

[44] Lindsay A., OReilly E. P. (2004). A tight-binding-based analysis of the band anti-crossing model in GaN_xAs_{1-x}. *Physica E*. **21**, 901.

[45] Masia F., Pettinari G., Polimeni A., Felici M., Miriametro A., Capizzi M., Lindsay A., Healy S. B., OReilly E. P., Cristofoli A., Bais G., Piccin M., Rubini S., Martelli F., Franciosi A., Klar P. J., Volz K., Stolz W. (2006). Interaction between conduction band edge and nitrogen states probed by carrier effective-mass measurements in $GaAs_{1-x}N_x$. *Physical Review B*. **73**, 073201.

[46] Baillargeon J. N., Cheng K. Y., Hofler G. E., Pearah P. J., Hsieh K. C. (1992). Luminescence quenching and the formation of the $GaP_{1-x}N_x$ alloy in GaP with increasing nitrogen content. *Applied Physics Letters*, **60**, 2540.

[47] Miyoshi S., Yaguchi H., Onabe K., Ito R., Shiraki Y. (1993). Metalorganic vapor phase epitaxy of $GaP_{1-x}N_x$ alloys on GaP. *Applied Physics Letters*. **63**, 3506.

[48] Xin H. P., Welty R. J., Tu C. W. (2000). $GaN_{0.011}P_{0.989}$ red light-emitting diodes directly grown on GaP substrates. *Applied Physics Letters*, **77**, 1946.

[49] Sato T., Imai M. (2002). Effects of nitrogen on GaAsP light-emitting diodes. *Journal of Applied Physics*. **91**, 6266.

[50] Güngerich M., Klar P. J., Heimbrodt W., Weiser G., Geisz J. F., Harris C., Lindsay A., OReilly E. P. (2006). Experimental and theoretical investigation of the conduction band edge of GaN_xP_{1-x}. *Physical Review B*. **74**, 241202(R).

[51] Broesler, R. J., Jr. (2010). Characterization of Novel Semiconductor Alloys for Band Gap Engineering. Ph.D. thesis, University of California, Berkeley.

[52] Yuen, H. B. (2006). Growth and characterization of dilute nitride antimonides for long-wavelength optoelectronics. Ph.D. thesis, Stanford University.

[53] Buyanova I. A., Izadifard M., Kasic A., Arwin H., Chen W. M., Xin H. P., Hong Y. G., Tu C. W. (2004). Analysis of band anticrossing in GaN_xP_{1-x} alloys. *Physical Review B*. **70**, 085209.

[54] Xin H. P., Tu C. W., Zhang Y., Mascarenhas A. (2000). Effects of nitrogen on the band structure of GaN_xP_{1-x} alloys. *Applied Physics Letters*. **76**, 1267.

[55] Leibiger G., Gottschalch V., Schubert M., Benndorf G., Schwabe R. (2002). Evolution of the optical properties of III-V nitride alloys: Direct band-to-band transitions in GaN_yP_{1-y} ($0<y<0.029$). *Physical Review B.* **65**, 245207.

[56] Shan W., Walukiewicz W., Yu K. M., Wu J., Ager III J. W., Haller E. E., Xin H. P., Tu C. W. (2000). Nature of the fundamental band gap in GaN_xP_{1-x} alloys. *Applied Physics Letters.* **76**, 3251.

[57] Verlet, L. (1968). Computer Experiments on Classical Fluids. II. Equilibrium Correlation Functions. *Physical Review.* **165**, 201214.

[58] Berendsen, H. J., Postma, J. P. M., van Gunsteren, W. F., DiNola, A., Haak, J. (1984). Molecular dynamics with coupling to an external bath. *The Journal of Chemical Physics.* **81**, 3684.

[59] Andersen, H. C. (1980). Molecular dynamics simulations at constant pressure and/or temperature. *The Journal of Chemical Physics.* **72**, 2384.

[60] Jin, X., Fuchib S., Takeda Y. (2013). Effect of compressive strain relaxation on surface morphology in GaAsP growth on GaP substrate. *Journal of Crystal Growth.* **370**, 204-207.

[61] Abramkin D. S., Putyato M. A., Budennyy S. A., Gutakovskii A. K., Semyagin B. R., Preobrazhenskii V. V., Kolomys O. F., Strelchuk V. V., Shamirzaev T. S. (2012). Atomic structure and energy spectrum of Ga(As,P)/GaP heterostructures. *Journal of Applied Physics.* **112**, 083713.

[62] Wetzel C., Meyer B. K., Omling P. (1993). Electron effective mass in direct-band-gap $GaAs_{1-x}P_x$ alloys. *Physical Review B.* **47**, 15588.

[63] Kunert B., Volz K., Koch J., Stolz W. (2006). Direct-band-gap Ga(NAsP)-material system pseudomorphically grown on GaP substrate. *Applied Physics Letters.* **88**, 182108.

[64] Ünsal Ö.L., Gönül B., Temiz M. (2014). A theoretical investigation of the band alignment of type-I direct band gap dilute nitride phosphide alloy of $GaN_xAs_yP_{1-x-y}$/GaP quantum wells on GaP substrates. *Chinese Physics B*, **23**, 7.

[65] Perkins J. D., Mascarenhas A., Zhang Y., Geisz J. F., Friedman D. J., Olson J. M., Kurtz S. R. (1999). Nitrogen-Activated Transitions, Level Repulsion, and Band Gap Reduction in $GaAs_{1-x}N_x$ with $x<0.03$. *Physical Review Letters.* **82**, 3312-3315.

[66] Chamings J., Adams A. R., Sweeney S. J., Kunert B., Volz K., Stolz W. (2008). Temperature dependence and physical properties of Ga(NAsP)/GaP semiconductor lasers. *Applied Physics Letters.* **93**, 101108-101111.

[67] Chamings J., Ahmed S., Adams A., Sweeney S. J., Odnoblyudov V. A., Tu C. W., Kunert B., Stolz W. (2009). Band anti-crossing and carrier recombination in dilute nitride phosphide based lasers and light emitting diodes. *Physica Status Solidi B.* **246**, 527-531.

[68] Vurgaftman I., Meyer J. R. (2003). Band parameters for nitrogen-containing semiconductors . *Journal of Applied Physics*. **94**, 3675-3696.

[69] Adachi S. (1993). Properties of Aluminium Gallium Arsenide, INSPEC. pp.82.

[70] Christensen N. E., Gorczyca I. (1994). Optical and structural properties of III-V nitrides under pressure. *Physical Review B*. **50**, 4397.

[71] Madelung O.,Von Der Osten W., Rössler U. (1986). Intrinsic Properties of Group IV Elements and III-V, II-VI and I-VII Compounds, Springer Science and Business Media. pp.73.

[72] Wu J., Shan W., Walukiewicz W., Yu K. M., Ager III J. W., Haller E. E., Xin H. P., Tu C. W. (2001). Effect of band anti-crossing on the optical transitions in $GaAs_{1-x}N_x$/GaAs multiple quantum wells. *Physical Review B*. **64**, 085320.

[73] Zhang Y., Mascarenhas A., Xin H. P., Tu C. W. (2000). Formation of an impurity band and its quantum confinement in heavily doped GaAs:N. *Physical Review B*. **61**, 7479.

[74] Skierbiszewski C., Perlin P., Wisniewski P., Knap W., Suski T. ,Walukiewicz W., Shan W., Yu K. M., Ager J. W., Haller E. E., Geisz J. F., Olson J. M. (2000). Large, nitrogen-induced increase of the electron effective mass in $In_yGa_{1-y}N_xAs_{1-x}$, *Applied Physics Letters*. **76**, 2409.

[75] Hai P. N., Chen W. M., Buyanova I. A., Xin H. P., Tu C. W. (2000). Direct determination of electron effective mass in GaNAs/GaAs quantum wells. *Applied Physics Letters*. **77**, 1843.

[76] Skierbiszewski C. , Perlin P., Wisniewski P., Suski T., Geisz J. F., Hingerl K., Jantsch W., Mars D. E., Walukiewicz W. (2001). Band structure and optical properties of $In_yGa_{1-y}As_{1-x}N_x$ alloys. *Physical Review B*. **65**, 035207.

[77] van de Walle C. G. (1989). Band lineups and deformation potentials in the model-solid theory. *Physical Review B*. **39**, 1871.

[78] Singh J. (2003). Electronic and Optoelectronic Properties of Semiconductor Structures, Cambridge University Press, New York.

[79] Matthews, J. W. and Blakeslee, A. E. (1974). Defects in epitaxial multilayers: I. Misfit dislocations. J. Cryst. Growth 27, 118.

[80] Vurgaftman, I., Meyer, J. R., Ram-Mohan L. R. (2001). Band parameters for III-V compound semiconductors and their alloys. *Journal of Applied Physics*. **89**(11), 5815.

[81] Alberi K., Dubon O. D., Walukiewicz W., Yu K. M., Bertulis K., Krotkus A. (2007). Valence band anticrossing in $GaBi_xAs_{1-x}$. *Applied Physics Letters*. vol.**91**, pp. 051909.

[82] Mohmad, A. R. B. (2013). Growth and Characterisation of GaAsBi. Ph.D. thesis, University of Sheffield.

[83] Usman M., Broderick C. A., Lindsay A., OReilly E. P. (2011). Tight-binding analysis of the electronic structure of dilute bismide alloys of GaP and GaAs. *Physical Review B*, vol.**84**, pp. 245202.

[84] O'Reilly E. P., Lindsay A., Tomi S., Kamal-Saadi M. (2002). Tight-binding and kp models for the electronic structure of Ga(In)NAs and related alloys. *Semiconductor Science and Technology*. vol.**17**, pp. 870.

[85] Janotti A., Wei S. H., Zhang S. B. (2002). Theoretical study of the effects of isovalent coalloying of Bi and N in GaAs. *Physical Review B*. **65**, 115203.

[86] Tixier S., Webster S. E., Young E. C., Tiedje T., Francoeur S., Mascarenhas A., Wei P., Schiettekatte F. (2005). Band gaps of the dilute quaternary alloys $GaN_xAs_{1-x-y}Bi_y$ and $Ga_{1-y}In_yN_xAs_{1-x}$. *Applied Physics Letters*. **86**, 112113.

[87] Francoeur S., Seong M. J., Mascarenhas A., Tixier S., Adamcyk M., Tiedje T. (2003). Band gap of $GaAs_{1-x}Bi_x$, $0 < x < 3.6\%$. *Applied Physics Letters*. 82(22), 3874-3876.

[88] Mascarenhas A., Zhang Y., Verley J., Seong M. J. (2001). Overcoming limitations in semiconductor alloy design. *Superlattices and Microstructures*. **29**, 395.

[89] Köksal, K. (2009). Theoretical Investigation of the Effect of Nitrogen on Optical and Electronic Properties of GaInAsN Semiconductors. Ph.D. Thesis, University of Gaziantep.

[90] Adams M. J. (1981). An Introduction to Optical Waveguides , John Wiley & Sons. pp.82-86

[91] Vahala K. J., Zah C. E. (1988). Effect of doping on the optical gain and the spontaneous noise enhancement factor in quantum well amplifiers and lasers studied by simple analytical expressions. *Applied Physics Letters*. **52**, 1945.

[92] Kudrawiec R., Luce A. V., Gladysiewicz M., Ting M., Kuang Y. J., Tu C. W., Dubon O. D., Yu K. M., Walukiewicz W. (2014). Electronic Band Structure of GaNPAs Highly Mismatched Alloys: Suitability for Intermediate-Band Solar Cells. *Physical Review Applied*. **1**, 034007.

[93] Döscher H. (2013). GaP Heteroepitaxy on Si(100). Springer.

[94] Adachi S. (2005). Properties of Group-IV, III-V and II-VI Semiconductors, John Wiley & Sons. p. 154.

[95] Gönül B. (1995). A Theoretical Study of the Threshold Current of Quantum Well Lasers. Ph.D. thesis, University of Surrey.

[96] Gönül B., Oduncuoğlu M., Dindaroğlu S., Yağdıran B. (2003). Influence of doping on gain characteristics of GaInNAs/GaAs quantum well lasers. *Semiconductor Science and Technology*. **18**, 163.

[97] Patane A., Balkan N. (2012). Semiconductor Research: Experimental Techniques, Springer Science & Business Media. pp. 187188.

LIST OF PUBLICATIONS

[1] Çapak M., Cançelik Y., Ünsal Ö.L., Atay Ş., Gönül B. (2011). An extended scenario for the Schrodinger equation. *Journal of Mathematical Physics*. **52**, 102102.

[2] Gönül B., Ünsal Ö.L., Gönül B. (2013). An exactly solvable algebraic model for single quantum well treatments. *Applied Mathematics*. **4**, 7-13.

[3] Ünsal Ö.L., Gönül B., Temiz M. (2014). A theoretical investigation of the band alignment of type-I direct band gap dilute nitride phosphide alloy of $GaN_xAs_yP_{1-x-y}$/GaP quantum wells on GaP substrates. *Chinese Physics B*, **23**, 7.

[4] Ünsal Ö.L., Gönül B. (2016). Revealing the effects of nitrogen on threshold current density in $GaN_xAs_{1-x-y}P_y$/GaP/$Al_zGa_{1-z}P$ type I QW laser structures by hydrostatic pressure. *Physica E*. **80**, 176-184.